Advancements to Magnetic Resonance Flow Imaging in the Brain

by

Sudarshan Ragunathan

A Dissertation Presented in Partial Fulfillment
of the Requirements for the Degree
Doctor of Philosophy

Approved July 2017 by the
Graduate Supervisory Committee:

James Pipe, Co-Chair
David Frakes, Co-Chair
Vikram Kodibagkar
Rosalind Sadleir
Houchun Hu

ARIZONA STATE UNIVERSITY

August 2017

ABSTRACT

Magnetic resonance flow imaging techniques provide quantitative and qualitative information that can be attributed to flow related clinical pathologies. Clinical use of MR flow quantification requires fast acquisition and reconstruction schemes, and minimization of post processing errors. The purpose of this work is to provide improvements to the post processing of volumetric phase contrast MRI (PCMRI) data, identify a source of flow bias for cine PCMRI that has not been previously reported in the literature, and investigate a dynamic approach to image bulk cerebrospinal fluid (CSF) drainage in ventricular shunts. The proposed improvements are implemented as three research projects.

In the first project, the improvements to post processing are made by proposing a new approach to estimating noise statistics for a single spiral acquisition, and using the estimated noise statistics to generate a mask distinguishing flow regions from background noise and static tissue in an image volume. The mask is applied towards reducing the computation time of phase unwrapping. The proposed noise estimation is shown to have comparable noise statistics as that of a vendor specific noise dynamic scan, with the added advantage of reduced scan time. The sparse flow region subset of the image volume is shown to speed up phase unwrapping for multidirectional velocity encoded 3D PCMRI scans. The second research project explores the extent of bias in cine PCMRI based flow estimates is investigated for CSF flow in the cerebral aqueduct. The dependance of the bias on spatial and temporal velocity gradient components is described. A critical velocity threshold is presented to prospectively determine the extent of bias as a function of scan acquisition parameters. Phase contrast MR imaging is not sensitive to measure bulk CSF drainage. A dynamic approach using a CSF label is investigated in the third project to detect bulk flow in a ventricular shunt. The proposed approach uses a preparatory pulse to label

CSF signal and a variable delay between the preparatory pulse and data acquisition enables tracking of the CSF bulk flow.

To Srirekha Gopalan,

Kamala Paati, Paachaa Thatha, Mohana Paati, Cheenu Thatha and,

The Beracah Gang

ACKNOWLEDGMENTS

I would like to take this opportunity to thank Dr. James Pipe for his invaluable guidance and mentorship over the course of my doctoral research. I would like to thank the members of my graduate committee, Dr. David Frakes, Dr. Vikram Kodibagkar, Dr. Rosalind Sadleir and Dr. Houchun Hu for their input and feedback at key stages of my research progress. I am thankful to all my colleagues at the Barrow Neurological Institute for the impromptu discussions and for assistance in the data acquisition process of my thesis. Most importantly, without the support of my family, my parents Geeta Ragunathan and N P Ragunathan, my brother Sharan, and my wife Srirekha in particular, I would not be successful in completing the requirements of this program. I would also like to acknowledge that this work was funded in part by Philips Healthcare.

TABLE OF CONTENTS

CHAPTER Page

CHAPTER Page

CHAPTER Page

LIST OF TABLES

LIST OF FIGURES

Figure Page

Figure Page

Figure Page

Figure Page

PREFACE

The work presented in Chapter 4 of this dissertation document contains material from a manuscript that has been submitted to an academic journal and is currently under review. This manuscript has the author of this dissertation as the first author. The details of the manuscript title, authors, and the chapter that the material is located in are as follows :

- Ragunathan S and Pipe JG, "RF Saturation Induced Bias in Aqueductal Cerebrospinal Fluid Flow Quantification Obtained using 2D Cine Phase Contrast Magnetic Resonance Imaging", Magnetic Resonance in Medicine, 2017 (Under Review). (Chapter 4).

Chapter 1

INTRODUCTION

Phase contrast magnetic resonance imaging (PCMRI) is a commonly used approach to obtain quantitative flow information of blood or cerebrospinal fluid (CSF) flow in the brain. The diagnostic utility of PCMRI can be affected by slow reconstruction due to computationally complex post-processing methods, inaccuracies in flow quantification introduced by magnitude and phase errors during acquisition, and the inability of PCMRI to detect the slow CSF drainage into the venous system. The goal of this work is to investigate the accuracy of velocity estimates obtained using 2D PCMRI, propose improvements to the post processing of PCMRI data and explore alternatives to the PCMRI technique for applications in CSF flow imaging.

The process of flow quantification involves multiple stages of post processing including background noise suppression, and segmentation of flow regions. The focus of the proposed improvements to PCMRI post-processing, is to develop an intrinsic method of noise estimation for spiral trajectories and use multidirectional velocity encoding [95] to improve noise suppression and identification of flow regions. Accuracy of phase contrast measurements have been shown to be affected by bias in flow estimates due to resolution, partial volume and intra-voxel flow dephasing. However, RF saturation effects on velocity estimates have not been well characterized. These effects are expected to bias velocity estimates obtained from 2D PCMRI. The objective here is to understand the factors influencing the bias. Cerebrospinal fluid flow alterations have been associated with pathological conditions such as normal pressure hydrocephalus (NPH). Currently, PCMRI is the primary imaging technique that provides dynamic CSF flow information. Phase contrast approaches however, have

not been successful in quantifying bulk CSF drainage. A solution is proposed by implementing a dynamic approach using single shot spin echo techniques using RF preparation to label CSF flow.

This work begins with an introduction to MR imaging fundamentals and presents the concepts related to MR flow imaging in Chapter 2. Chapter 3 describes the noise estimation approach for spiral MRI and its application to speed up phase unwrapping. The extent of RF saturation induced bias in quantitative CSF flow estimates in the cerebral aqueduct obtained using cine PCMRI based acquisitions is presented in Chapter 4. Chapter 5 introduces a dynamic labeling approach to detect bulk CSF drainage in the cerebral aqueduct and in a ventricular shunt. Chapter 6 summarizes the improvements proposed to flow imaging techniques and Chapter 7 outlines opportunities for future work on these projects.

Chapter 2

FUNDAMENTALS OF MAGNETIC RESONANCE IMAGING

Magnetic resonance imaging (MRI) is a medical imaging modality that utilizes the principles of nuclear magnetic resonance (NMR) and electromagnetic induction to generate a spatial and temporal map of an anatomical region of interest. The history of development in MRI can be summarized through some of the pivotal breakthroughs in the field. Some of the earliest work in studying magnetic properties of atomic nuclei can be credited to Sir Isidor Isaac Rabi in the 1930s [74]. A decade later, Felix Bloch and Edward Mills Purcell demonstrated the concept of NMR in condensed matter [3, 73]. One of the most important contributions to the field of NMR/MRI was the discovery of the spin echo by Erwin Hahn in the 1950s [30]. High resolution NMR spectroscopy was developed by Richard R Ernst in the 1960s [20]. Sir Peter Mansfield and Paul Lauterbur were the first to introduce spatial localization to produce the first MR images [43, 50].

This chapter explains the fundamental concepts related to MRI and introduces quantitative flow imaging in the brain. Section 2.1 provides a brief overview of MR physics. Section 2.2 presents the commonly used pulse sequences to image fluid flow in the human body. The quantitative aspects of flow imaging will be explained in detail in Section 2.3. For further reading on topics related to MRI concepts and to understand the quantitative aspects of MRI, [9, 29, 45] are recommended references.

2.1 From individual spins to an image

The fundamental concept of generating an MR image is best explained using three conditions : (i) The structure being imaged has a measurable magnetic moment from

its protons (this work is focused towards ^{1}H MR imaging), (ii) Using the principles of on-resonant excitation, the magnetization vector can be perturbed in a controlled fashion by an RF waveform, and (iii) The rotating magnetization vector induces a measurable signal in a receive coil. Each of the three stages will be described in the following subsections.

2.1.1 The measurable magnetization of an object

Every nucleus can be described by a unique set of quantum numbers. The quantum characteristic relevant to MRI is the spin quantum number, denoted by I. The spin quantum number takes a discrete set of values that are either integer (0, $\pm$1, $\pm$2, ...) or half-integer ($\pm$1/2, $\pm$3/2, $\pm$5/2, ...). ^{1}H spins have $I = 1/2$, and such a system is called spin-1/2 system. The microscopic magnetic moment ($\vec{\mu}$) can be obtained from the spin quantum number as,

$$\vec{\mu} = \frac{\gamma h}{2\pi}\sqrt{I(I+1)}, \tag{2.1}$$

where γ is the gyromagnetic ratio and is equal to 42.577 MHz/T for ^{1}H, and h is the Planck's constant (6.6 x 10^{-34} J/s). The magnetic moment vector can have ($2I$+1) possible orientations. For ^{1}H spins, this value is 2. Essentially, when ^{1}H spins are placed in a static magnetic field ($\mathbf{B}_0$), the spins either align with the magnetic field or against it. These spins will experience a torque which is equal to the rate of change of angular momentum, and causes the spins to precess about the axis of $\mathbf{B}_0$ (the $\mathbf{B}_z$ component). The precession frequency of the spins is called the Larmor frequency, and is given by $\omega_0 = \gamma\mathbf{B}_0$.

The collective behavior of a spin system is the relevant property that will henceforth be of interest, and can be described by the macroscopic magnetization vector

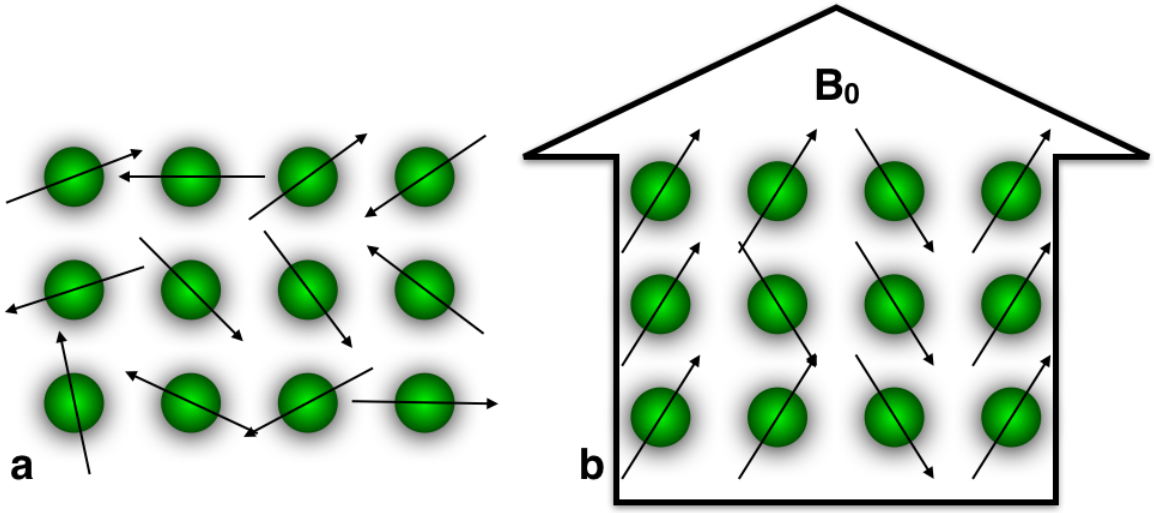

Figure 2.1: Polarization of protons in the presence of a static magnetic field.

$(\vec{M})$ such that

$$\vec{M} = \sum_{n=1}^{N} \vec{\mu_n} \tag{2.2}$$

where N is the total number of spins in the object being imaged.

When the object is placed in the static field $\mathbf{B}_0$, $\vec{M}$ now precesses about $\mathbf{B}_z$ at frequency equal to ω_0 given by

$$\omega_0 = \gamma B_0. \tag{2.3}$$

In the presence of $\mathbf{B}_0$ (Fig. 2.1), each magnetic moment orientation experiences a different energy interaction with the static magnetic field. For the specific case of ^{1}H spins, the two energy states are described as

$$E_\uparrow = -\frac{1}{2}\gamma\hbar B_0 \tag{2.4}$$

and

$$E_\downarrow = \frac{1}{2}\gamma\hbar B_0. \tag{2.5}$$

The spin population difference is provided by the difference in the two energy states. The net magnetization is then obtained by substituting the difference in Eq. 2.2.

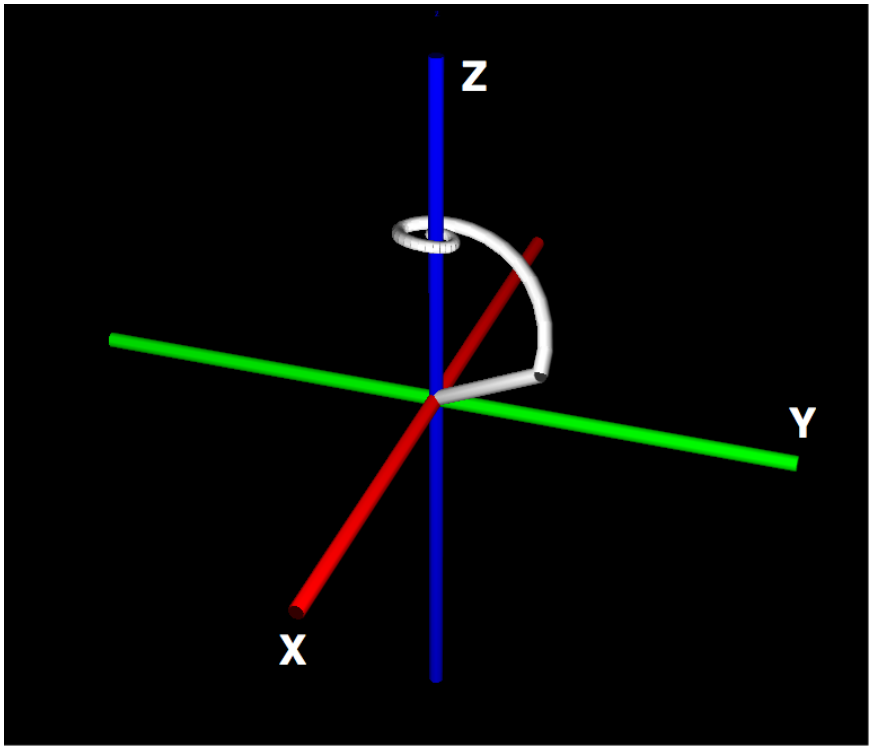

Figure 2.2: Simulation of the excitation of a spin isochromat on to the transverse plane using a RF pulse.

2.1.2 RF Excitation

When an object is placed in a static magnetic field (B_0), the ^{1}H spins precess about B_0 with frequency ω_0. This state shall be referred to as the initial state, when discussing the MR experiment and image generation. The magnetization $\mathbf{M}$ at any given time be described by it's two orthogonal components, the longitudinal ($\mathbf{M}_z$) and the transverse ($\mathbf{M}_\perp$) components. At the initial state, $\mathbf{M}_\perp = 0$.

It is important to mention here that the transverse component of the precessing magnetization is the source of measurable MR signal. Signal measurement is possible due to Faraday's principle of induction, where a rotating magnetic field will induce current in a coil. The process of 'tipping' the magnetization to the transverse plane

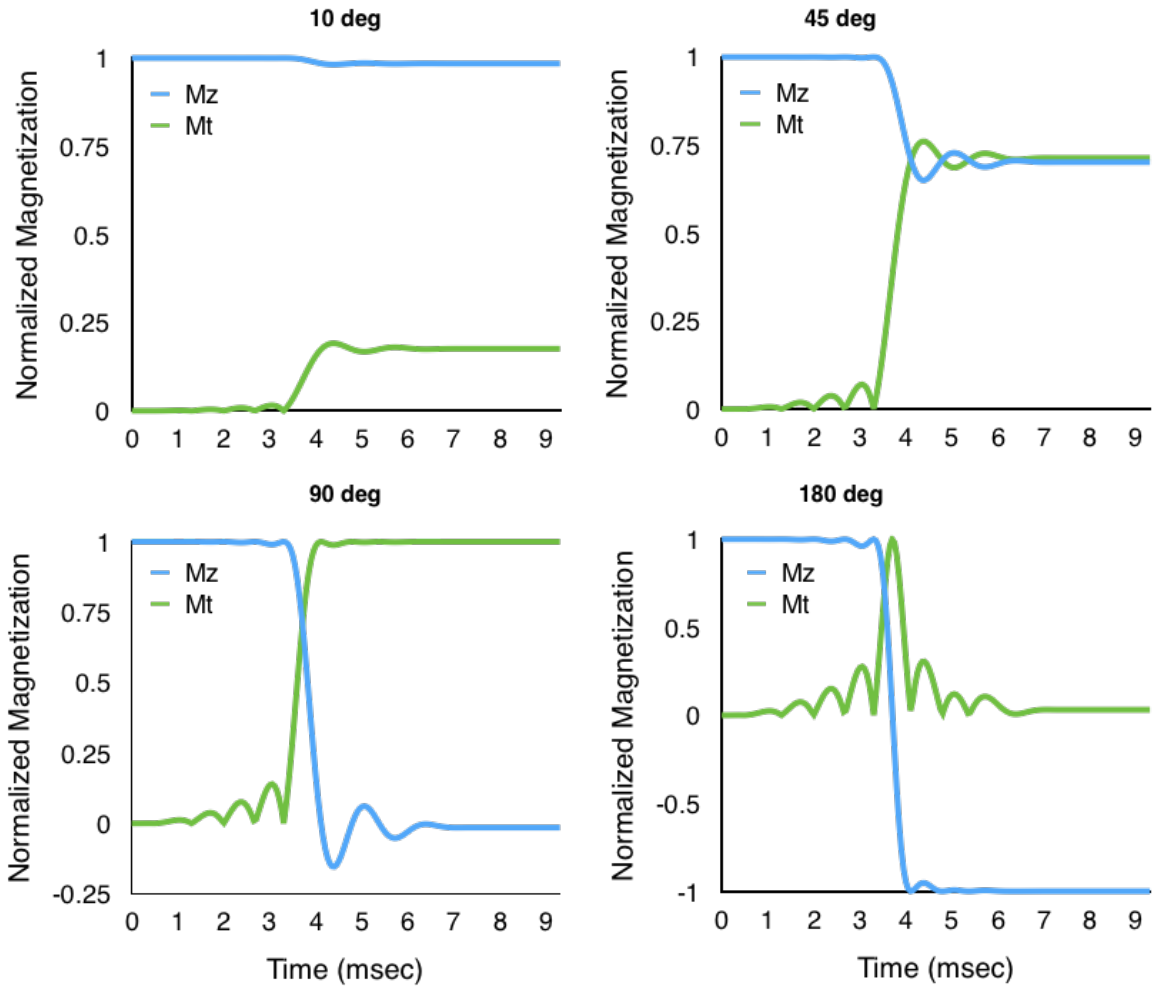

Figure 2.3: The evolution of transverse (Mt) and longitudinal (Mz) magnetization as a function of time as a result of RF excitation using four different flip angles.

is achieved by applying an oscillating magnetic field ($\mathbf{B}_1$) with the same frequency as ω_0. Due to the phenomenon of resonance, $\mathbf{M}$ interacts with the $\mathbf{B}_1$ field while continuing to precess around $\mathbf{B}_0$ as shown in Fig. 2.2. This interaction results in the tipping of $\mathbf{M}$ on to the transverse plane. Once in the transverse plane, the spins continue to precess about $\mathbf{B}_0$ and as a result of principle of induction, a measurable signal is detected in a RF receive coil. This process is also called RF excitation. The simulation of RF excitation of a single spin isochromat is depicted in Fig. 2.2.

The amount of transverse magnetization measured from RF excitation differs for varying degrees of tipping of the magnetization vector away from the longitudinal axis. The angle of excitation, also known as the flip angle (θ), is defined as the angle made by $\mathbf{M}$ on application of the RF excitation pulse and is given by

$$\theta(t) = \gamma \int_{\tau=0}^{t} B_1(\tau) d\tau. \tag{2.6}$$

Figure 2.3 shows the time evolution of longitudinal and transverse magnetization as a result of RF excitation for some commonly used flip angles. Small values of flip angles such as 10^o is sufficient to produce an appreciable transverse magnetization without a substantial loos in longitudinal magnetization. This is useful in fast scanning applications that employ gradient echo based sequences. Alternatively, a flip angle of 90^o tips all of the magnetization on to the transverse plane. This is useful in spin echo based imaging and in applications that incorporate RF pulses for magnetization preparation such as in fat saturation, or T2 preparation for example. A 180^o flip angle is typically used in inversion recovery sequences where contrast generation is based on nulling the signal from a particular tissue or fluid.

2.1.3 Relaxation phenomenon and contrast generation

The RF excitation phenomenon causes the bulk magnetization to reach a higher energy state. The magnetization remains in this higher energy state for the duration of the RF excitation pulse. Once the RF pulse is not applied, the magnetization starts to go back to the lower energy or initial state. The process is called relaxation and has two components, namely: transverse relaxation characterized by the exponential time constant T_2, and longitudinal relaxation characterized by the exponential time constant T_1. Both T_1 and T_2 relaxations occur simultaneously, and their durations vary depending on the object, or tissue sample being imaged.

Longitudinal relaxation is the process by which the bulk magnetization **M** returns to it's initial value parallel to the static magnetic field. This process is also called the spin-lattice relaxation. When **M** returns to it's original state, the energy of the system decreases. This release of energy occurs into the surrounding structure (lattice). The relaxation process takes different times for different ^{1}H spin environments, and is characterized by the time constant T_1. T_1 is defined as the time taken for the z-component of **M** to reach 63% of its maximum value. The process can be described as

$$M_z(t) = M_z(0)(1 - e^{-\frac{t}{T_1}}). \tag{2.7}$$

Transverse relaxation is the process by which the $\mathbf{M}_\perp$ component of the bulk magnetization decays in the transverse plane. This process is also called spin-spin relaxation. In addition to the spin-lattice interactions, the proximity of spins gives rise to variations in the magnetic field experienced by the interacting nuclei changing its precession frequency by a small amount, briefly. This causes the exponential decay of the magnetization in the transverse plane over time and is characterized by the time constant T_2. T_2 is defined as the time taken for the transverse magnetization to decay to 37% of its initial value. The mathematical expression for T_2 relaxation is given by

$$M_\perp(t) = M_\perp(0)e^{-\frac{t}{T_2}}. \tag{2.8}$$

Both T_1 and T_2 relaxation are based on the intrinsic properties of the object or tissue being imaged. The transverse relaxation process can be further accelerated due to the influence of external factors such as variations in the static magnetic field due to improper shimming, susceptibility variations due to the presence of metallic objects or implants in close proximity to the imaging object. This contributing factor

to transverse relaxation is represented as $T_2^{'}$. The accelerated relaxation is given as

$$\frac{1}{T_2^*} = \frac{1}{T_2} + \frac{1}{T_2^{'}} \tag{2.9}$$

The T_2^* effects from the phase incoherence of the transverse magnetization can be compensated by using refocussing RF pulses in spin echo based pulse sequences, a topic that is discussed in detail in section 2.2.2.

There are two frames of reference, the laboratory frame and the rotating frame of reference generally used to describe MRI phenomenon. The laboratory frame of reference is fixed with respect to the scanner orientation. The bore of an MRI system lies along the $Z^{'}$ axis, while the $X^{'}$ and $Y^{'}$ axes are defined using the right handed Cartesian coordinate system. The rotating frame of reference is obtained by rotating the $X^{'}Y^{'}$ plane of the laboratory frame around the $Z^{'}$ axes at an angular frequency equal to ω_0. Nomenclature distinction between the two frames is achieved by labeling the axes of the rotating frame as X, Y and Z with their corresponding unit vectors denoted by $\hat{x}$, $\hat{y}$ and $\hat{z}$. Therefore, a spin isochromat precessing at ω_0 in the laboratory frame will appear to be stationary in the rotating frame of reference.

It is important to note that both the relaxation phenomena occur concurrently and last for different durations. The transverse relaxation typically is much faster than the longitudinal relaxation. The Bloch equations describe the time dependent evolution of magnetization incorporating the effects of longitudinal and transverse relaxation. The magnetization ($\vec{M}$) at any given instant t in the rotating frame of reference is given as

$$\frac{d\vec{M}}{dt} = \gamma\vec{M} \times \vec{B} - \frac{M_x\hat{x} - M_y\hat{y}}{T_2} - \frac{(M_0 - M_z)\hat{z}}{T_1}. \tag{2.10}$$

The first term on the right hand side of 2.10 describes spin precession, the second term describes the T_2 relaxation process while the last term describes T_1 relaxation.

2.1.4 Spatial Localization

The previous section described the basic experiment to detect an MR signal. The signal detected is essentially the sum of contributions from all the spins in the system, which must be spatially resolved in order to generate images. This spatial localization is performed using magnetic field gradients. Gradients in MRI refer to the deliberate spatial variations of the magnetic field B_0 produced by specialized hardware comprising of gradient coils, and its driving sources. Magnetic field gradients along the three orthogonal axes of the Cartesian coordinate system are generated using three separate gradient coils. There are three types of gradients that are used for localization namely : frequency encoding, phase encoding, and slice selective gradients. These are not the only gradients used, but in some way represent the minimum requirements for a conventional imaging experiment. Other gradients can be termed functional, or application specific such as flow encoding gradients, diffusion gradients, spoilers, etc. Flow encoding gradients will be further explained in detail later in this chapter, as they are important for flow quantification.

Frequency encoding gradients assign unique precession frequencies to each spin isochromat at a distinct spatial location in the direction of the gradient application during signal measurement. The frequency encoding gradient can be applied in any direction. The frequency encoding gradient waveform in Fourier encoded pulse sequences typically consists of a prephaser gradient lobe that is opposite in polarity to the readout gradient lobe. Data acquisition is performed at the onset of the readout gradient lobe. This arrangement is used in the generation of an echo. Assuming that the frequency encoding gradient G_x is applied along some direction X (with no loss in generalization), the spatial encoding of unique precession frequencies is demonstrated

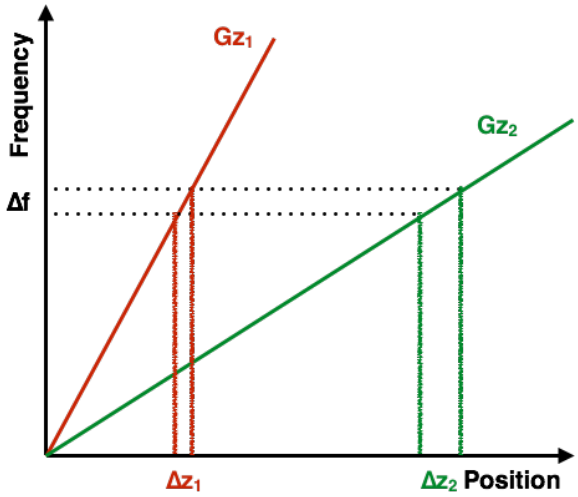

Figure 2.4: Larmor frequency versus position along the slice selection gradient direction. The bandwidth of the RF pulse and the gradient strength determine the thickness of the slice.

using Eq. 2.11.

$$\omega^{'}(x,t) = \gamma(B_0 + G_x(t)x) \tag{2.11}$$

Phase encoding is used to create a linear spatially varying phase of the transverse magnetization. It is implemented by applying a constant gradient lobe prior to application of the frequency encoding gradient. The area under the phase encoding gradient lobe changes for every TR to acquire multiple lines in K-space (explained in section 2.1.5). This is a typical implementation for data acquired on a Cartesian grid. If the frequency encoding gradient is applied along X, then the phase encoding gradient G_y is typically applied along Y for single slice acquisitions. In the case of volumetric acquisitions, phase encoding gradients are applied in both Y and Z directions (assuming frequency encoding occurs along X). The combination of frequency and phase encoding constitutes spatial localization in MR.

Slice selection is performed by applying a constant gradient concurrently with a spatially selective RF pulse (excitation, refocusing, inversion, spatial preparation).

The amplitude of the gradient lobe applied and the bandwidth of the RF pulse determine the slice thickness, as shown in Fig. 2.4. The gradient Gz_1 is stronger than Gz_2, and hence for the same RF bandwidth, Gz_1 results in a thinner slice than when Gz_2 is applied. Slice selection gradient application results in phase dispersion across the slice. Therefore, a slice rephasing gradient is applied which is opposite in polarity to the slice selection gradient to compensate for the phase dispersion. The slice thickness can be obtained as

$$\Delta z = \frac{2\pi \Delta f}{\gamma G_z}. \tag{2.12}$$

2.1.5 K-Space

K-space is essentially an multidimensional array representation of the object being imaged in the Fourier domain of the object. In essence, K-space represents the spatial frequencies of the imaged object. In MRI experiments, the MR signal is measured in K-space and then Fourier transformed to obtain a map of the signal object in image space. K-space is mathematically defined as

$$\vec{k}(t) = \frac{\gamma}{2\pi} \int_0^t \vec{G}(\tau) d\tau \tag{2.13}$$

where $\vec{G}(\tau)$ is the applied imaging gradient. Therefore, K-space traversal is governed by the application of frequency, phase and slice encoding gradients. While the position in K-space at any given time is governed by the area under the gradient lobe, the gradient amplitude determines the speed of K-space traversal. Figure 2.5 shows the effect of K-space coverage on the image. Most of the contrast information is contained at the center of K-space, while the high spatial frequencies contain information about the edges or sharp transitions in the image. If the resolution of the image is denoted by res and the field of view by FOV, the extent of K-space is equal to $1/res$, and the distance between successive K-space samples is equal to $1/FOV$. Improper

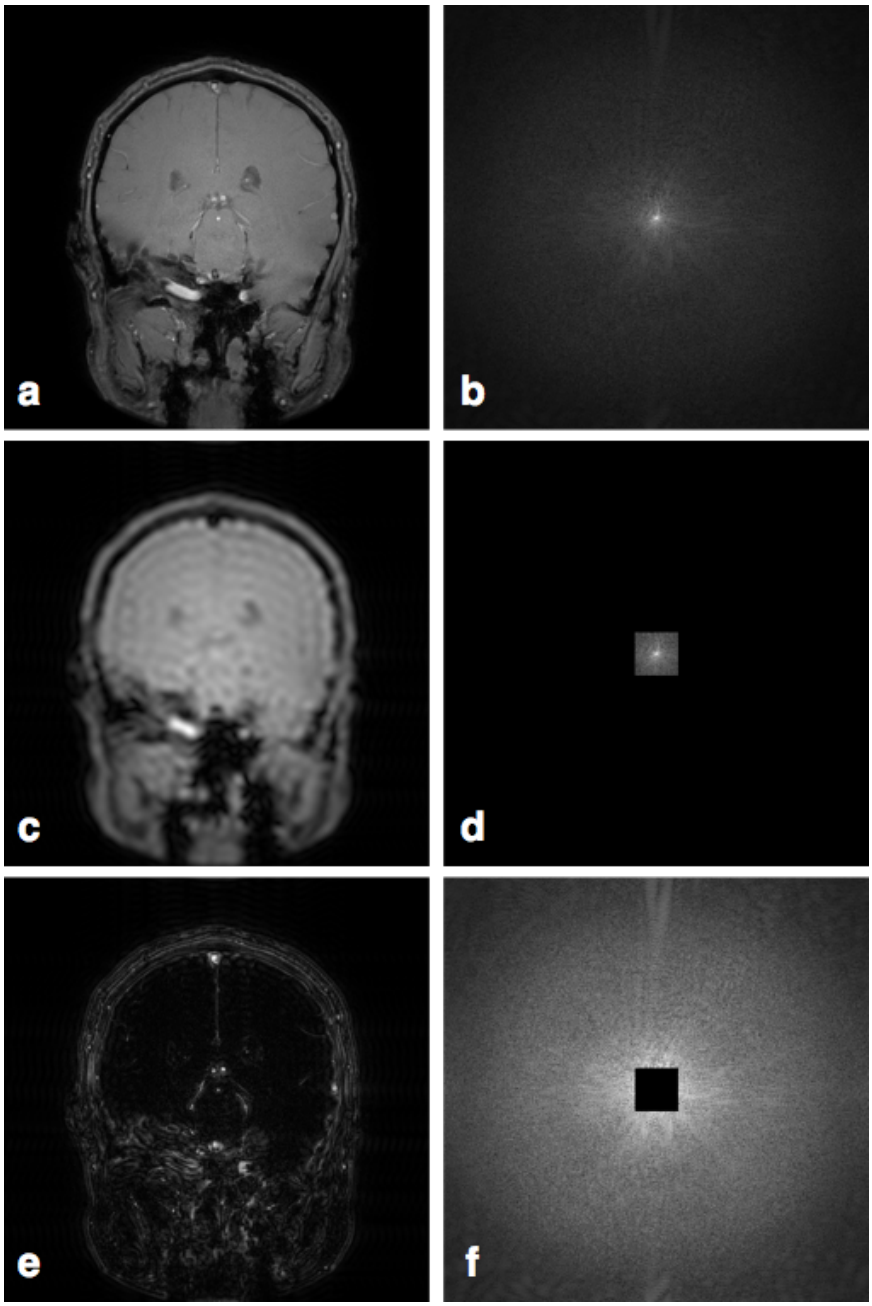

Figure 2.5: (a), (c) and (e) show images generated when K-space is sampled fully, regions around center of K-space are sampled, and when everything but the center is sampled respectively. (b), (d) and (f) show the corresponding K-space data.

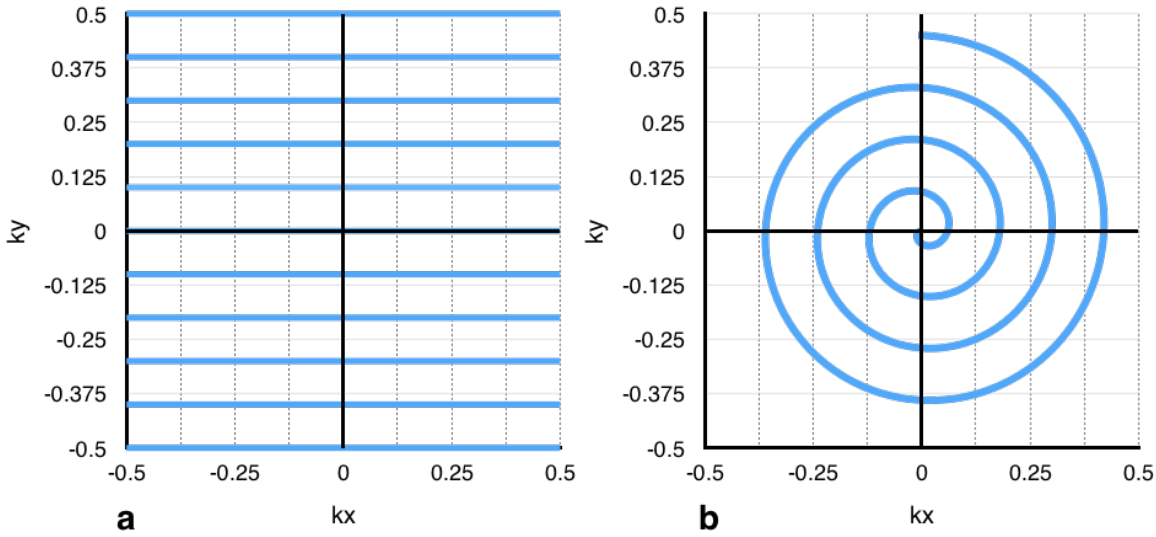

Figure 2.6: (a) Cartesian sampled K-space. Each blue line indicates a K-space line that is acquired in a single TR. (b) A single spiral interleaf in K-space.

K-space sampling can lead to the presence of artifacts in the image. If the extent of sampled K-space is not large enough, ringing can be observed in regions with sharp transitions in the image. The image overall also appears blurred when compared to a higher resolution image. Decreasing the K-space sampling density could result in aliasing artifact in the image.

The path mapped out by K-space as a result of the imaging gradients is called the K-space trajectory. This trajectory is governed by the amplitude and temporal profile of the imaging gradients applied in the pulse sequence. K-space trajectories can be two or three dimensional. The most commonly used K-space trajectory is rectilinear K-space sampling also known as the Cartesian trajectory. Chapter 5 of this work uses a Cartesian trajectory in acquiring K-space. In a typical Cartesian trajectory based pulse sequence, K-space is filled at the rate of one line per TR. Each line is associated with a unique value of the phase encoding gradient. This makes Cartesian based MR imaging very slow. The reconstruction of data acquired

using Cartesian trajectories is as straightforward as applying the Fourier transform to the K-space data. Non-Cartesian approaches to acquiring K-space have gained popularity in recent times owing to decreased scan time, and in some cases, the incoherent nature of artifacts such as image aliasing. The non-Cartesian trajectory used in Chapters 3 and 4 of this work, is a spiral trajectory. Spiral K-space can be obtained by playing out readout gradients simultaneously along what would have been the frequency and phase encoding directions for a Cartesian MR pulse sequence. Spiral trajectories do not have a phase encoding gradient for each slice. The entire K-space can be obtained in a single TR using a single shot spiral acquisition. Blurring can become an issue with spiral data acquisition and the effect increases as the readout duration increases. When data acquisition is stretched over multiple TRs, the readout gradient duration decreases reducing the effect of blurring, which might still need further correction. Aliasing artifacts for spiral MRI are less coherent than Cartesian MRI. There are some aspects of non-Cartesian data acquisition that have to be taken into consideration. The reconstruction is no longer straightforward. Spiral data acquisition for example, results in non uniform sampling of K-space and the data have to first be mapped on to a cartesian grid and corrected for sampling density variations before being Fourier transformed to obtain the image. Gridding reconstruction can be computationally intensive. Trajectory correction is also an important step in the reconstruction of spiral data. References [60, 68, 70] are suggested for further reading on spiral trajectory design and reconstruction. An example Cartesian and spiral K-space trajectory is shown in Fig. 2.6.

2.2 The basic pulse sequences

A pulse sequence is a timing diagram that describes the sequential and concurrent interaction of RF pulses, gradient waveforms and data acquisition. Any form of MR

experiment will have its unique pulse sequence, that contains information on the trajectory used for data acquisition or the contrast being generated. There are two basic pulse sequences (gradient and spin echoes) that are explained as part of this section. These sequences can then be used as building blocks to build more complex sequences that are application specific such as flow, perfusion, diffusion, elastography, cardiac function, tagging, etc. Since this work is focussed towards flow, a typical angiographic pulse sequence is described in section 2.3.1 as part of velocity encoding strategies.

2.2.1 Gradient Echo Imaging

Gradient echoes are formed by employing imaging gradients to achieve phase coherence of the various spin isochromats tipped on to the transverse plane by the RF excitation pulse. This is achieved by using gradients to dephase and rephase the spin isochromats in the transverse plane without the incorporation of RF pulses for this purpose. These sequences are also commonly known as Gradient Recalled Echoes (GRE) or Field Echoes (FE). An example GRE pulse sequence for a single TR is shown in Fig. 2.7.

Gradient echo based sequences are popular for fast imaging applications. This is because a refocusing pulse is not required to generate echoes, and the use of low flip angle RF excitation pulses. The use of low flip angles implies that a only a small fraction (1-cos θ) of M_z is lost every TR, while maintaining an appreciable amount of measured signal (sin θ). As a result, less T_1 recovery is needed. This reduces the TR when compared to spin echo based sequences (discussed in section 2.2.2), and therefore the scan time. Reduced scan time is not the only reason for the wide applicability of GRE sequences. Application specific contrast generation is another reason for the use of GRE sequences. Hyperintense blood signal and T1 reduction

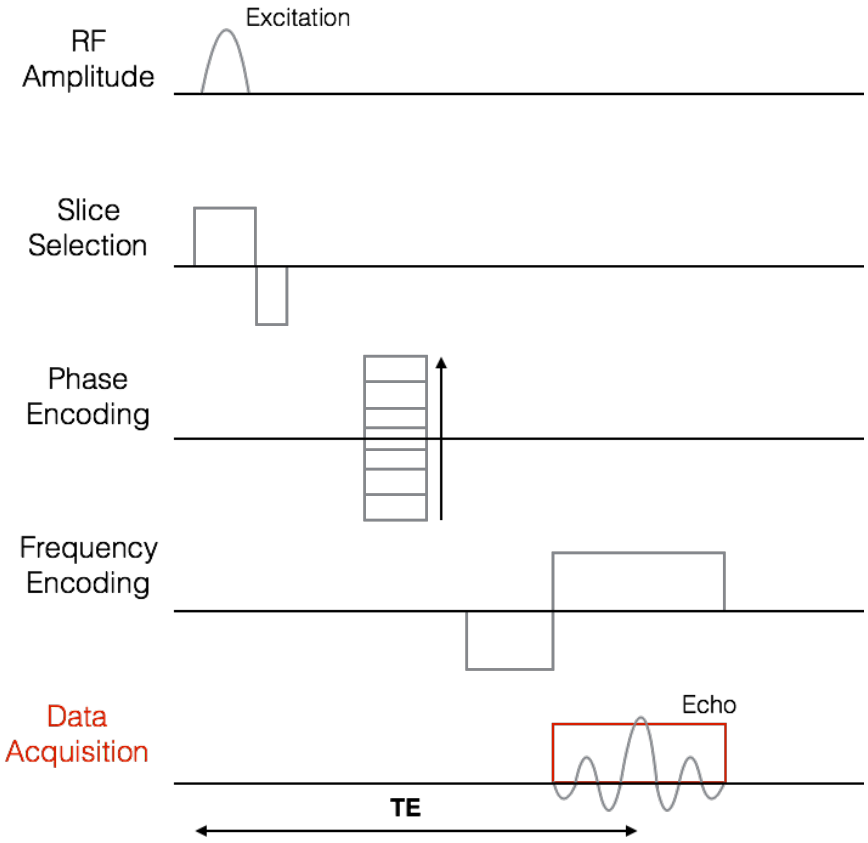

Figure 2.7: A single TR in a gradient echo pulse sequence.

using contrast agents have resulted in GRE based angiographic sequences being used in clinical environments. Since gradient echo formation does not use a refocusing RF pulse, GRE based approaches are useful in detection of hemorrhage due to the T_2^* weighting. Excessive T_2^* weighting can however result in signal loss and is also one of the disadvantages of using GRE based approaches when imaging near metallic implants. GRE sequences can be further classified as spoiled or steady state free precessing (SSFP) depending on the evolution of the transverse magnetization at the end of a single TR. Since this work uses spoiled GRE sequences for flow imaging, a brief description is provided in the following subsection.

Spoiled gradient echo imaging

Spoiling refers to the attenuation of transverse magnetization prior to the application of a successive RF excitation pulse. Spoiling can be achieved by specifying a TR that is much longer than T_2, but this approach is inefficient due to increased scan times. More commonly used approaches that utilize the speed of GRE based sequences employ either gradient based or RF based spoiling. With the case of perfect spoiling, the transverse magnetization is zero when the RF excitation pulse is applied for any given TR. This RF pulse will only excite the longitudinal magnetization recovered from the previous TR. At some point in this process the recovered longitudinal magnetization between two successive TRs will cease to vary. This phenomenon is called the steady state. Henceforth every RF excitation will tip the same amount of magnetization onto the transverse plane. The steady state signal from an gradient refocused echo (S_{GRE}) is obtained as

$$S_{GRE} = \frac{M_0 \sin\theta(1 - e^{-TR/T_1})}{1 - \cos\theta e^{-TR/T_1}} e^{-TE/T_2^*}. \tag{2.14}$$

Under steady state conditions, the flip angle that maximizes the measured signal is called the Ernst angle and is calculated as

$$\theta_{Ernst} = \arccos(e^{-TR/T_1}). \tag{2.15}$$

2.2.2 Spin Echo Imaging

The spin echo was first discovered by Erwin Hahn in 1950 [30]. RF spin echoes are generated using excitation pulses followed by one or multiple refocusing pulses. Typical values of flip angles used for RF excitation and RF refocusing are 90^o, and 180^o respectively. Spin echo based sequences are commonly used in clinical MRI with applications in head, spine and knee imaging. They are also used in black blood and diffusion weighted imaging applications. An example spin echo pulse sequence is

shown in Fig. 2.8. The signal measured from a spin echo sequence can be calculated using Eq. 2.14 for a flip angle of 90^o. This simplifies to

$$S_{SE} = M_0(1 - e^{-TR/T_1})e^{-TE/T_2}. \tag{2.16}$$

An important advantage of using spin echo based sequences is that they are better at imaging near metallic implants when compared to gradient echo based sequences. This is because spin echoes employ RF refocusing pulses that can rephase the spins that accrue phase over time due to field inhomogeneities. However, spin echoes can still not recover the loss due to spin - spin interactions. Hence spin echo based imaging is sensitive to T_2 weighting of the imaging region of interest. Generating T_2 weighted images requires a sufficiently long TE and TR, which can result in fairly long scan times. Thus, scan acceleration becomes an important factor. Rapid acquisition with refocused echoes (RARE) proposed by Henning et al. is a spin echo accelerates spin echo based acquisition by collecting multiple lines in K-space for the series of RF refocusing pulses following a single RF excitation pulse [31]. The commercial implementation of this sequence across vendors is also commonly known as Fast Spin Echo (FSE) or Turbo Spin Echo (TSE). As each line in K-space is associated with an echo formation, the acquisition of multiple K-space lines results in the formation of an echo train. Single shot sequences acquire all of K-space in the echo train following a single RF excitation pulse. Multi shot sequences acquire all of K-space over 2 or more RF excitation pulses followed by a shorter echo train.

Specific Absorption Rate (SAR) is the total RF energy deposition that occurs in a sample over the time of exposure to RF energy. Since spin echo sequences incorporate the repeated use of RF pulses, the SAR in these sequences can increase beyond safe limits. The energy deposition is proportional to θ^2. As a result, a more practical approach to spin echo implementation involves using flip angles $<180^o$

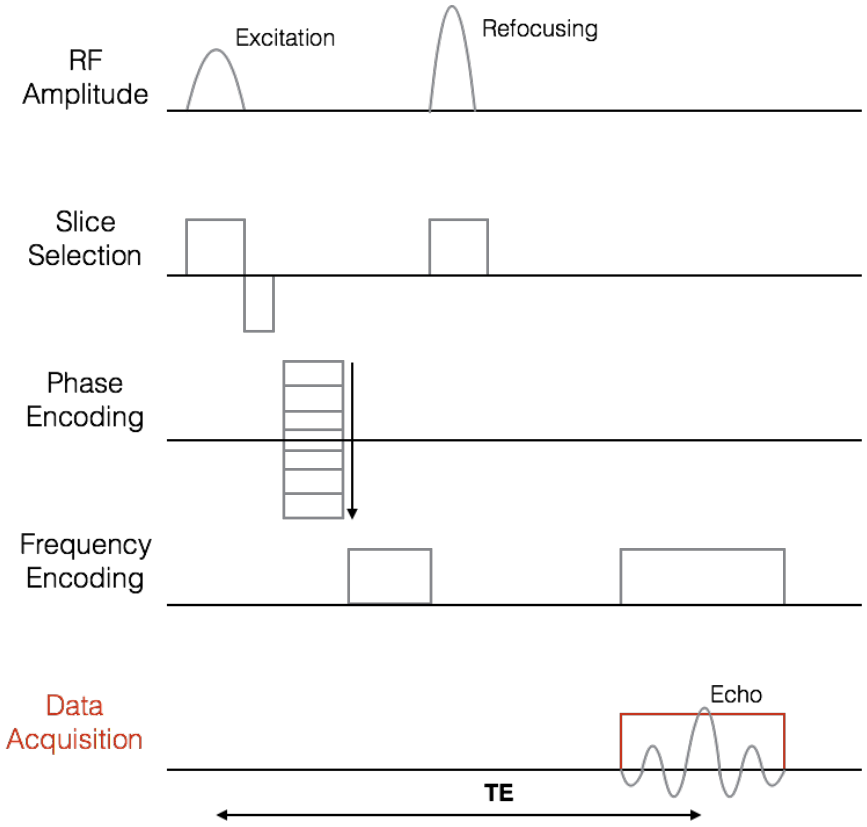

Figure 2.8: A single TR in a spin echo pulse sequence.

for the refocusing pulses. An alternate approach is to use variable flip angle for successive refocusing pulses, but might affect the contrast mechanism desired. Further acceleration in data acquisition can be obtained by combining parallel imaging or partial fourier techniques with a FSE implementation of the sequence. The work described in chapter 5 uses a 2D single shot turbo spin echo sequence with SENSE to dynamically monitor CSF flow in the aqueduct and in a ventricular shunt.

2.3 Concepts related to MR flow imaging

This work focusses on different stages of MR flow imaging, utilizing phase contrast MRI for flow quantification. The subsequent parts of this section will introduce the fundamental concepts required to understand phase contrast MR imaging. The

discussion will begin with the introduction of velocity encoding followed by describing the phase sensitive reconstruction method, and finally discussing the important image processing involved post reconstruction to mitigate artifacts and quantification errors.

2.3.1 Velocity Encoding

Velocity encoding is the process of using gradient waveforms to encode velocity information in the phase of the MR signal. This is achieved with the use of bipolar gradients along the direction requiring velocity encoding. A figurative representation of a bipolar gradient is shown in Fig. 2.9a. The velocity encoding gradients can be applied along one, two, or all three axes to independently encode the three orthogonal components of the velocity vector. The application of a gradient enforces the spin isochromats to accrue phase proportional to the area under the gradient waveform. When a bipolar gradient is applied, the static spins accrue a phase proportional to G_0T_0 for the positive gradient lobe and the same phase in the opposite direction for the duration of the negative gradient lobe. This net phase accrual of static spins is zero. With spins that move with some nonzero velocity, the net phase accumulation is nonzero (as will be shown when discussing first moments). Therefore the velocity is encoded in the phase of the MR signal. A second data acquisition with the same bipolar gradient amplitude and duration but reversed polarity will again result in net zero phase for static spins, while a nonzero phase for spins with nonzero velocities. The phase difference of the two acquisitions provides an estimate of the velocity, and forms the basis of phase contrast MRI (PCMRI). The toggling of bipolar gradient can be independently or simultaneously performed along the three axes depending on the velocity components required. The bipolar gradients are applied after RF excitation and prior to data acquisition. They can also be combined with slice select or phase encoding gradients to minimize TE.

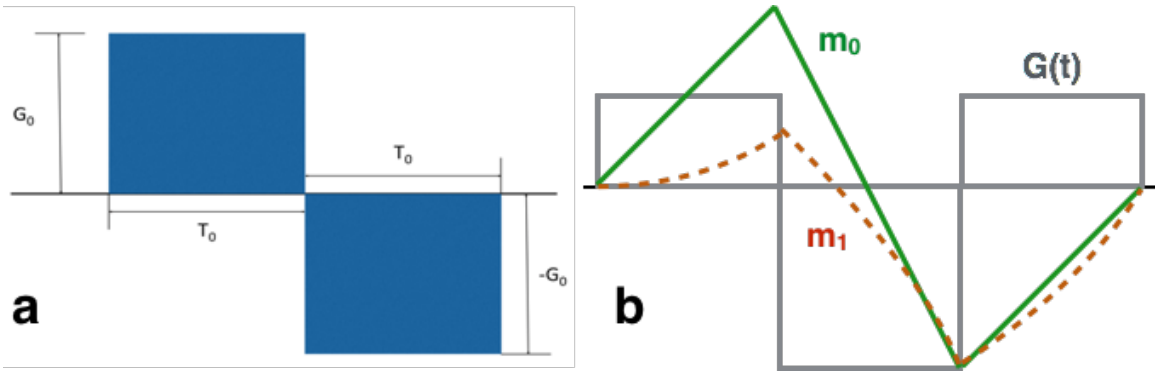

Figure 2.9: (a) A figurative representation of a bipolar gradient with gradient amplitude G_0, and duration $2T_0$. (b) Zero and first order gradient moment evolution with time.

The relationship between phase and velocity can be derived using the gradient moment approach. In the case of macroscopic coherent flow, the position ($x(t)$) of spins at any given time t can be expressed from its Taylor series expansion.

$$x(t) = x_0 + v.t + \frac{at^2}{2} + ..., \tag{2.17}$$

where v is the velocity of the spins and a their acceleration. Typically, only the velocity term is considered from the series, although gradient waveform sensitization to higher order terms can be achieved by extending the concept for the first order term. The phase accrual during the application of bipolar gradient is given as

$$\phi_1 = \gamma \int_0^T G(t)x(t)dt. \tag{2.18}$$

Replacing $x(t)$ from Eq. 2.17,

$$\phi_1 = \gamma \int_0^T G(t)[x_0 + vt]dt \tag{2.19}$$

$$= \gamma[x_0 \int_0^T G(t)dt + v \int_0^T G(t)tdt] \tag{2.20}$$

The first integrand on the right hand side of Eq. 2.20 is the zero order moment (m_0) of the gradient, while the second integrand is the first order moment (m_1). The first

order term is associated with the static spins and the phase accrual over the bipolar gradient duration is zero. Therefore Eq. 2.20 reduces to

$$\phi_1 = \gamma v m_1. \tag{2.21}$$

For the second acquisition the bipolar gradient is toggled to obtained the second phase accrual ϕ_2, which has the same phase magnitude as Eq. 2.21.

$$\phi_2 = -\gamma v m_1 \tag{2.22}$$

The difference in phase provides an estimate of the spin velocity and is given as

$$v = \frac{\Delta\phi}{2\gamma m_1}. \tag{2.23}$$

The evolution of m_0 and m_1 over time due to the application of bipolar gradients is shown in Fig. 2.9b where two bipolar gradients are mirrored and concatenated. As the moment is calculated from the area of the gradient lobe, a time efficient implementation of the gradient can be achieved by doubling the amplitude and halving the duration (while maintaining system limits). When phase coherence is achieved, the value of the gradient moment if zero. This process is called gradient moment nulling, and is used to mitigate phase contributions from the nulled moment during phase difference reconstruction. Figure 2.9 illustrates that implementing a bipolar gradient will null moment contribution from stationary spins, but encode the moment contribution from flowing spins in the phase difference. Extending the bipolar gradient arrangement one more time will result in first order moment nulling. Further extension of the bipolar gradient arrangement will continue to null higher order moments. For practical implementation purposes most sequences employ either zero or first order moment nulling. A basic implementation of a phase contrast MR pulse sequence is represented in Fig. 2.10. Flow compensation is implemented along all three directions. The toggling bipolar velocity encoding gradient is shown in red.

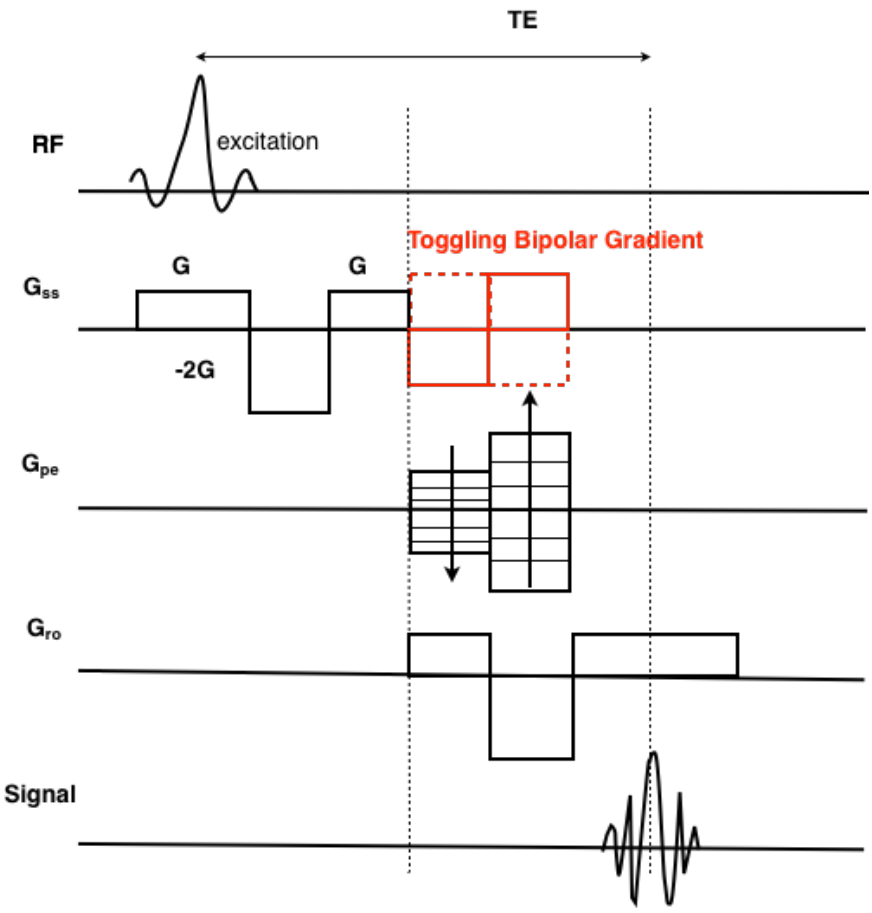

Figure 2.10: Pulse sequence for phase contrast MRI.

2.3.2 Reconstruction and Post-Processing

The reconstruction pipeline to generate velocity maps from the acquired data is shown in Fig. 2.11. Phase difference reconstruction is performed using the four quadrant arctangent denoted by $ATAN2$. For flow encoding along one direction, the phase difference calculated as

$$\Delta\phi = ATAN2\left(\frac{Im(Z_1 Z_2^*)}{Re(Z_1 Z_2^*)}\right), \tag{2.24}$$

where Z_1 and Z_2 are the complex reconstructed images for the two bipolar gradient segments respectively. The $ATAN2$ function extends the dynamic range of the arc tangent operation from $(-\pi/2,\pi/2)$ to $[-\pi,\pi]$. The velocity sensitivity is determined

Figure 2.11: The reconstruction pipeline to generate velocity maps from K-space data obtained using a PCMRI based pulse sequence

by the encoding / aliasing velocity denoted as V_{enc}. When the velocity estimate is equal to V_{enc}, $\Delta\phi = \pi$. For data obtained using a multichannel coil array, Bernstein et al. [8] recommended performing the coil combination prior to performing the phase difference reconstruction. The phase difference maps calculate $\Delta\phi$ for each pixel.

Phase aliasing occurs when the value of $\Delta\phi$ exceeds the dynamic range of the $ATAN2$ operation. The aliasing manifests itself as abrupt transitions in phase and are represented by a value within $[-\pi,\pi]$. Aliasing results in incorrect velocity estimation and has to be corrected for. A simple solution to the problem of aliasing is to specify a sufficiently high enough V_{enc}. Applications that require high velocity to noise ratio use a value of V_{enc} lower than the expected maximum velocity. In these cases, some form of phase unwrapping has to be performed for accurate flow quantification. The phase unwrapping algorithm used in Chapter 3 of this work is described in [95].

Two major sources of phase errors are due to contributions from concomitant field gradients and eddy current based phase offsets. Concomitant fields are nonlinear spatially varying magnetic fields generated as a consequence of Maxwell's equations in the presence of an activated linear gradient. The concomitant magnetic fields result in an additional spatially varying phase $\Delta\phi_c(x, y, z)$ to $\Delta\phi$. The value of $\Delta\phi_c(x, y, z)$ can be exactly calculated and removed from the phase difference maps as demonstrated in [10]. Eddy currents based phase offsets on the other hand cannot be exactly determined and are harder to compensate. These phase errors arise due to rapidly changing gradients during acquisition. Eddy currents can be particularly

troublesome when imaging slow flow regimes such as CSF flow due to the presence of high velocity encoding moments. Limiting the slew rate of the flow encoding gradients will help mitigate these effects but also result in increased TE. A common practice to correct for these errors is to fit the phase of stationary tissue to a second or third order polynomial and subtract the fitted phase from the phase difference maps. More advanced approaches such as the use of magnetic field monitoring to estimate background tissue phase offset have resulted in accurate flow quantification [24].

Velocity estimates ($\hat{v}$) on a voxel by voxel basis are obtained from the phase difference maps as

$$\hat{v} = \frac{\Delta\phi V_{enc}}{\pi}. \tag{2.25}$$

The velocity estimates are obtained concurrently for each velocity encoding direction with the root mean squared of the three velocity components providing the magnitude of the velocity vector. The flow rate is estimated as the sum of the product of the velocity estimate per voxel and the area of the voxel, over the entire flow region of interest. Specific flow quantitative metrics are further explained in Chapter 4.

Chapter 3

USING NOISE STATISTICS FOR FASTER PHASE UNWRAPPING OF 3D PCMRI DATA

Phase contrast magnetic resonance imaging (PCMRI) is a technique that encodes velocity information of the imaging region of interest in the phase of the image. This approach has been widely used to obtain quantitative flow information in vivo for cardiovascular, neuro, and peripheral MR imaging applications. Developments in PCMRI can be traced back to the 1980s with the use of magnetic field gradients sensitive to flow and its effects on MR imaging[5, 53]. The linear relationship between velocity and MR signal phase was introduced by Bryant et al[15]. Phase contrast angiography was applied as a noninvasive quantitative flow imaging technique in cardiovascular applications using 2D acquisitions synchronized to the cardiac cycle[55, 58, 67], and with volumetric acquisitions[19] using efficient velocity encoding strategies[66]. The primary concern with respect to PCMRI data acquisitions was long scan times. With the advent of spatial and temporal image acceleration techniques such as SENSE, GRAPPA and k-t methods [26, 37, 71], scan times for PCMRI have been significantly reduce with the ability to obtain high resolution velocity maps and study of dynamic flow quantitation [11, 51, 80]. Recently quantitative PCMRI has been used successfully in research studies involving clinical outcomes [17, 23, 42, 52, 61–63].

Extraction of quantitative information from PCMRI data involves multiple stages of post-reconstruction processing. The reconstructed phase difference maps are corrected for background phase offsets due to concomitant field and eddy currents [10, 17, 32, 79, 86]. This is followed by phase unwrapping [44, 85], after which, the vessels of interest are manually segmented and quantitative information is computed

from the segmented region of interest. Visualization of PCMRI based velocity maps can be affected due to the presence of background phase noise. Thresholding using magnitude image information is a common method applied to suppress background noise for improved flow region visualization [8, 86]. Zwart and Pipe proposed a multidirectional velocity encoding method which used multiple flow encoding directions and a single low V_{enc} to improve the velocity to noise ratio (VNR) [95]. The shared information between the different non-orthogonal flow encoding directions was used to correct for velocity aliasing. These multiple flow encoding directions can also be used to distinguish background noise from stationary tissue and flow regions using a statistical approach. An important step during the post processing of phase difference reconstruction involves phase unwrapping to correct for velocity aliasing. For typical 3D volumetric data acquisitions, the unwrapping algorithms can become computationally intensive. A flow mask that identifies all the flow regions in an imaging volume could potentially reduce the computation time of phase unwrapping.

This work develops a new approach to estimate noise statistics for spiral MRI and apply the estimated noise in identifying flow regions within a image volume obtained using multidirectional velocity encoded PCMRI. The work masks the background noise and static tissue voxels in the imaging volume, and performs phase unwrapping only on the sparse flow segmented regions. This process is expected to reduce the execution time of the phase unwrapping algorithm by approximately $30\% - 40\%$, as the flow regions are estimated to comprise of $2\% - 3\%$ of the imaging volume. The work is presented as three stages of development. The first stage (Section 3.1) presents a novel approach for noise estimation in spiral MRI. The second stage (Section 3.2) discusses the development of a tri-level mask using the noise statistics from stage one, that is shown to identify and separate background noise, static tissue, and flow regions in an imaging volume. The final stage of development (Section 3.3) involves

a demonstration of phase unwrapping speedup by performing the algorithm on only the flow segmented regions in the volume.

3.1 Noise estimation in spiral MRI

Signal to noise ratio (SNR) is an important quantitative measure of MR image quality. It is therefore desirable to be able to quantify noise in MR images as accurately as possible. Although noise estimation is a problem of notable importance, and the focus of extensive research, there does not exist a gold standard method to estimate noise statistics. A list of some of the existing approaches towards noise estimation is presented, following which the proposed method is briefly outlined.

Extensive research has been conducted detailing the statistical properties of noise present in an MR image [27, 48, 54]. Establishment of the noise distribution in MR images led to the development of statistical models to estimate noise such as using the distribution of local moments [1], or the use of mean absolute deviation estimators in the wavelet domain as described in [65]. The statistical models however exhibit signal dependency, which may decrease the efficiency of the estimator. Another method developed to estimate noise was based on the selection of an appropriate background region of interest (ROI). The work done by Constantinides, et. al [18], explored estimating noise variance from background ROI by obtaining measurements from coil arrays. A major limitation of estimation methods in the image domain is that it can be difficult to select a region of interest with no signal. Noise estimation based on a histogram of the image was also proposed in [34]. However, methods that use the mode of the background data to estimate noise variance, as is the case with the histogram of the image, depend on the assumption that every MR image has sufficient background data required for this method.

The outlined methods attempt to estimate MR noise properties in the image domain, and can be categorized with other post processing techniques that add to the overall implementation time. The objective of this work is to eliminate any signal dependencies during the noise estimation process, and to make the implementation an integral part of the reconstruction process. In this regard, a new method is proposed that utilizes the oversampling of data at low spatial K-space frequencies to eliminate the signal in K-space, generating pure noise in K-space. The method was implemented for single coil data acquired using spiral K-space trajectories.

Data acquired along a spiral K-space trajectory are oversampled at lower spatial frequencies and critically sampled at higher spatial frequencies. The oversampling of spiral trajectories at low spatial frequencies presents the possibility of reconstructing unaliased low-resolution images using only a fraction of the acquired samples. Specifically, the region of K-space oversampled by a factor of 2 or more can be used to reconstruct 2 unaliased images. One can then effectively remove the redundant signal content from these two datasets by appropriate subtraction. The noise content in the two datasets, being independent, adds in the difference image. This difference image contains only noise and can be used to estimate the noise in acquired dataset.

The proposed method was used to generate noise by reconstructing K-space data points in non-Cartesian trajectories oversampled by a factor of 2 or more. The subsection on noise image generation provides a detailed description of the modifications to the gridding process to eliminate the signal in K-space. The variance estimates of the noise generated using the proposed method are derived in the subsection on noise image analysis. This is followed by a brief description of the data acquisition parameters used.

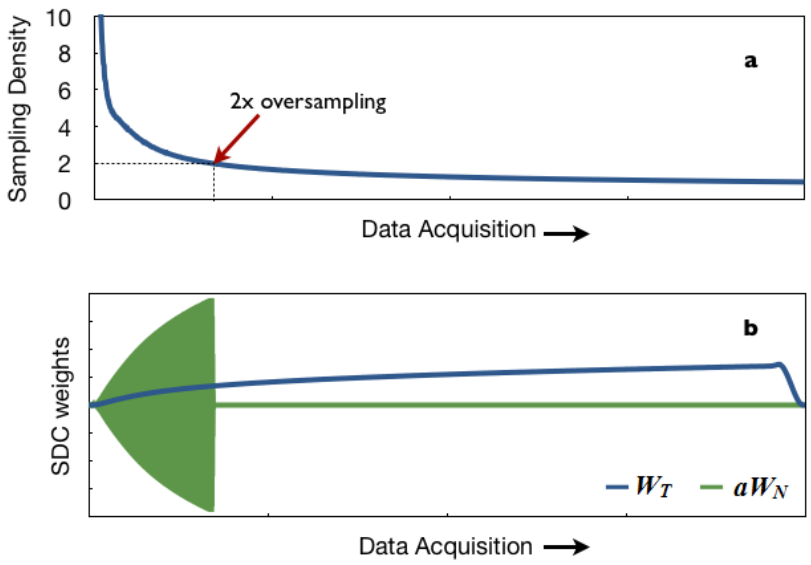

Figure 3.1: (a) During spiral reconstruction, the K-space region oversampled by a factor of 2 or more is used to modify the corresponding SDC weights (b) SDC weights (W_T) used in spiral reconstruction compared with the modified and scaled SDC weights (αW_N)

3.1.1 Noise Image Generation

Data were collected using a stack of spiral trajectory (T points per interleaf) with sampling density along each interleaf as illustrated in Fig. 3.1(a). The corresponding sampling density compensation (SDC) weights [60], are denoted by W_T. The arrow in Fig. 3.1(a) denotes the point prior to which K-space is obtained with an oversampling factor of 2 or more (N data points). A second set of weights W_N, were generated from W_T as follows. For the first N points along each interleaf, the weights with odd indices were scaled by -1. The remaining SDC weights for W_N after these N points were set to zero. Gridding reconstruction was performed twice, once using W_T, and once using W_N as the SDC weights. All other steps in the reconstruction process

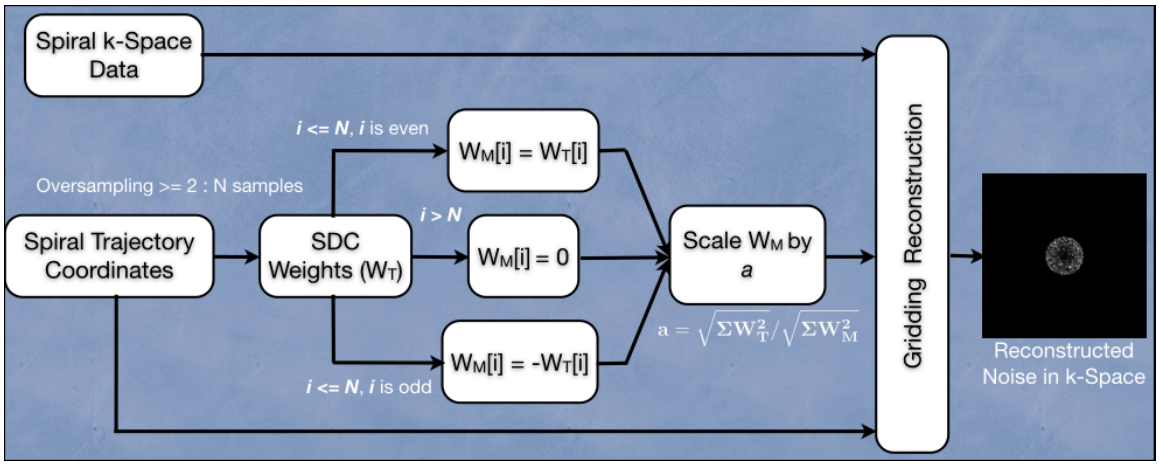

Figure 3.2: Flowchart of the noise variance estimation algorithm for spiral MRI : Generating the low resolution noise image during spiral reconstruction in GPI

were identical in both cases. The Fourier transform of the data weighted by W_N and then gridded resulted in a noise image.

The noise generated from N data points was scaled when compared to the noise in the fully sampled data. The scaling factor (α) is quantified as shown in the next subsection. With an appropriate value of α applied to the noise standard deviation obtained using the proposed method (σ_N), an estimate of the noise standard deviation in the fully sampled data (σ_T) was obtained. The gridding reconstruction, Fourier transform and variance calculations were performed offline using the Graphical Programming Interface (GPI) [59] software platform. The proposed approach to generate noise data in K-space is shown in Fig. 3.2.

3.1.2 Noise Image Analysis

The standard deviation of noise in the image domain is related to the standard deviation of noise in K-space according to:

$$\sigma_{image} = C\sigma_{kspace}\sqrt{\Sigma W^2}, \tag{3.1}$$

where, σ_{image} and σ_{kspace} are the standard deviations in image and K-space respectively, W denotes the sampling density compensation weights, and C is a scaling constant. As mentioned in the previous subsection, the proposed method makes use of the first N samples. The noise standard deviations of the images using W_T and W_N were obtained from Eq. 3.1 as

$$\sigma_T = C\sigma_{kspace}\sqrt{\Sigma W_T^2}, \tag{3.2}$$

$$\sigma_N = C\sigma_{kspace}\sqrt{\Sigma W_N^2}, \tag{3.3}$$

Dividing Eq. 3.2 by Eq. 3.3 gives

$$\sigma_T = \alpha\sigma_N, \tag{3.4}$$

where

$$\alpha = \sqrt{\frac{\Sigma W_T^2}{\Sigma W_N^2}}. \tag{3.5}$$

The value of σ_N was estimated from the noise image, then scaled by α to obtain an estimate of σ_T. This scaling factor α was in practice applied to the wieghts; thus images were created using W_T and αW_N, as illustrated in Fig. 3.1(b). Equation 3.4 therefore represents the noise standard deviation estimate in a spiral acquisition, in terms of the noise standard deviation of the reconstructed $2x$ oversampled region in K-space and scaled appropriately.

3.1.3 Data Acquisition

Phantom data were obtained on a Philips 3T Ingenia scanner using a 2D spiral gradient echo scan with the following acquisition parameters - FOV/Res: 240 mm/0.8 mm; 48 spiral interleaves; τ: 9.612 ms; $T = 2226$ samples; $N = 132$ samples. Thirty repetitions of the phantom scan were performed to obtain noise statistics.

Seven volunteer datasets were obtained on the 3T Ingenia scanner using a stack of spiral gradient echo scan with the following acquisition parameters - FOV/Res: 220 mm/1.0 mm; 48 spiral interleaves; τ: 6.162 ms; $T = 1802$ samples; $N = 398$ samples. A noise reference scan was obtained from the scanner using the same protocol, but with the RF excitation turned off.

A standard Philips noise dynamic scan was performed for both phantom and volunteer experiments and used as the ground truth to evaluate the accuracy of the noise statistics obtained using the proposed method. Noise variance estimates were calculated in GPI separately for the real and imaginary channels of the reconstructed complex noise images for the proposed method and the reference noise dynamic. Real and imaginary channel histograms were generated for the complex noise images obtained using the proposed approach. A T-test was performed to determine if there was a significant difference in the noise standard deviation estimates obtained using the proposed approach when compared to the ground truth.

3.1.4 Results and Discussion

The output of the gridding algorithm produced a single coil complex noise image. Figure 3.3 shows the reconstructed images. The first column shows the phantom image and the volunteer brain image, while the second column shows the noise image obtained using the proposed method. The volunteer/phantom images and their corresponding noise images were obtained were obtained using a single GPI network. The values of the standard deviation of the complex noise obtained by the proposed method was compared with that of a noise reference scan obtained using the same scan parameters. The comparison is summarized in Table 3.1 by separating the complex noise into the real and imaginary channel. A histogram of the real and imaginary

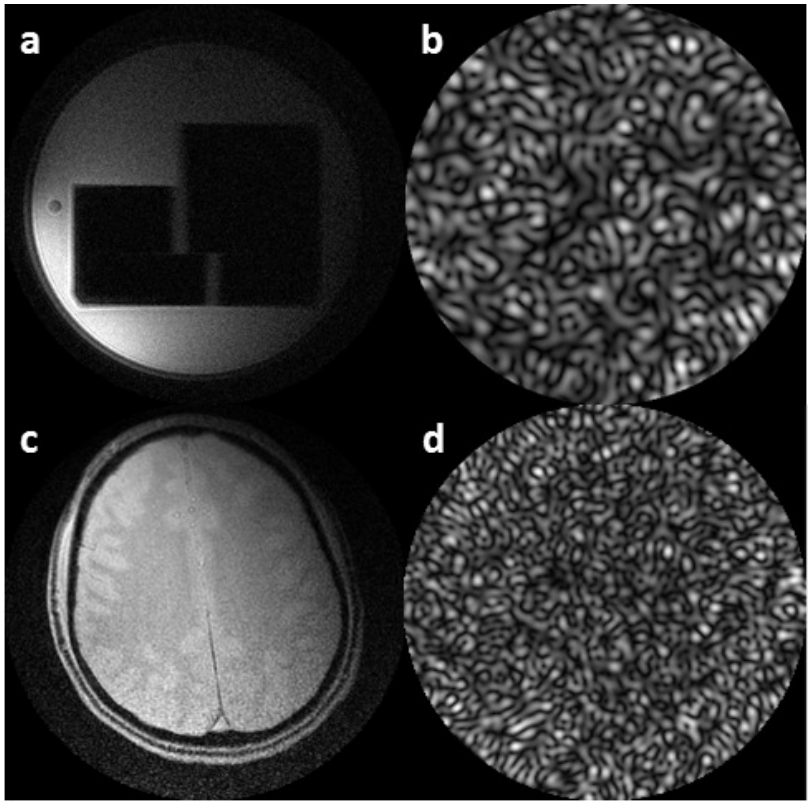

Figure 3.3: 2D phantom and volunteer images acquired using spiral trajectories (a, c), and their respective reconstructed noise images (b, d) obtained using the proposed method.

Table 3.1: Noise Standard Deviation Estimates (σ_T)

	Phantom (mean $\pm$ σ)		Volunteer (mean $\pm$ σ)	
	RF off	Proposed Method	RF off	Proposed Method
Real Channel	60.26 $\pm$ 0.60	61.2407 $\pm$ 0.08	81.28 $\pm$ 0.40	81.04 $\pm$ 0.08
Imaginary Channel	60.23 $\pm$ 0.67	60.9678 $\pm$ 0.08	81.29 $\pm$ 0.37	81.50 $\pm$ 0.08

channels of the reconstructed noise image was obtained as shown in Fig. 3.4 to provide a visual representation of the noise distribution.

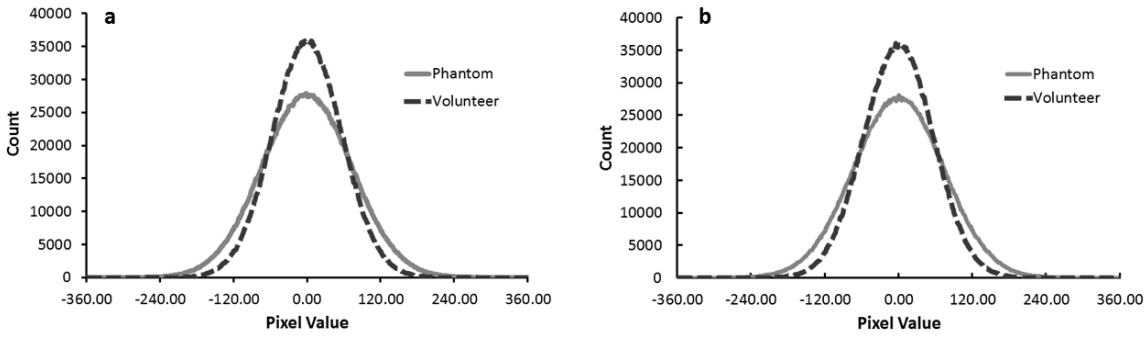

Figure 3.4: Histogram of the reconstructed noise image from phantom and volunteer data depicting the noise distribution in the real channel (a) and the imaginary channel (b).

Table 3.1 shows that the standard deviation estimates of the noise obtained using the proposed method are comparable to those obtained using a noise reference scan. However, it is important to note that the noise generated using the proposed method is not the same noise as is present in the acquired data. Since the $2x$ oversampling region in K-space corresponds to low spatial frequencies, the high spatial frequency content is masked resulting in a reconstructed noise image that has a lower resolution than the image reconstructed from the original dataset using all K-space data. This effect is also illustrated in Fig. 3.3(b) and in Fig. 3.3(d), where the noise images were reconstructed using different values of N. Quantitatively, the effect is compensated by introducing a scaling factor as shown in Eq. 3.4, to obtain an accurate quantitative estimate of the noise standard deviation. The histograms of complex noise generated using the proposed approach were indicative that there was no substantial deviation from zero mean of the real and imaginary noise channels of phantom and volunteer data. Hypothesis testing comparing the noise standard deviations of the proposed approach and the ground truth revealed that there was no significant difference between the statistics obtained from the two methods.

The noise estimation method proposed in this work was evaluated for 2D spirals and stack of spiral trajectories. In theory, this method would be applicable to any trajectory that has oversampling in the readout direction. Although the readout direction for Cartesian trajectories may be oversampled, nonlinear filtering or post processing techniques could affect the accuracy of the proposed method, since the underlying assumption is that the reconstruction is a linear process preserving the complex Gaussian nature of noise. Currently this approach has been evaluated for single coil reconstruction. The proposed method would not work for a sum of squares coil combination as this process is nonlinear. This method should work for a linear combination of data weighted by coil sensitivities, provided the off diagonal elements have low amplitudes when compared to the main diagonal components.

3.1.5 Summary

A new method was proposed to estimate the noise standard deviation for spiral imaging. The method incorporated the oversampling of data at low spatial frequencies, to eliminate the signal content during the reconstruction process. The appropriate scaling factors were incorporated while generating the SDC weights and hence avoided unnecessary post processing of the reconstructed noise image. An added advantage of the integrated implementation is the ability to reconstruct the original data and the noise image concurrently for SNR applications. The proposed method does not require multiple acquisitions, or dependency on a background region of interest.

3.2 Flow region identification for multidirectional velocity encoded PCMRI

Phase contrast magnetic resonance imaging (PCMRI) has been repeatedly shown to be the method of choice for in vivo fluid flow quantification. PCMRI uses motion sensitizing gradients to encode velocity information. Phase difference reconstruction

involves the subtraction of the phase images obtained using acquisitions for each flow encoding gradient, and the flow compensated acquisition. Velocity estimates are obtained from the phase difference images as shown in Eq. 3.6.

$$\tilde{v} = \frac{\Delta\phi}{V_{enc}}. \tag{3.6}$$

Extraction of quantitative information from PCMRI data involves multiple stages of post-reconstruction processing. The phase difference reconstruction is performed using a 4 quadrant arctangent operation commonly denoted by the function $ATAN2$. This function is defined only in the interval $[-\pi/2, \pi/2]$. Flow quantification accuracy is primarily affected due to phase errors. Eddy currents introduce nonzero background phase variations in static tissues. These errors can be compensated for by estimating a polynomial fit to the background phase. Phase errors can also arise due to contributions from concomitant field gradients, which can be estimated analytically and corrected. Incorrect velocity estimates can also be obtained as a result of phase aliasing. This occurs when the V_{enc} specified is not higher than the maximum velocity in the image volume. To obtain an accurate estimate of the velocity, the phase difference images have to first be checked for phase wraps.

Visualization of PCMRI based velocity maps can be affected due to the presence of background phase noise. Thresholding using magnitude image information is a common method applied to suppress background noise for improved flow region visualization[11]. Zwart and Pipe proposed a multidirectional velocity encoding method which used multiple flow encoding directions and a single low VENC to improve the velocity to noise ratio (VNR) [95]. The mutual information among the different velocity encoding directions was used to correct for velocity aliasing. These multiple flow encoding directions can also be used to improve noise suppression and distinguish background noise from stationary tissue and flow regions. For typical 3D

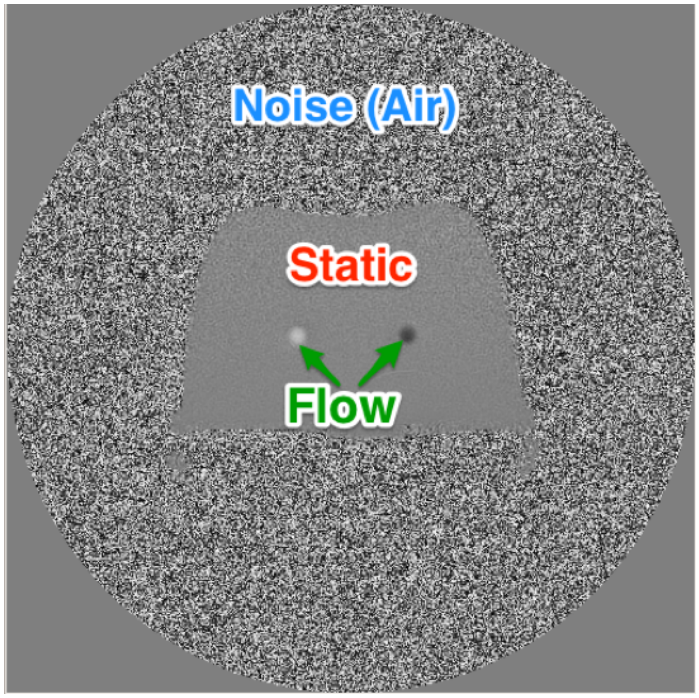

Figure 3.5: Example phase contrast MRI image using a flow phantom, with the regions representing background noise, no flow and directional flow highlighted as shown.

volumetric data acquisitions, the unwrapping algorithms are computationally intensive. In such cases, a flow mask can be useful in reducing the number of voxels that need to be unwrapped, by identifying the flow regions in an imaging volume. The objective of the proposed method of identifying flow regions is not to achieve accurate segmentation, but to be able to identify all flow voxels in a volume and reduce computational time of the phase unwrapping approach used by Zwart and Pipe [95].

3.2.1 Differentiation of voxel characteristics

Phase contrast MRI based velocity maps have three distinct regions (noise, static, and flow) as highlighted in Fig. 3.5. A single voxel representation of the three regions is shown in Fig. 3.6. The first stage in the mask development was the suppression

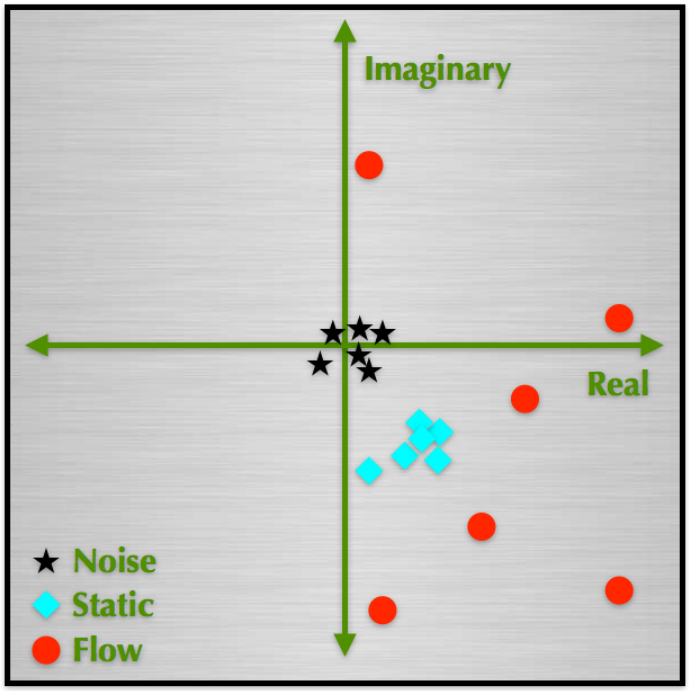

Figure 3.6: A single voxel from an example volunteer dataset representing the three distinct regions in a phase contrast image, measured along the six flow encoding directions is shown in the complex plane.

of background noise. The reconstructed complex image and the noise variance were used for this purpose. A T-test comparing the means of real and imaginary channel of the reconstructed complex data to zero independently, was used to determine if a voxel could be characterized as noise. The output of the hypothesis testing is a binary dataset with voxel value 0 if noise or voxel value 1 if signal. The binary mask was then multiplied with the phase difference dataset. The second stage was to identify flow regions from the non-zero voxels in the phase difference dataset. The standard deviation of phase noise is inversely proportional to the SNR of the magnitude image. A Chi square test was performed comparing the phase deviation across different velocity encoding directions to the standard deviation of phase noise in a voxel. The

SNR	NL = 90	NL = 95	NL = 98
1	29.55%	40.73%	54.84
2	0.14%	0.35%	1.00%
5	0.00%	0.00%	0.00%
10	0.00%	0.00%	0.00%

Table 3.2: Fraction of pixels incorrectly characterized as noise for varying values of SNR and noise masking confidence levels (NL).

addition of the noise and flow masks constituted a tri-level mask with 0 representing noise, 1 representing static tissue and 2 representing flow regions.

3.2.2 Numerical Simulations: Methods

A complex gaussian noise dataset was simulated with zero mean and known standard deviation. This dataset was used to test the performance of the noise mask by verifying the number of output non-zero voxels were equal to residual value for each confidence level. The test for identifying flow regions comprised of another synthetic dataset that simulated phase variation in one dimension, and magnitude variation from 0 to $3\sigma_{noise}$ in the second dimension. Complex gaussian noise with zero mean and standard deviation σ_{noise} was added to the synthetic dataset.

The effect of SNR on mask performance was evaluated using a simulated data with a constant signal magnitude over the entire field of view. Complex gaussian noise of known standard deviation was added to the K-space data to generate images with SNR equal to 1, 2, 5, and 10. The performance of the mask was evaluated by the fraction of pixels incorrectly characterized as noise by the proposed algorithm.

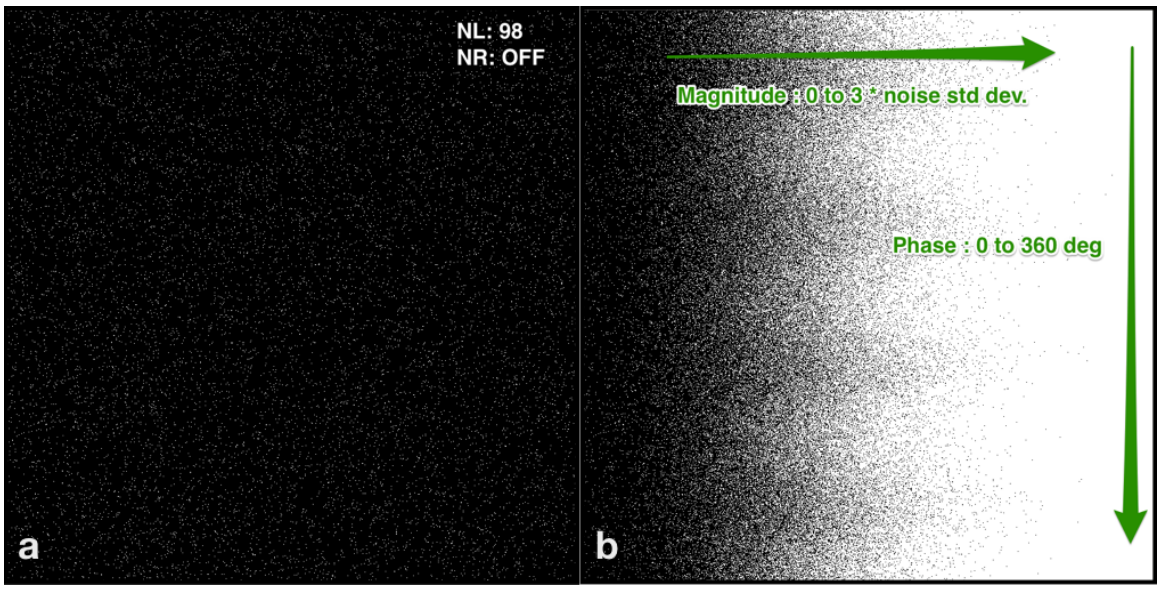

Figure 3.7: Tri-level mask performance on (a) simulated noise; (b) simulated phase variation with additive gaussian noise. NL (noise level) represents the threshold for the t-test hypothesis, and NR (noise refinement) represents the the umber of iterations of binary opening performed on the output of the mask.

3.2.3 Numerical Simulation: Results

Figure 3.7a shows the output of the mask on simulated complex gaussian noise with known standard deviation. The noise mask was set at 98% confidence level. The number of voxels the were not masked out were found to be 1.9% of the imaging volume, which was close to the expected performance error of 2%. The mask performance with phase variation in the presence of noise is shown in Fig. 3.7b. The mask was most sensitive at phase values of $0^o, 90^o, 180^o, 270^o$, and 360^o. The mask was least sensitive when the real channel was the same as the imaginary channel. The mask was likely to detect noise if either the real channel or the imaginary channel was noise. The noise mask had a performance error of 4.9% for a confidence level of 95%, and a performance error of 9.7% for a confidence level of 90%.

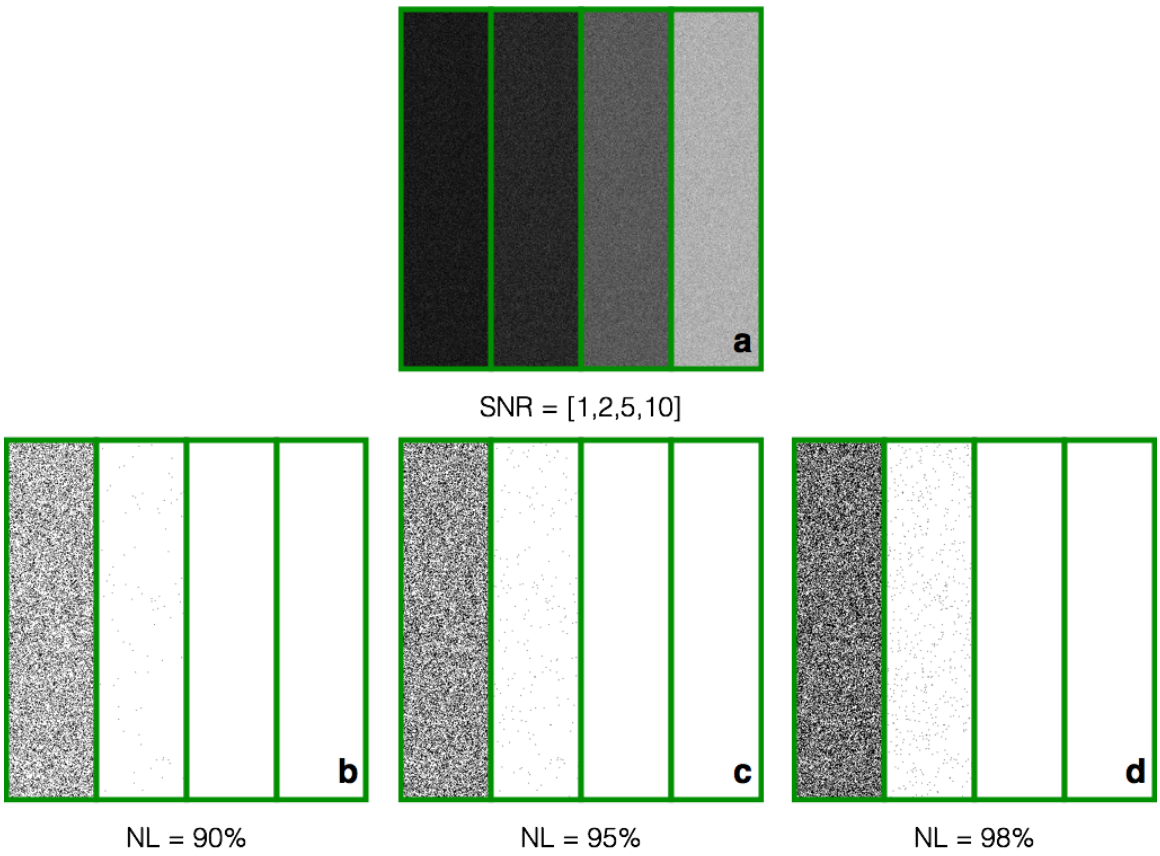

Figure 3.8: (a) Numerical simulation of signal with additive gaussian noise for SNR values of 1, 2, 5 and 10 (left to right). The performance of the noise mask for the four SNR values at (b) noise masking confidence level (NL) of 90%, (c) noise masking confidence level (NL) of 95%, and (d) noise masking confidence level (NL) of 98%.

The performance of the mask for SNR values of 1, 2, 5 and 10 is shown in Fig. 3.8. At low SNR the likelihood of identifying a false positive in the case of noise masking was higher than at a higher SNR. The mask performance error with changing SNR is depicted in Table 3.2. For an SNR or 2 and more, it is clearly evident that the mask is accurate in differentiating between signal and noise. For SNR < 2, many pixels were incorrectly identified as noise. Since the flow region identification depends on

phase deviations, pixels identified as noise in the first stage of the mask algorithm, have a high likelihood of being categorized as regions with flow.

3.2.4 Phantom Experiments : Methods

A gravity feed based flow phantom was used to acquire phase contrast data. The design specifications of the flow phantom are provided in Appendix A. A 3D stack of spiral trajectory was used to acquire data with 6 velocity encoding directions. Other MR acquisition parameters were: TE/TR = x ms / 29 ms, $\theta = 10^o$, FOV_{XYZ} = 150 mm x 150 mm x 60 mm, Δx x Δy = 0.8 mm x 0.8 mm x 0.8 mm. The flow in the phantom was along the FH direction. The peak velocity was determined to be 9 cm/s. V_{enc} was set at 15 cm/s. Data were acquired using a birdcage coil and the reconstruction was performed in GPI. Noise images were reconstructed from the acquired data as described in section 3.1. The reconstructed low resolution scaled noise, reconstructed complex data, and phase difference data were input to the tri-level mask algorithm to obtain the noise and flow masks. Tri-level masks were obtained for all possible combinations of noise confidence levels $(90\%, 95\%, 98\%)$ and flow confidence levels $(90\%, 95\%, 98\%)$. Different morphological image processing techniques (binary opening after noise stage, binary dilation after flow stage) with user discretion, were applied after each stage of the algorithm, to improve the mask performance. A standard 3x3 structuring element was used for morphological image processing.

3.2.5 Phantom Experiments: Results

The velocity maps and the corresponding output of the tri-level mask algorithm are shown in Fig. 3.9(a,b) for sagittal slice orientation and in Fig. 3.9(c,d) for axial slice orientation. The mask algorithm was able to identify background noise, regions

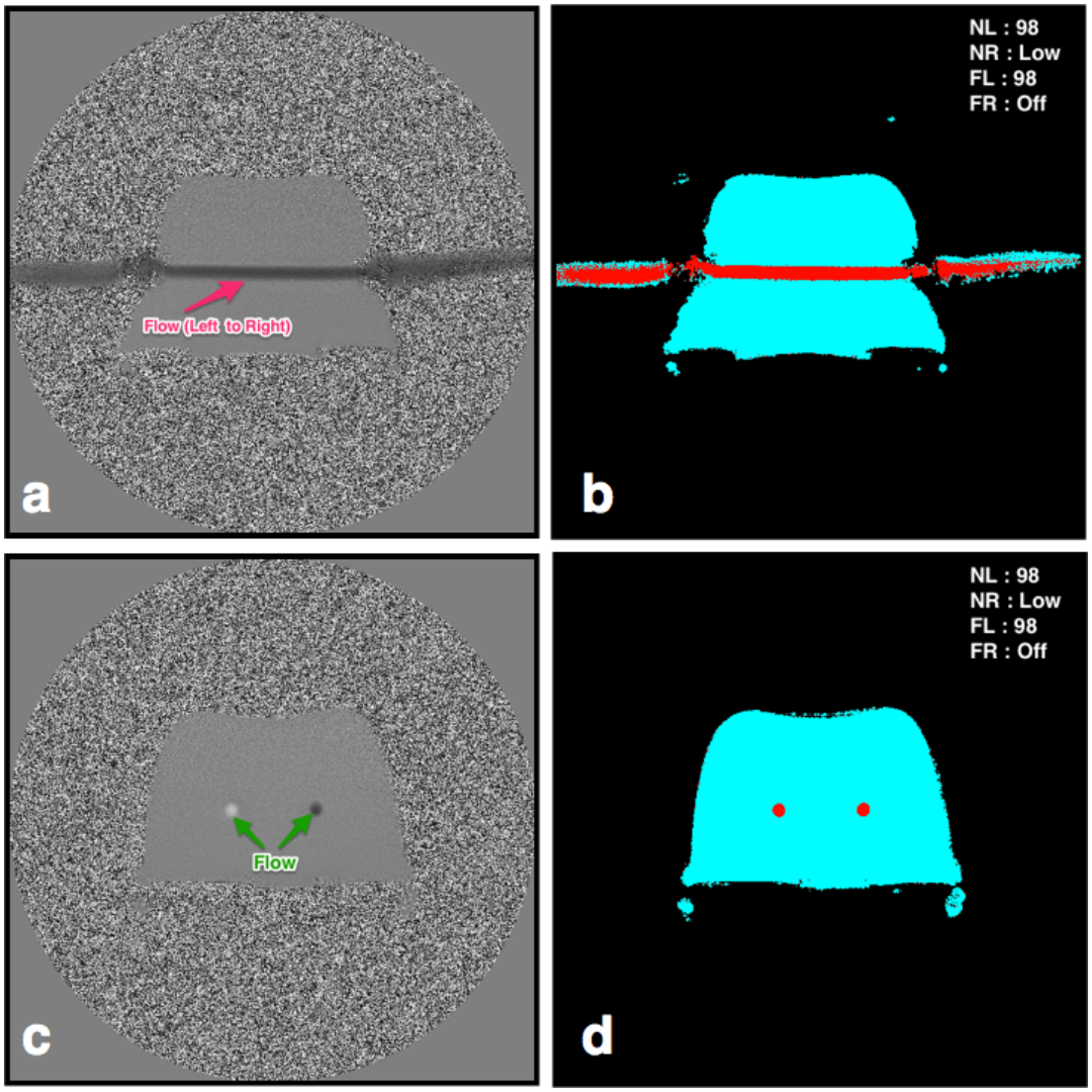

Figure 3.9: Flow phantom data were obtained using 6 directional flow encoding. (a) Velocity map obtained using sagittal slice orientation with flow in the left-right direction; (b) Tri-level mask output for sagittal slice orientation with noise masking at 98% confidence level and flow region identification at 98% confidence level. One iteration of binary opening was performed on the noise mask; (c)Velocity map obtained using axial slice orientation with flow into and out of the image; (d)Tri-level mask output for axial slice orientation with noise masking at 98% confidence level and flow region identification at 98% confidence level. One iteration of binary erosion was performed on the noise mask. [Black/0 : Noise, Blue/1 : No flow, Red/2: Flow]

without and with flow successfully for both slice orientations. Spurious noise voxels were masked out after performing one iteration of binary erosion.

3.2.6 In Vivo Experiments: Methods

Three sets of volunteer data were acquired using 3D stack of spiral trajectories with 6 directional velocity encoding. Other MR acquisition parameters were: TE/TR = x ms / 19 ms, $\theta = 10^o$, FOV_{XYz} = 240 mm x 240 mm x 80 mm, Δx x Δy = 0.8 mm x 0.8 mm x 0.8 mm. V_{enc} was set at 80 cm/s. Data were acquired using a birdcage coil and the reconstruction was performed in GPI. Noise images were reconstructed from the acquired data as described in section 3.1. The reconstructed low resolution scaled noise, reconstructed complex data, and phase difference data were input to the tri-level mask algorithm to obtain the noise and flow masks. Tri-level masks were obtained for all possible combinations of noise confidence levels $(90\%, 95\%, 98\%)$ and flow confidence levels $(90\%, 95\%, 98\%)$. Different morphological image processing techniques (binary opening after noise stage, binary dilation after flow stage) with user discretion, were applied after each stage of the algorithm, to improve the mask performance. A standard 3x3 structuring element was used for morphological image processing. A representation of the flow region sparsity in the image volume was provided by the flow region volume fraction. The flow region volume fraction was calculated as the ratio of the number of flow voxels to the total number of voxels in the image volume.

3.2.7 In Vivo Experiments: Results

The reconstructed velocity maps for flow component in the slice direction for the three volunteers is shown in Fig. 3.10(a-c). For each of these volunteers the tri-level mask output was computed (Fig. 3.10(d-f)) and the corresponding velocity magnitude

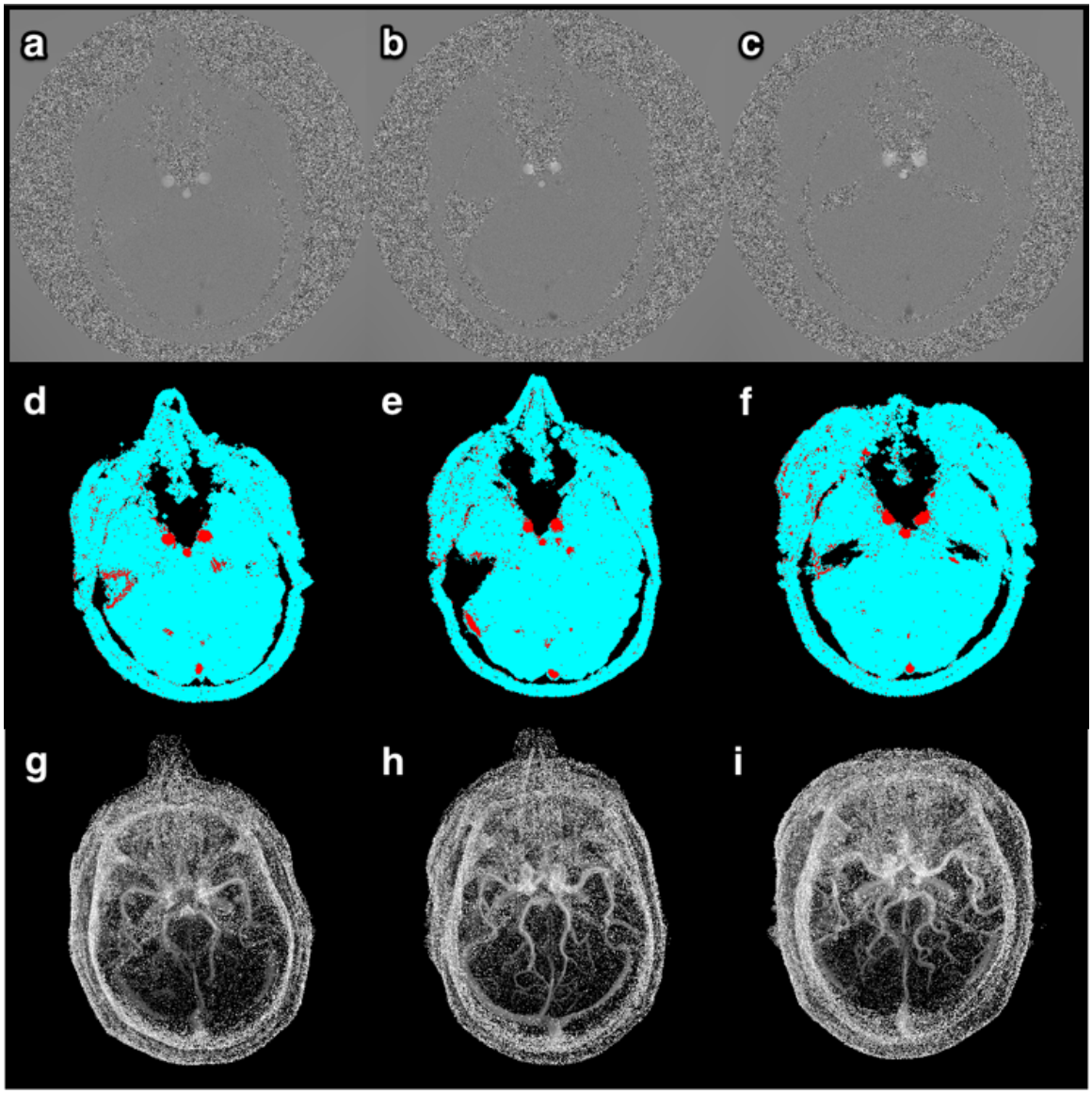

Figure 3.10: In vivo data from three volunteers were obtained using 6 directional velocity encoding. (a-c) Velocity maps of an axial slice are shown for the three volunteers; (d-f) Tri-level mask output corresponding to the three volunteers for an axial slice orientation with noise masking confidence at 98%, and flow identification confidence at 90%. Three iterations of binary opening were performed on the noise mask; (g-i) Flow masked maximum intensity projections along slice direction for the three volunteers provide information on the velocity magnitude within the flow regions.

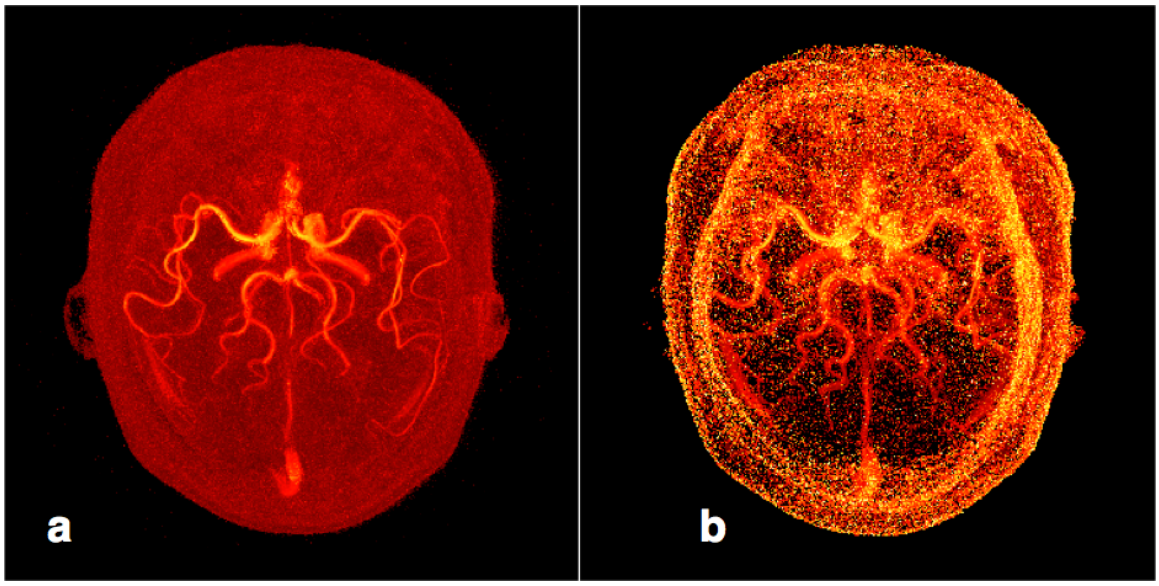

Figure 3.11: (a) Magnitude masked speed MIP; (b) Tri-level masked speed MIP

maximum intensity projections (MIPs) along the slice direction were also generated by first computing the flow masked velocity magnitude from the individual velocity component maps and then collapsed with respect to the maximum value in the slice direction, as shown in Fig. 3.10(g-i). The background noise across all volunteers was effectively suppressed by the mask algorithm, and repeatability of the algorithm to identify flow regions among in vivo data was also observed. The sporadic distribution of isolated flow voxels at the edge of the brain image can be attributed to the low SNR of the magnitude image at the edge of the field of view in the slice direction (Fig. 3.11b). The flow region volume fraction was estimated at 2.3% for the MIP shown in Fig. 3.11b.

3.2.8 Discussion

Conventional approaches for flow visualization employ magnitude based thresholding of the phase difference reconstructed maps to suppress background noise [8, 12]. Static tissue suppression for cine PCMRI sequences has been achieved using the

through time standard deviation of voxel phase [86]. A new method for voxel characterization as noise, static tissue or flow is presented using the noise statistics estimated in section 3.1 in conjunction with signal magnitude and phase deviations. The method was evaluated for PCMRI data obtained using 3D spiral acquisitions with multidirectional velocity encoding. The purpose of the mask algorithm was not intended to produce highly accurate flow segmentation, but produce a sufficiently sparse image volume to reduce the number of voxels that would require phase unwrapping. Hence, static tissue voxels inaccurately classified as flow were less concerning than flow voxels erroneously identified as background noise or static tissue.

The mask performance was evaluated with noise and signal simulations at different SNR and statistical confidence levels. The mask was observed to successfully distinguish the three regions for SNR $\geq$ 2. The mask was able to ascertain flow regions irrespective of the slice orientation and direction of flow. The ability of the mask to distinguish between noise and flow regions was affected when SNR was less than 2. This performance issue was observed primarily at the edge of the field of view in the slice direction. Morphological image processing was used to improve the performance of the mask in background noise suppression and ensuring that edge voxels of the vessels were accurately identified as flow regions. The noise suppression stage of mask development incorporated a 3x3 structuring element to remove isolated noise pixels in the background by first performing binary erosion followed by binary dilation of the mask. A single iteration of erosion was determined to be sufficient in noise removal and a single iteration of dilation was performed to minimize the loss of edge signal pixels from the erosion stage. The flow region identification stage of mask development utilized one iteration of binary dilation using the same 3x3 structuring element used in the noise suppression stage. Dilation was used to include additional pixels around the flow periphery regions ensuring that all pixels corresponding to

vessels were included in the mask. The disadvantage of using binary dilation to refine the flow mask was that a small fraction of pixels ($\approx 10\%$) corresponding to static tissue may be misclassified as flow regions in the mask. This is expected to result in a small increment in the computation time of the phase unwrapping algorithm, but not substantial enough to negate the speedup in phase unwrapping obtained as a result of the mask. A noise mask confidence level (NL) of 98 was identified as the optimal masking level for background noise suppression. A single iteration of binary erosion was observed to be sufficient to suppress all of the background noise for NL = 98. The optimal flow identification confidence level (FL) was determined to be 90. At this level, a single iteration of dilation was sufficient to include all the vasculature in the mask. The performance of the mask is dependent on statistical power for both noise and flow identification. Increasing the number of flow encoding directions is therefore expected to improve the mask performance. However, this approach would invariably increase scan time and therefore is not ideal. Six velocity encoding directions was determined to be the optimal number according to Zwart and Pipe [95].

The proposed approach is expected to reduce the computational time of the phase unwrapping algorithm significantly as a result of the reduced flow region fraction in the imaging volume. The proposed tri-level mask development could be used for flow visualization, and for estimating background phase. This work did not explore the mask refinement with respect to these applications but will be part of future development.

3.3 Application to phase unwrapping : Improvements using the tri-level mask

The accuracy of flow quantification using PCMRI based approaches can be affected by phase aliasing. Phase aliasing occurs when the measured velocity component is greater than the maximum encoded velocity denoted by V_{enc}. Since the dynamic

range of phase differences is bounded by [-π, π], phase differences values outside this range get wrapped into the dynamic range providing an incorrect velocity estimate. Phase unwrapping can be performed prospectively, or as part of post processing. A common prospective approach to correct for phase wraps has been proposed by Lee et. al [44], where the authors recommend the acquisition of high and low V_{enc} datasets to remove phase aliasing while maintaining a high velocity to noise ratio (VNR). An example of a post processing approach to phase unwrapping is provided by Loecher et. al [46] incorporating spatial and temporal continuity with minimal user intervention. The work by Untenberger et. al [85] also utilizes phase continuity in the temporal direction to unwrap phase. The algorithm used in this work was proposed by Zwart and Pipe [95], where unwrapping was performed by identifying the most consistent solution to the reconstructed velocity estimate in a two dimensional or three dimensional solution space.

The tri-level mask algorithm presented in section 3.2 can be used to only output the flow regions. This binary dataset is termed the flow mask, and is then used with the phase difference maps to only check those voxels in the volume that correspond to a non-zero value on the flow mask, for phase wraps. The unwrapped flow voxels are then combined with the original phase difference map prior to velocity estimation. This process was implemented on all acquired in vivo datasets. The motivation of this work was to reduce the computation time of the phase unwrapping approach used in [95].

3.3.1 Data Acquisition and Implementation

Six volunteer datasets were obtained using 3D stack of spiral trajectories with 6 directional velocity encoding. Other MR acquisition parameters were: TE/TR = x ms / 19 ms, $\theta = 10^o$, FOV_{XYz} = 240 mm x 240 mm x 80 mm, Δx x Δy = 0.8 mm

x 0.8 mm x 0.8 mm. V_{enc} was set at 30 cm/s. Data were acquired using a birdcage coil and the reconstruction was performed in GPI. The tri-level mask was obtained as described in section 3.2.

The tri-level mask was modified to generate a binary mask (flow mask) with nonzero voxels representing flow regions within an imaging volume. The phase difference data for each of the six flow encoding directions were multiplied with the flow mask. The phase unwrapping approach described in [95] was implemented in GPI. Phase unwrapping was performed on the phase difference datasets with and without the application of the flow mask. The velocity estimates were obtained for the unaliased phase difference data with and without the masks. The difference of the two velocity estimate maps was performed to observe the effects of flow masking the phase difference data. The phase unwrapping algorithm execution times were noted in GPI for both instances. A flowchart of the approach is provided in Fig. 3.12.

The time improvements due to the application of the mask were quantified by a speed-up factor called Fractional Unwrapping Speed-up (FUS) defined as

$$FUS = \frac{time\,without\,mask}{time\,with\,mask} \tag{3.7}$$

The unaliased velocity maps in each of the six directions were visually assessed for errors in unwrapping using the mask.

3.3.2 Results and Discussion

The unaliased phase difference data with and without the mask are shown in Fig. 3.13. The performance of the flow mask can be explained with reference to three specific cases of phase aliasing in the example in vivo dataset. For both elliptical ROIs (denoting flow regions along different flow encoding directions), the performance of the phase unwrapping algorithm was not affected by the use of the flow mask or without

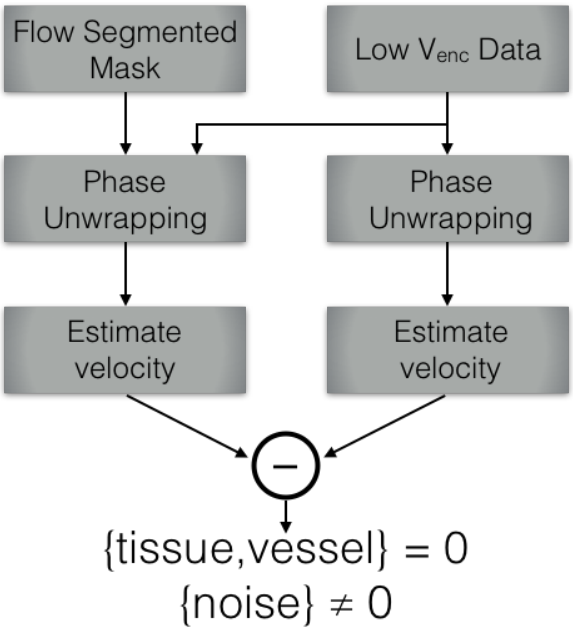

Figure 3.12: Algorithm to determine the performance of the unwrapping algorithm with and without the mask.

its use. The red arrow is used to represent static tissue in the phase difference data (Fig. 3.13A). Without the use of the mask some of the voxels in this region were falsely identified as flow regions with phase aliasing and underwent unwrapping, as observed along the v_3 direction in Fig. 3.13B. On application of the flow mask, these regions were identified as static tissue and did not undergo phase unwrapping (Fig. 3.13C). The FUS (mean $\pm$ σ) was determined to be 33.26 $\pm$ 1.47. The average fraction of flow voxels in the image volume for volunteer datasets was 3%. The FUS was observed to be inversely proportional to the fraction of voxels checked for phase aliasing.

Phase unwrapping is essential for accurate quantitative flow estimation using PCMRI but can be computationally expensive for high resolution 3D datasets. The tri-level mask provided two distinct improvements to the performance of the phase unwrapping algorithm. The primary improvement was faster execution of the phase

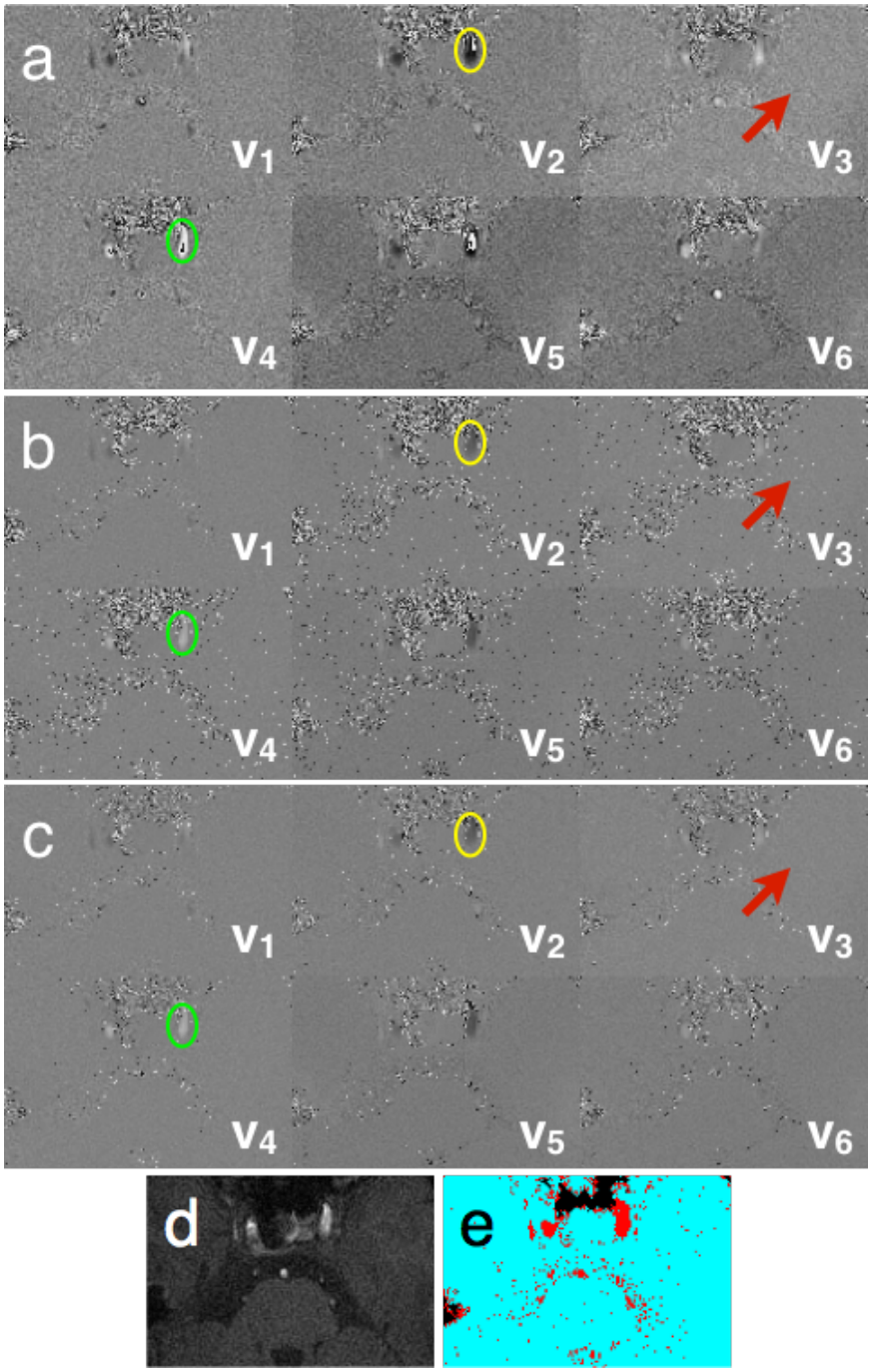

Figure 3.13: This figure compares the output of the phase unwrapping algorithm with and without the use of the tri-level mask. The elliptical ROIs for each color highlight a specific case of phase aliasing, and the corresponding output of phase unwrapping with and without the mask. The arrow highlights the additional improvement provided by the mask in distinguishing between static tissue and vasculature.

unwrapping algorithm by a factor of 33x, as a result of the sparsity of the flow regions within an imaging volume. The second improvement mitigated the incorrect unaliasing of static tissue phase in regions with low SNR, resulting in inaccurate velocity estimates.

3.4 Conclusion

A new approach to improve the execution speed of phase unwrapping of data acquired using multidirectional flow encoding was discussed. The proposed approach consisted of three stages of development. The first stage introduced a novel method to estimate noise statistics from a single fully sample spiral acquisition. The algorithm was integrated into the gridding reconstruction pipeline by appropriate weighting and scaling of the density compensation coefficients to concurrently produce the reconstructed image and a low resolution noise dataset. The statistics of the reconstructed noise were found to be comparable to the noise measured using a noise dynamic scan on the fully sample data.

The second stage incorporated the noise statistics, image magnitude data, and phase deviation from the phase difference maps to generate a tri-level mask that could successfully identify and separate background noise, static tissue, and the vasculature in the acquired image volume. The flow regions fraction of the imaging volume was found on average to represent only 2% of the entire image volume. The mask was also able to provide sufficient noise and static tissue suppression while generating speed MIPs.

The tri-level mask was used in the final stage of development to check for aliased phase only in the voxels classified as flow by the mask. This increased GPI execution speed of the phase unwrapping algorithm on average by 33 times. The mask was

also able to mitigate the fraction of incorrectly unaliased voxels, most of which were associated with the static tissue region.

Chapter 4

RF SATURATION INDUCED BIAS IN AQUEDUCTAL CEREBROSPINAL FLUID FLOW QUANTIFICATION USING CINE 2D PCMRI

Phase contrast magnetic resonance imaging has been the method of choice for quantitative flow imaging. Although technical advancements in PCMRI have primarily focussed on cardiovascular applications, there exists a growing interest in its use in the study of disorders attributed to alterations in CSF flow dynamics. Cerebrospinal fluid is a clear liquid primarily produced in the choroid plexus, and present in the brain ventricles and subarachnoid space. Cerebrospinal fluid flow dynamics are critically important in maintaining intracranial pressure and neuronal metabolic activity. Cerebrospinal fluid flow dynamics are complex, with an oscillatory component governed by the cardiac cycle, and a bulk flow component associated with the circulation and reabsorption of CSF in the jugular venous system [72, 77]. The cerebral aqueduct is considered as an important region of interest to ascertain the validity of PCMRI based CSF flow quantitation, particularly with respect to characterizing hydrocephalus. Although PCMRI is sufficiently sensitive to quantify the oscillatory flow component, imaging bulk flow has been a problem, especially in the cerebral aqueduct. System limits may inhibit the use of large gradient moments to achieve, in some cases, sufficient sensitivity to accurately measure slow flow.

Phase contrast MRI has several known challenges. The accuracy of flow quantification is affected by concomitant field effects that can be accurately characterized and compensated [10]. Eddy current based phase offsets can be highly problematic for slow CSF flow due to large gradient lobes used for slow flow sensitization. Eddy current based phase offset compensation can be achieved by a polynomial fit of

the background stationary phase [86], estimating the phase offset using a stationary phantom [22], or using a field camera to monitor spatiotemporal phase variations [24]. Motion artifacts are also a cause for concern for PCMRI data acquired using Cartesian trajectories. Artifacts due to pulsatile flow observed in Cartesian acquisitions can be mitigated using non-Cartesian acquisitions [56, 57]. In this work, the in vivo data were collected using spiral trajectories to mitigate these effects. In addition, the aqueduct has a diameter of 2 - 3 mm in adults, requiring high spatial resolution during data acquisition to minimize partial volume effects [83]. Apart from these sources of error, RF saturation effects could result in a bias in estimated velocities using 2D PCMRI which, to our knowledge, hasn't been explored in detail before.

The velocity distribution of spins in a voxel causes each spin to experience a velocity dependent number of successive RF excitations as part of the gradient echo sequence before it exits the excited slice. The slower spins are saturated to a greater extent than the faster spins in a voxel, biasing the signal weighted estimate of mean velocity in that voxel towards the faster moving spins in that voxel. This effect is a positive bias and increases as the velocity distribution becomes larger within a voxel. The focus of this work is to gain a better understanding of the influence of MR acquisition parameters on the extent of RF saturation induced bias on CSF flow quantification.

An important clinical utility of CSF flow imaging has been in the study of patients with normal pressure hydrocephalus (NPH). PCMRI based CSF flow quantification in patients with NPH has undergone extensive research, with some studies determining that adults diagnosed with NPH with hyper-dynamic CSF flow rates respond well to the ventriculoperitoneal shunting procedure [13]. This hyper-dynamic CSF flow results in higher aqueductal CSF stroke volume (ACSV) [13, 78]. Interestingly, while some of the previous work show correlation between PCMRI based CSF flow estimates

and the outcome of diagnosing NPH patients or evaluating NPH patients' successful response to shunts [47, 78, 92], there have also been studies that have stated that flow estimates obtained from PCMRI may not be solely used in successful shunt response determination, or in evaluating shunt patency [2, 38]. The use of different MR acquisition parameters in these studies relate to the investigation of RF saturation induced bias in CSF flow quantification presented in this work. It is important to note that variations in MR acquisition parameters are one among multiple factors potentially influencing the outcome of the reported studies.

This work considers CSF flow quantification errors due to variations in flip angle (θ), with the expectation that an increase in θ will increase the bias in regions with a large velocity spin distribution. Also, this particular source of error could contribute to the inconsistencies in reported results on using cine PCMRI in studies involving NPH patients. The first section introduces theoretical background on the dependance of signal saturation on the velocity distribution. Section 4.2 provides information on the experimental setup for data acquisition and analysis in a gravity feed based flow phantom and the cerebral aqueduct in healthy volunteers. Sections 4.3 and 4.4 sections present arguments supporting the effects of RF saturation on CSF flow quantification and its relevance to clinical applications.

4.1 Theory

A mathematical model incorporating the effects of RF saturation is developed for steady flow as a function of spin velocity. The bias introduced is shown to be dependent on slice thickness (Δz), repetition time (TR), and flip angle (θ). Equation 4.1 describes the saturation effects on the signal (S_v) from a spin moving through a Δz thick slice approximated by a decaying exponential. Assuming the spin travels

with uniform velocity (v), and takes time ($T = \Delta z/v$) to travel through the slice,

$$S_v \approx \int_0^T e^{-t/TA} dt = TA(1 - e^{-T/TA}), \tag{4.1}$$

ignoring T1 recovery and defining

$$TA = \frac{-TR}{ln(cos\theta)}. \tag{4.2}$$

The variable TA is defined as the time constant describing the rate at which magnetization is removed from the system by RF pulses, and was introduced by Pipe and Robison [69]. The relative signal magnitude of a voxel, incorporating the effects of saturation due to the velocity spin distribution, is obtained using Eq. 4.3.

$$S = \int_{voxel} \frac{1 - e^{-V_0/v}}{V_0/v} e^{\frac{-i\pi v}{Venc}} dv, \tag{4.3}$$

where

$$V_0 = \frac{\Delta z}{TA}. \tag{4.4}$$

V_0 is called the critical velocity, and can be interpreted as the velocity below which spins experience substantial saturation effects. The integrand of Eq. 4.3 (S_v) was used to theoretically portray effects of saturation as a function of estimated velocity (Fig. 4.1a). For different values of V_0 calculated using Eq. 4.4 and MR acquisition parameters from referenced literature [2, 35, 76, 82, 88], the effect of saturation increased with increasing V_0, for a given velocity estimate v. The choice of θ for the phantom and volunteer experimental sets was determined based on the range of V_0 values used in these studies (Fig. 4.1b).

Relative signal is defined as the ratio of signal magnitude from stationary spins to that from flow spins. Edge voxels of the cerebral aqueduct that contain part CSF flow and part stationary tissue exhibit a decrease in the relative signal values (0.5 to 0.2) as θ increases from 10^o to 30^o. Increasing θ saturates the stationary tissue to a

greater extent and also increases the signal from CSF flow, as shown in an example in vivo dataset (Fig. 4.2). Incorporating the contributions of partial volume in Eq. 4.3 introduces a velocity bias at the edge voxel that is supplemental to the bias introduced from RF saturations effects, as shown in Fig. 4.1(c-f). Figure 4.1c and Fig. 4.1d show the individual effect of partial volume and RF saturation on velocity estimates with increasing partial volume fraction (pv) of CSF flow. The combined effect of RF saturation and partial volume is shown in Fig. 4.1e. The velocity estimate bias (v_{30^o} - v_{10^o}) for all three contributions is shown in Fig. 4.1f. While partial volume only influences velocity bias at the edge voxel, RF saturation contributes to velocity bias at the edge voxel and flow voxels with spin velocities less than V_0.

4.2 Methods

RF saturation effects were studied in a flow phantom and in the cerebral aqueduct of healthy volunteers. The data for all experiments were collected on a 3.0T Philips Ingenia scanner. Cartesian data were reconstructed on the scanner and the complex images exported to a workstation for further analysis. Data reconstruction for spiral scans, and the analysis of all data were performed on an offline workstation using GPI [96].

4.2.1 Phantom Experiment

Data were obtained using a gravity feed flow phantom, built in-house to create fully developed steady flow with laminar profile. The phantom consisted of two parallel cylindrical flow tubes each 45 cm long with an inner diameter of 3 mm, part of which were immersed in an enclosed water bath. The two tubes had flow in opposite directions, and satisfied the entrance length condition for fully developed laminar flow. The limiting peak velocity to maintain this condition was calculated to be 20

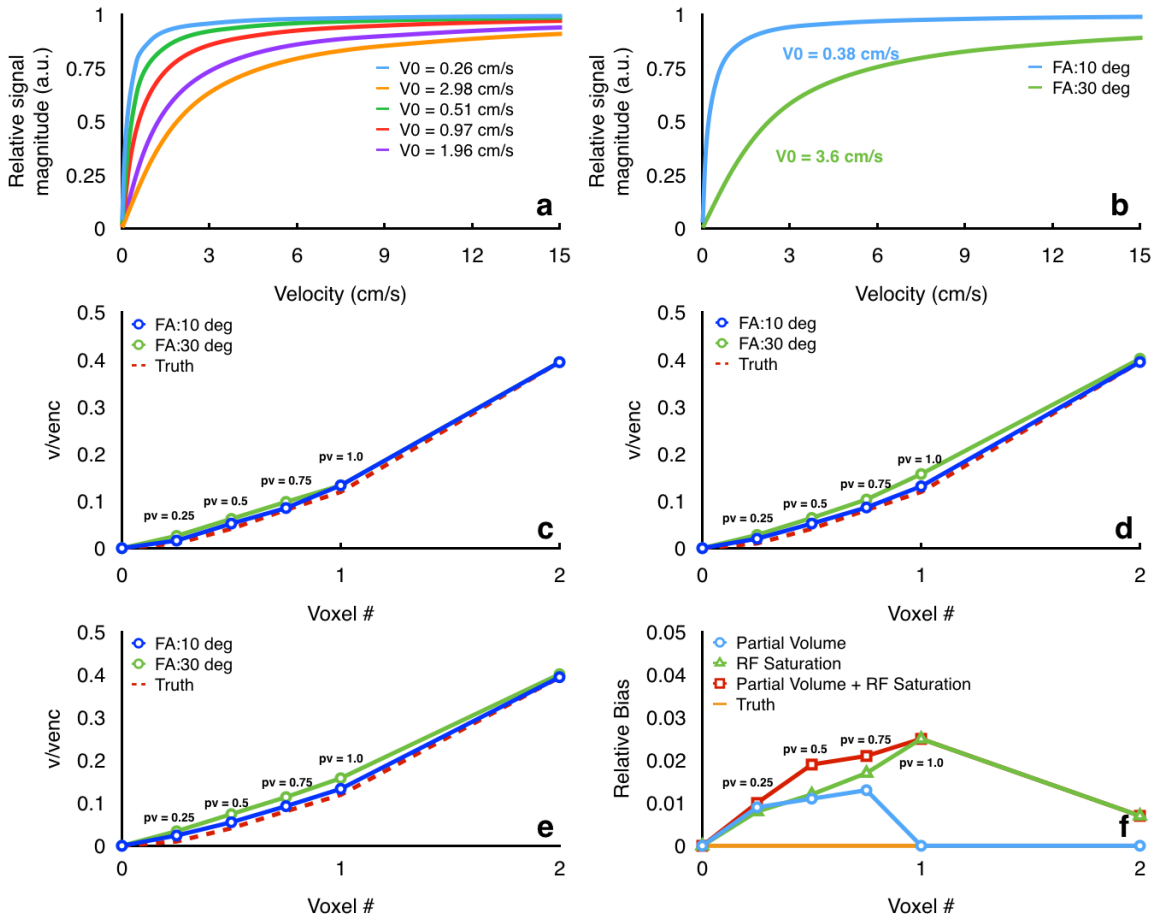

Figure 4.1: Extent of RF saturation effects (integrand of Eq. 4.3) as a function of (a) velocity, for different values of V_0, obtained from referenced CSF flow quantification studies; and (b) velocity, obtained in this work for flip angles of 10^o (V_0=0.38 cm/s), and 30^o (V_0=3.6 cm/s). The contribution from (c) partial volume effects only, (d) RF saturation effects only, and (e) combined effects of partial volume and RF saturation towards velocity bias is shown for varying values of fractional CSF spins in a voxel. The 'Truth' represents velocity estimates obtained without the presence of partial volume or RF saturation effects. (f) The bias for each of the cases shown in (c-e) was obtained as the difference in velocity estimates for the two flip angles. [In (c-f) *pv* stands for partial volume fraction]

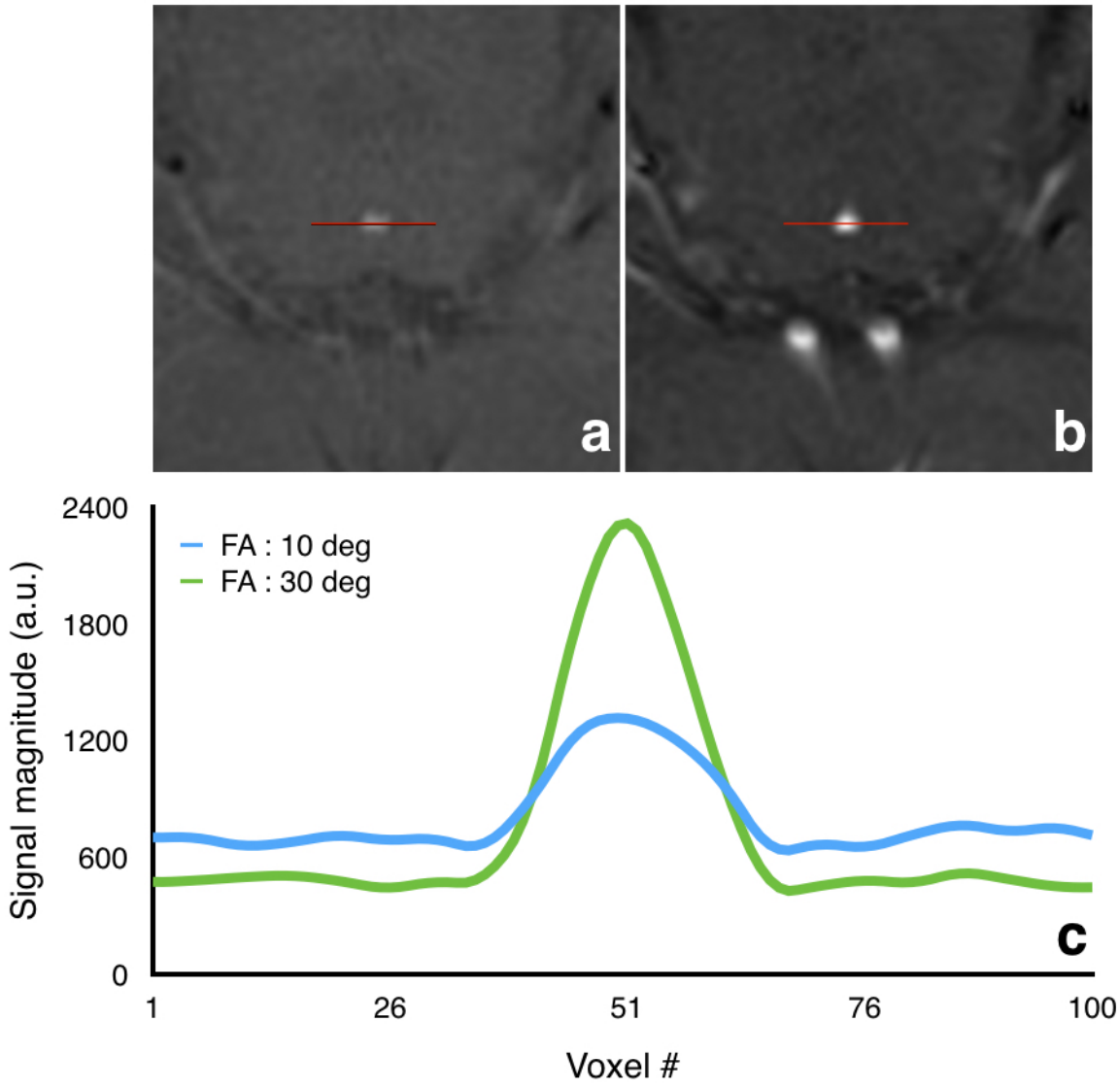

Figure 4.2: An example axial reconstructed magnitude image is shown for (a) $\theta = 10^o$, and (b) $\theta = 30^o$. The red line represents the 1D cross-section of the aqueduct used to obtain magnitude signal profiles for both flip angles as shown in (c).

cm/s. The flow phantom setup was determined to accommodate the observed range of CSF flow velocities, through the cerebral aqueduct among healthy adults from existing literature [6, 36, 64, 84]. A single experimental set consisted of obtaining data for $\theta = 10^o$, followed by the same protocol except $\theta = 30^o$. Repeated measures of the experimental set were obtained to determine variations in the velocity estimate. Flow information was obtained using a 2D Cartesian phase contrast scan with flow encoding enabled along the slice direction, and the following MR acquisition parameters: TE/TR = 6.9 ms/20 ms, in-plane resolution = 0.6 mm x 0.6 mm, slice thickness = 5 mm, NSA = 10, V_{enc} = 12 cm/s, FOV = 150 mm x 150 mm. The maximum gradient strength and slew rate were limited to 31 mT/m and 120 mT/m/s respectively.

4.2.2 Volunteer Experiment

Data were obtained from 6 healthy volunteers (5 male and 1 female) aged between 25 and 45 years. The cerebral aqueduct was used as the flow region of interest. The cerebral aqueduct was localized using a sagittal T2-weighted multislice TSE scan. The MR acquisition parameters for the sagittal localizer were TE/TR = 80 ms / 3000 ms, $\theta = 90^o$, in-plane resolution = 0.55 mm x 0.65 mm, slice thickness = 2 mm, FOV = 200 mm x 200 mm x 26 mm, TSE factor = 15, and the scan time was 2 minutes. An example slice of the sagittal localizer depicting the aqueduct is shown in Fig. 4.3a, where the highlighted region denotes the slice orientation of the cine phase contrast scan shown in Fig. 4.3b. Retrospectively cardiac gated 2D phase contrast MRI scans using a 2D spiral trajectory [70] with mixed interleaf ordering [68], were obtained for an angulated slice located orthogonal to the cerebral aqueduct, as prescribed in Fig. 4.3a. Data acquisition using a spiral trajectory was chosen for volunteer studies due to greatly reduced coherent artifacts from non-repeatable flow compared to data acquisition using a Cartesian trajectory. A single experimental set consisted

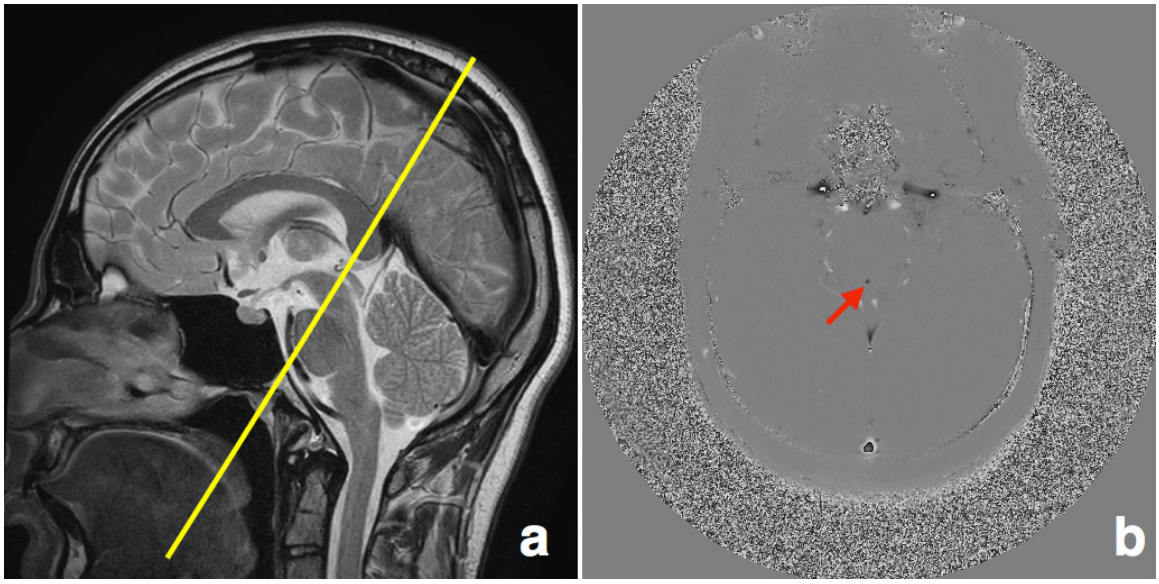

Figure 4.3: (a)T2 weighted midline sagittal localizer identifying the cerebral aqueduct. The yellow line denotes the angulation of the slice profile for the phase contrast scans. (b) Velocity map obtained from highlighting the flow through the aqueduct, which is identified by the arrow.

of obtaining phase contrast data for $\theta = 10^o$ followed by $\theta = 30^o$, with rest of the MR acquisition parameters being TE/TR = 4.2 ms / 30 ms, in-plane resolution = 0.6 mm x 0.6 mm, slice thickness = 5 mm, FOV = 240 mm x 240 mm, # of spiral interleaves = 63, V_{enc} = 12 cm/s with 16 cardiac phases. The maximum gradient strength and slew rate were limited to 31 mT/m and 120 mT/m/s respectively. Physiological waveform monitoring was performed using a Philips Peripheral Pulse Unit (PPU). Six repeated measures for the experimental set were obtained for each volunteer, to average the effects of variations in the velocity estimates. The total scan time for each volunteer was 12 minutes 36 seconds.

4.2.3 Data Analysis

For the flow phantom data, velocity maps were calculated after appropriate post-processing and phase corrections on the scanner, and the following analysis was performed in GPI. The flow region of interest (ROI) was identified using an iterative thresholding approach described in [75]. Student's T hypothesis testing was performed comparing the mean velocity on a voxel-by-voxel basis for $\theta = 10^o$ and $\theta = 30^o$, to identify regions with significant change in velocity estimates ($P < 0.05$).

For volunteer data, background phase error correction was implemented in GPI using the approach described by [86]. Static tissue regions were identified using the temporal standard deviation of the signal. A second order polynomial was used to fit the static phase and subtracted from the uncorrected phase difference maps to obtain the phase offset corrected maps. The velocity maps were obtained from the phase difference images using the prescribed value of V_{enc}. The flow ROI was identified using the approach described in [75]. Velocity difference (bias) maps for each volunteer were obtained by subtracting the velocity maps for $\theta = 10^o$ from $\theta = 30^o$ (averaged over the repeated acquisitions per volunteer). Changes in velocity estimates across the aqueduct cross-section were described by spatial velocity gradient maps and changes in velocity estimates over time in the voxel were described by the temporal velocity gradient maps. The spatial and temporal velocity gradient maps were calculated from the velocity maps using finite differences, and the spatiotemporal gradient maps were computed using the root-sum-of-squares of the spatial and temporal gradient components of the velocity estimates. Temporal variations over the cardiac cycle of the following flow metrics were generated for both values of θ: average velocity estimate at the center of the aqueduct, average velocity estimate at a single location on the aqueduct periphery, average flow rate, and aqueductal stroke volume. The average

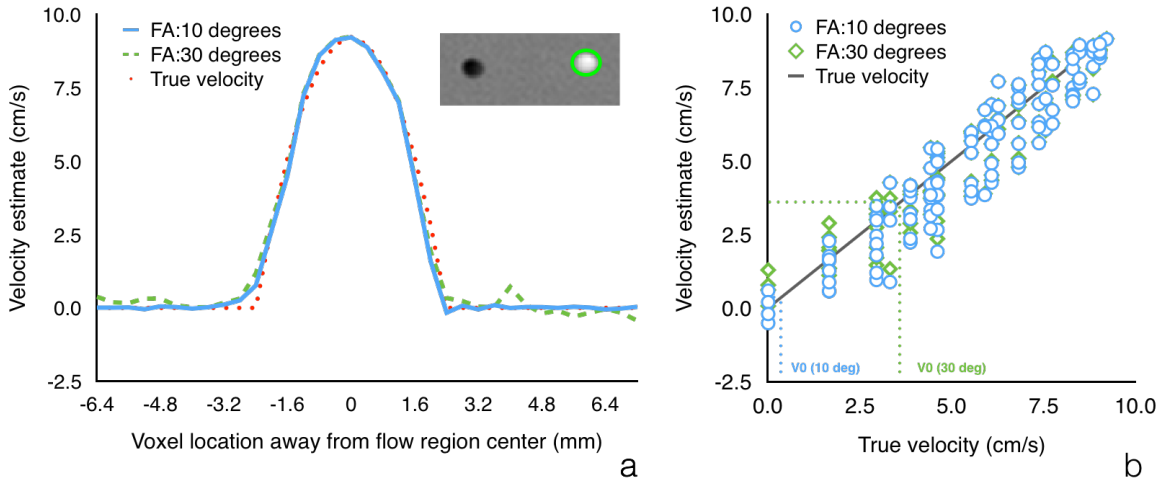

Figure 4.4: (a) Velocity profiles were obtained as a function of voxel location for fluid flow through the highlighted region of the velocity map. The average value of true velocity was calculated to be 4.6 cm/s. (b) Bias in measured velocity estimates when compared with the true velocities observed for velocity estimates lower than $V_0 = 3.6$ cm/s.

flow rate was calculated as a summation of the product of velocity estimate in a voxel and the voxel area, over all the voxels in the prescribed ROI. The aqueductal stroke volume was calculated as the average of the systolic and diastolic stroke volumes. The velocity difference maps were compared against the spatial, temporal, and spatiotemporal velocity gradient maps. A Wilcoxon signed rank test was performed comparing the aqueductal stroke volume estimates (combined across volunteers; $N = 36$) for $\theta = 10^o$ and $\theta = 30^o$.

4.3 Results

The measured velocity estimates are compared with the true velocity profile as shown in Fig. 4.4. Deviations from true velocity were observed for velocity estimates lower than V_0. Figure 4.5 shows the flow phantom velocity maps and p-value analysis

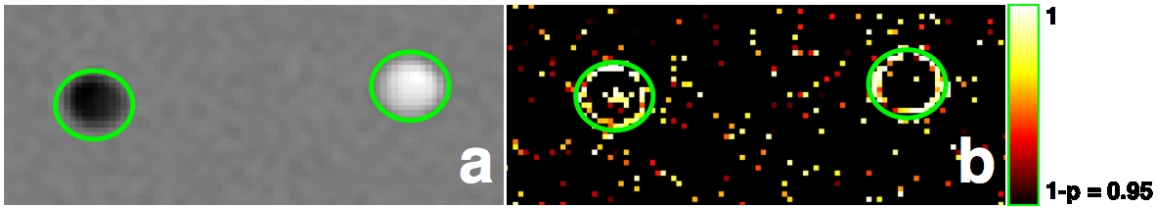

Figure 4.5: (a)Flow phantom axial slice velocity map; (b) P-value map of the same axial slice, showing regions with significant change in velocity estimates ($P < 0.05$), as a result of flip angle variation between 10 and 30 degrees. The flow regions have been identified by green circles.

showing regions with significant change in velocity estimates between $\theta = 10^o$, and $\theta = 30^o$. The flow regions were highlighted by the green ROIs. In Fig. 4.5b, the voxels with no significant change in velocity estimates were masked. Within the ROI, the majority of voxels undergoing a significant change in velocity estimate due to change in θ were concentrated at the flow region periphery.

The velocity map for one volunteer is shown in Fig. 4.3b. The cerebral aqueduct was identified as shown by the red arrow. Based on the flow encoding direction, negative velocity estimates corresponded to the diastolic phase of the cardiac cycle, and positive velocity estimates corresponded to the systolic phase of the cardiac cycle (Fig. 4.6a). During systole, the velocity difference (between $\theta = 30^o$ and $\theta = 10^o$ data) was observed to be positive and the difference magnitude increased until peak systole. Similarly, during diastole the velocity difference was observed to be negative and increased in magnitude until the peak diastolic phase of the cardiac cycle (Fig. 4.6b). The velocity estimate at the center of the aqueduct cross-section for $\theta = 10^o$ (Fig. 4.6a) is shown to provide a representative example on the CSF flow dynamics over the cardiac cycle. At peak systole and diastole, the contribution of spatial component was higher than the temporal component towards the spatiotemporal velocity gradient.

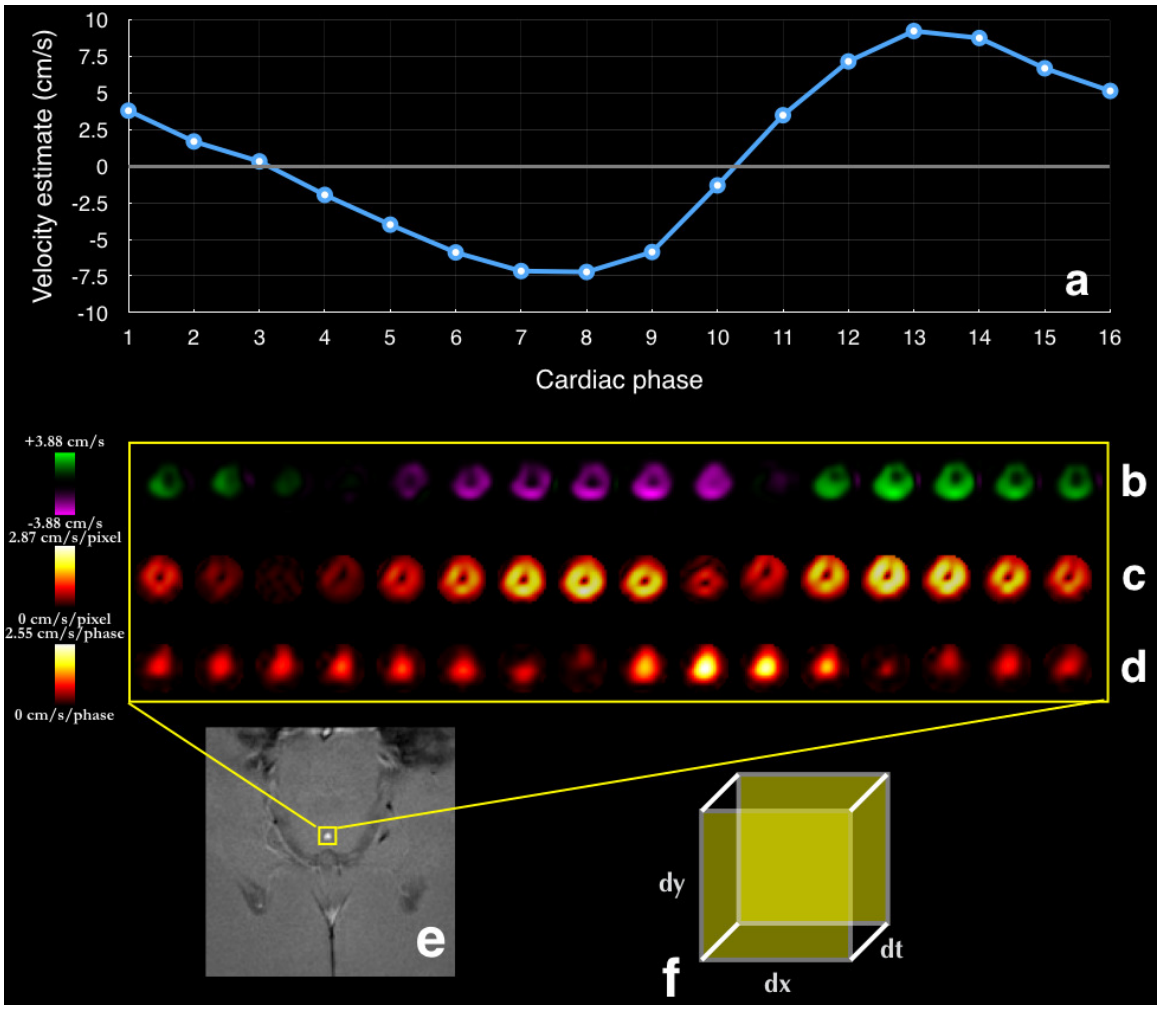

Figure 4.6: (a) Single voxel velocity estimate over one cardiac cycle; (b) Velocity difference map (FA:30 - FA:10); (c) Spatial velocity gradient; (d) Temporal velocity gradient; (e) Gradient echo magnitude image highlighting the flow region of interest (aqueduct); (f) Representation of the voxel dimensionality of in-plane resolution and temporal duration of each cardiac phase. The data were obtained for a single volunteer averaged over six experimental sets.

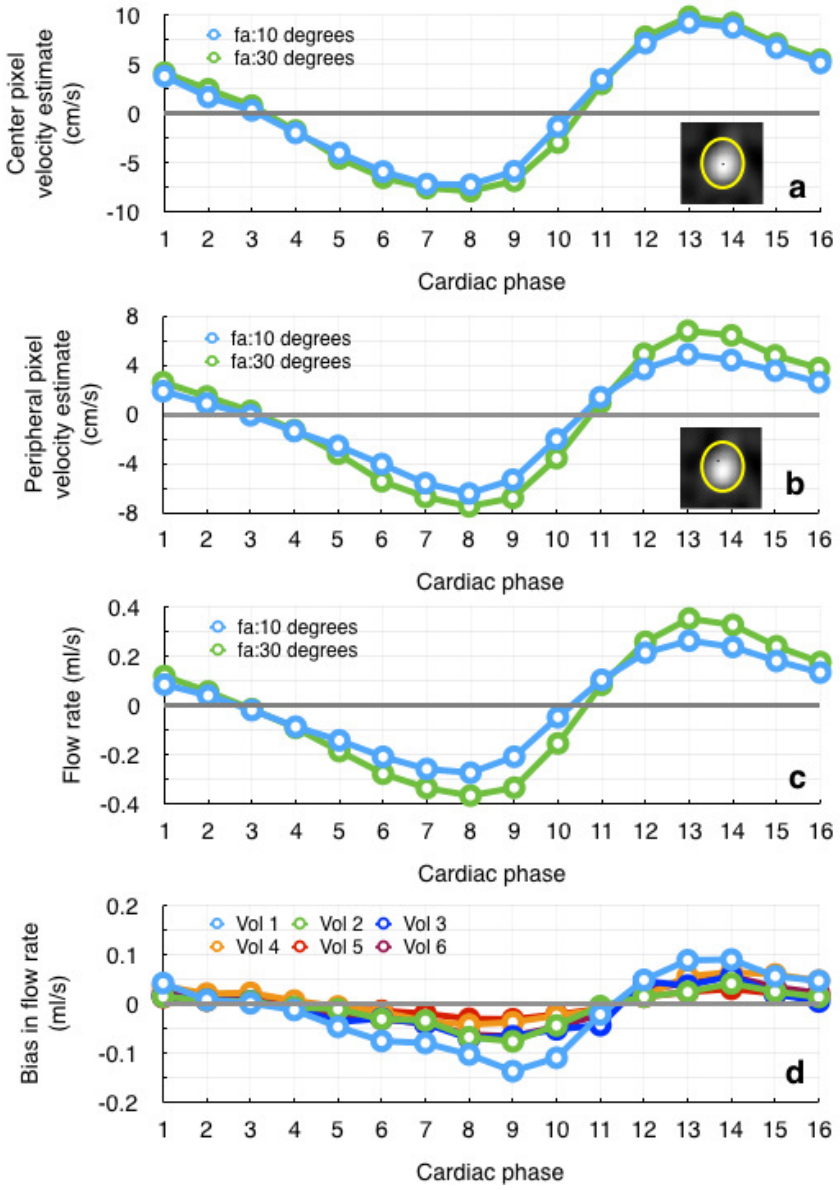

Figure 4.7: (a) Single center voxel (represented by the dark voxel within the yellow ROI) velocity estimate comparison for flip angles 10 and 30 degrees; (b) Single peripheral voxel (represented by the dark voxel within the yellow ROI) velocity estimate comparison for flip angles 10 and 30 degrees; (c) Flow rate estimate comparison for flip angles 10 and 30 degrees; (d) Bias in flow rate estimates were obtained by subtracting flip angle 10 flow rate estimates from flip angle 30 flow rate estimates. The data obtained were averaged over six experimental sets for each volunteer.

The temporal component influenced the spatiotemporal gradient to a greater extent during transition from systole to diastole and vice versa, as depicted in Fig. 4.6(b-d). The temporal profiles of aqueductal flow quantities were compared for $\theta = 10^o$, and $\theta = 30^o$, as illustrated in Fig. 4.7. With the higher flip angle, the velocities were overestimated, particularly during peak systole and diastole. The location of the velocity estimates at the aqueduct center and periphery were highlighted using an ROI (Fig. 4.7a & 4.7b). The bias in velocity estimates was observed to be higher at the aqueduct periphery when compared to the center of the aqueduct. The flow rate was calculated as a summation of the product of velocity estimate per voxel and the voxel area, over all the voxels within the yellow ROI. The temporal profile of the bias in flow rates demonstrated an overestimation by as high as 28% during systole, and as high as 19% during diastole by increasing θ from 10^o to 30^o. At peak systole and diastole there was good correlation between the spatial velocity gradient and bias, as depicted in Figs. 4.8(a-c), while the temporal variations in velocity did not seem to influence the bias, as shown in Figs. 4.8(d-f). During transition between systole and diastole however, the temporal velocity gradients had greater influence on the bias than the spatial velocity gradients, as shown in Figs. 4.8(g-i). The aqueductal stroke volumes for each experimental set acquired are shown in Fig. 4.9. The mean aqueductal stroke volume estimates separated by the volunteer is provided in Table 4.1. The Wilcoxon signed rank test determined that data obtained using $\theta = 30^o$ had significantly higher aqueductal stroke volume estimates than data obtained using $\theta = 10^o$ ($P < 0.05$).

4.4 Discussion

The focus of this work was to study the extent of RF saturation induced bias in CSF flow quantification, manifested by variation in MR acquisition parameters. Spins

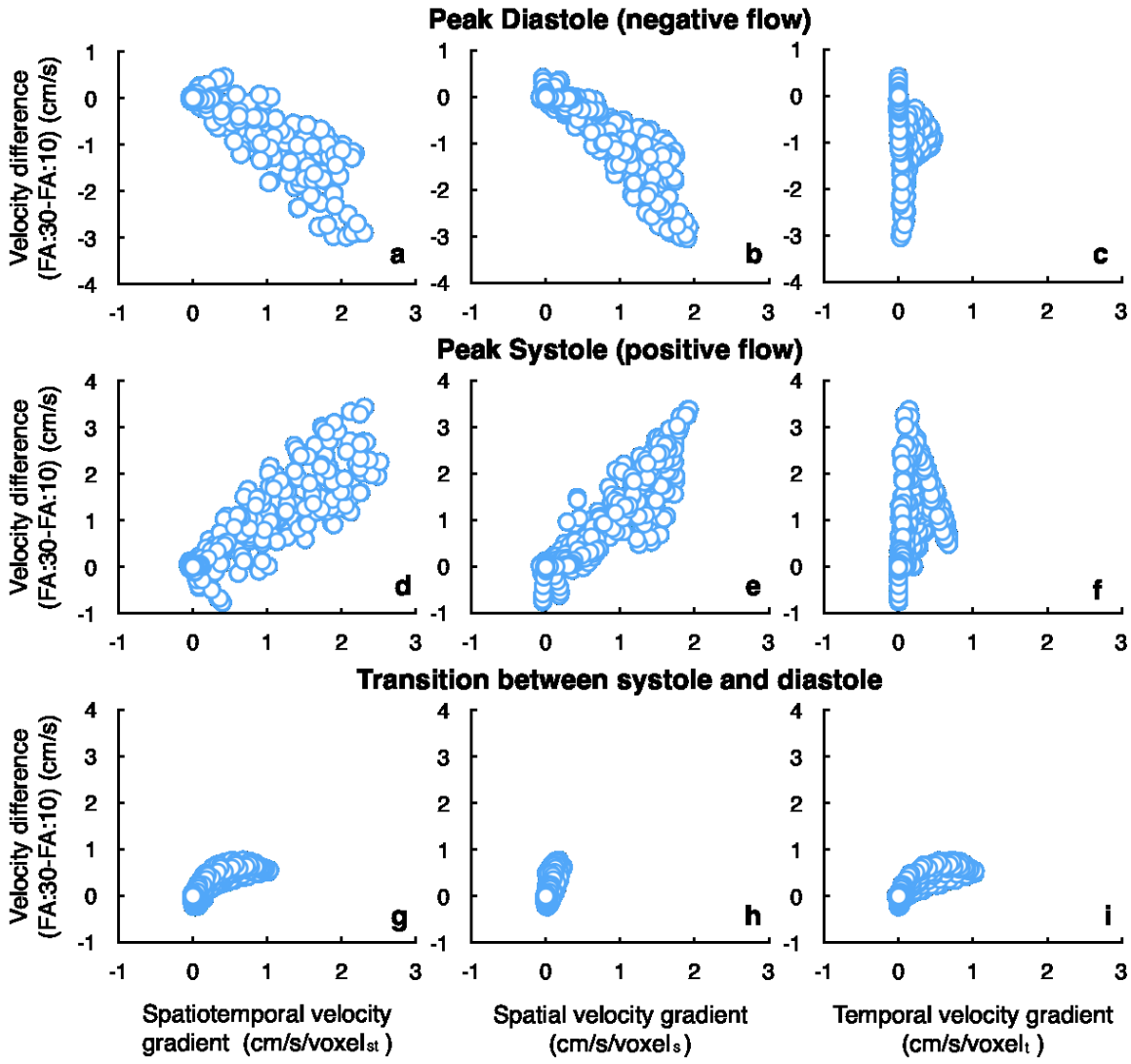

Figure 4.8: Correlation between bias measured as the velocity difference and (a, d, g) spatiotemporal velocity gradient, (b, e, h) spatial velocity gradient, (c, f, i) temporal velocity gradient for (a - c) peak diastole, (d - f) peak systole, and (g - i) transition from systole to diastole. The velocity gradient spans the spatial dimensions for (b, e, h), the temporal dimension for (c, f, i), and both spatial and temporal dimensions for (a, d, g).

with lower velocities in a given voxel will experience a larger number of successive RF excitations, and are therefore saturated to a greater extent than spins with higher

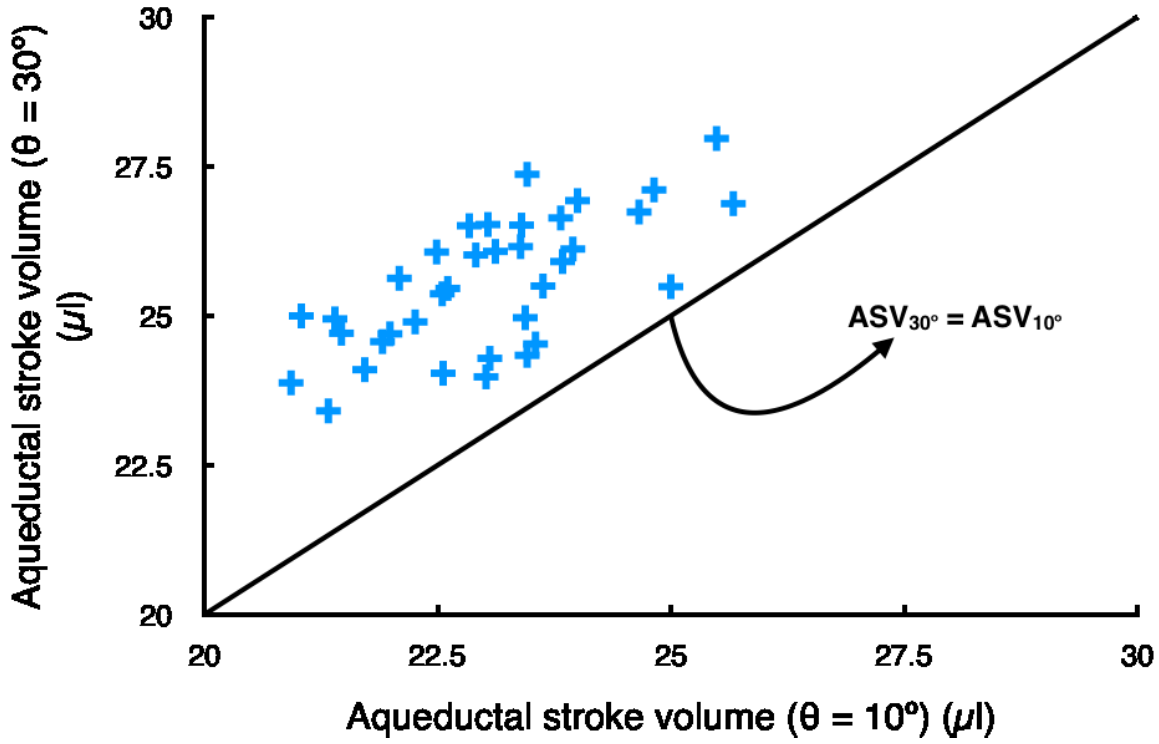

Figure 4.9: Comparison of the aqueductal stroke volume estimates for $\theta = 10^o$ and $\theta = 30^o$ for six volunteers, with six experimental set acquisitions per volunteer. The mean aqueductal stroke volumes were $23.05\mu l(\theta = 10^o)$ and $25.54\mu l(\theta = 30^o)$.

velocities. This effectively biases the mean velocity estimate of that voxel, and is more pronounced in voxels with a larger spin velocity distribution. This saturation effect is observed in 2D imaging, and can be mitigated by obtaining data using 3D volumetric scans. However, 2D cine PCMRI is still the clinical standard with respect to CSF flow quantification. Although CSF flow is complex, previous studies have shown that CSF flow through the aqueduct maintains a laminar profile [40]. Therefore, RF saturation effects are expected to bias flow at the aqueduct periphery to a greater extent than its center.

The manifestation of bias can occur due to variation in multiple acquisition parameters such as flip angle, slice thickness, and TR. The Theory section introduced

Table 4.1: Mean and standard deviation of aqueductal stroke volumes for $\theta = 10^o$ and $\theta = 30^o$

$Volunteer$	$ASV(mean \pm \sigma)\mu l$		
	θ_{10^o}	θ_{30^o}	$\theta_{30^o} - \theta_{10^o}$
1	22.33 ± 0.52	25.20 ± 0.73	2.87 ± 0.39
2	23.07 ± 2.05	25.74 ± 1.67	2.68 ± 0.93
3	24.23 ± 0.69	26.20 ± 1.14	1.97 ± 1.21
4	23.41 ± 0.50	25.15 ± 1.03	1.74 ± 0.66
5	23.36 ± 0.38	25.76 ± 1.09	2.40 ± 0.92
6	21.93 ± 0.78	25.18 ± 0.96	3.25 ± 0.56

the concept of critical velocity (V_0) as means of determining the combined effect of all three acquisition parameters. With increasing V_0, the likelihood of bias in measured velocity increases, as can be inferred from Fig.4.1b. These values of V_0 were computed from MR acquisition parameters obtained from five previously conducted studies on the use of PCMRI for CSF flow quantification in the aqueduct [2, 35, 76, 82, 88]. Based on the signal saturation effects from the data used to generate Fig.4.1, the experimental setup of using 10^o and 30^o for flip angles was chosen. The values of V_0 for our experimental set of $\theta = 10^o$, and 30^o, were calculated to be 0.38 cm/s and 3.6 cm/s respectively.

Table 4.2: Computation of critical velocities from relevant literature

Author$^{(ref)}$	Study Description	Spatial Resolution† (mm^2)	Cardiac Phases*	V0 (cm/s)
E Kapsalaki et al[39]	Quantification of normal CSF flow in aqueduct in cine PCMRI at 3T	N/A	N/A	0.8
M Ozturk et al[64]	Aqueduct CSF flow dynamics using PCMRI in normal pediatric cases	1.25 x 0.40	N/A	0.3
J H Lee et al[36]	CSF flow using PCMRI in aqueduct for normal volunteers	0.54 x 0.40	15	0.1
F Barkhof et al[6]	PCMRI of normal aqueductal CSF flow	1.00 x 1.00	9 - 17	5.0
O Unal et al[84]	cine PCMRI evaluation of normal aqueductal CSF flow according to age and sex	0.83 x 0.63	N/A	0.1
O Algin et al[2]	PCMRI in diagnosis of NPH and shunt response prediction	1.20 x 0.45	N/A	3.0
M Jaeger et al[35]	Relationship between ICP and PCMRI derived measures in NPH	0.55 x 0.55	N/A	0.5
P Luetmer et al[47]	Using PCMRI to diagnose NPH	0.63 x 0.84	16	0.8
M R Weinzierl et al[88]	Value of PCMRI to predict hydrocephalus	0.63 x 0.63	N/A	1.0
G Ringstad et al[76]	Comparing ASV using PCMRI with ICP scores for NPH patients	0.60 x 0.80	30 - 40	0.3
B Kahlon et al[38]	Is ASV using PCMRI a good predictor for shunt responds in NPH	N/A	N/A	N/A
G Chen et al[16]	Application of PCMRI in endoscopic aqueductoplasty of patients with hydrocephalus	1.10 x 1.45	N/A	N/A
C Beggs et al[7]	CSF flow in aqueduct in cerebrospinal venous insufficiency +ve and -ve patients using PCMRI	N/A	32	0.6
M Yousef et al[93]	Use of PCMRI based CSF flow rates to differentiate NPH from involutional brain changes	0.70 x 0.35	N/A	0.6
J F Giner et al[21]	PCMRI for identifying patients with NPH	0.33 x 0.33	25	0.5
A Scollato et al[78]	Changes in ASV for unshunted NPH using PCMRI	0.63 x 0.47	16	0.1
S M Stivaros et al[81]	ETV outcome with PCMRI	1.04 x 0.40	16	3.0
El Sankari et al[82]	PCMRI support for diagnosis of aqueductal stenosis	0.63 x 0.94	16	1.9
N S Kurwale et al[41]	PCMRI of intracranial shunt tube to diagnose VP shunt malfunction	N/A	N/A	N/A

N/A : Data Unavailable

$\dagger$: lower is better

$\star$: higher is better

Table 4.3: MR acquisition parameters for referenced literature in Table 4.2 (TA is defined as the rate of magnetization loss from the system due to RF pulses).

Reference	Flip angle (deg)	TR (ms)	Slice Thickness (mm)	TA (ms)
E Kapsalaki et al	20	30	4	482
M Ozturk et al	10	31	5.5	2041
J H Lee et al	10	45	4	2939
F Barkhof et al	45	52	7.5	150
O Unal et al	10	43	3	2809
O Algin et al	30	29	6	202
M Jaeger et al	15	34	5	981
P Luetmer et al	30	57	3	396
M R Weinziel	15	18	5	519
G Ringstad et al	10	24	4	1568
B Kahlon et al	N/A	44	N/A	N/A
G Chen et al	15	N/A	10	N/A
C Beggs et al	20	40	4	643
M Yousef et al	15	22	4	635
J F Giner et al	10	16	5	1045
A Scollato et al	10	54	5	3527
S M Stivaros et al	30	29	6	202
El Sankari et al	20	20	6	322
N S Kurwale et al	15	17	N/A	490

N/A : Data Unavailable

Data presented in Table 4.2 on the use of PCMRI to quantify CSF flow in clinical applications, highlight the ongoing discussion in the research community on the role of PCMRI as a clinical diagnostic tool for CSF based pathological conditions. Algin et al [2] found that PCMRI was unable to predict successful shunt response among NPH patients. The study by Luetmer et al [47] on the diagnostic utility of PCMRI among an NPH patient population had a negative outcome. On the other hand, Giner et al [21] was able to show a successful outcome in the role of PCMRI for identifying patients with NPH, and the work done by Kurwale et al [41] shows that PCMRI could be used to identify ventriculoperitoneal shunt malfunction. There have also been positive and negative study outcomes on the accuracy of aqueductal stroke volume estimates obtained using PCMRI in the prediction of shunt responsiveness among NPH patients [38, 76, 78]. Although dependance of quantitative CSF metrics on sex and age [6, 84], or combining CFD and PCMRI data to provide patient specific CSF quantification [40] have been studied, there has not been significant work on understanding bias in CSF flow estimates due to varying MR acquisition parameters. It is compelling to note that the value of V_0 was different in each of the afore mentioned studies. Based on the literature survey, there were four studies with $V_0 \geq 1.8$ cm/s, two of which had a V_0 of 3 cm/s, and one study had V_0 as high as 5 cm/s. In these studies, we expect the extent of bias contribution from saturation effects to be similar as that observed from the data presented in this work. In particular, the study by Barkhof et al [6] ($V_0 = 5$ cm/s) reported peak systolic and diastolic flow rates averaged among adults as 0.34 ml/s and 0.19 ml/s respectively. These values were comparable to the peak systolic (0.33 ml/s) and peak diastolic (0.20 ml/s) flow rates obtained for $\theta = 30^o$ ($V_0 = 3.6$ cm/s), from our experimental data (averaged over six volunteers) while the corresponding unbiased values ($\theta = 10^o$) were 0.26 ml/s and 0.15 ml/s respectively. This literature survey was not an exhaustive list of the

studies on CSF flow quantification using PCMRI, but rather intended to demonstrate the clinical relevance of understanding the bias due to saturation.

CSF flow in the aqueduct is approximately laminar [40] with almost equal flow in the caudal and cranial direction over the cardiac cycle. Bias in CSF flow estimates depends on the velocity spin distribution in each voxel within the flow ROI. The velocity estimate of each voxel is characterized by two spatial and one temporal dimensions (Fig. 4.6f). The largest spatial distribution of spin velocities is observed at the aqueduct periphery and the largest temporal distribution of spin velocities is observed at the center of the aqueduct. Spatial and temporal velocity gradients describe spin distribution dependent flow variations across the aqueduct cross-section, and over the cardiac cycle respectively. In the obtained volunteer data, bias in single voxel velocity and average flow rate estimates were predominantly influenced by the spatial velocity gradient during systolic and diastolic cardiac phases, with the temporal velocity gradient having a dominant influence during transition between systolic and diastolic cardiac phases (Fig. 4.8). The bias is not only dependent on V_0 but also on the spatial and temporal resolutions. Reducing the voxel size and increasing the number of acquired cardiac phases would help in mitigating the effects of RF saturation.

The bias in CSF flow estimates are an important source of error in studies utilizing 2D PCMRI as the sole diagnostic tool to determine clinical outcome. For example, Kurwale et al [41] reported on the utility of PCMRI based CSF velocity estimates in determining shunt malfunction. The study showed a significant change in peak and mean velocity (< 2 cm/s), between the control (shunt functioning) and test (shunt malfunction) groups. Bradley et al [13] discussed the role of PCMRI based aqueductal stroke volume quantification in NPH studies . In a previous study by the

same authors, NPH patients with aqueductal stroke volumes less than $42\mu l$ had a successful shunt response rate of 50%.

Limitations of this work include a simplified theoretical framework with focus on unidirectional steady flow. Incorporating the oscillatory flow profile is being considered as part of future work. Inaccuracies in flow quantification could also arise from background phase offsets, particularly for slow CSF flows as determined by Wentland et al [89]. To minimize the effect of eddy current based errors, the gradient strength and slew rates were limited to 31 mT/m and 120 mT/m/s respectively during data acquisition, followed by subtracting the phase of stationary tissue during post processing. Partial volume effects could also have a supplementary effect to RF saturation on flow bias. The contributions from partial volume and RF saturation were shown for varying flow partial fractions (Fig 4.1). This analysis was limited to a linear velocity distribution. While partial volume influenced velocity estimates only for the partially occupied flow voxels, RF saturation had an additional effect on fully occupied flow voxels with velocities less than V_0. This observation was also supported in vivo with the bias in aqueductal velocity estimates prevalent in multiple voxels interior of the aqueduct in addition to the peripheral voxels (Fig. 4.6).

In this work, the aqueductal stroke volume estimates for $\theta = 30^o$ were found to be greater than those for $\theta = 10^o$ for every single experimental set acquired (Fig4.9). RF saturation effects biased the aqueductal stroke volumes by 12%. Although a 12% bias may not significantly affect a shunt responsiveness study outcome involving NPH patients with high aqueductal stroke volumes, this bias is a substantial source of error in CSF flow quantification that should be taken into consideration in studies using PCMRI based CSF flow quantification to determine clinical outcomes.

4.5 Conclusion

The work presented here shows the extent of RF saturation induced bias in CSF flow estimates in the aqueduct, as a result of variation in MR acquisition parameters. The combined effect of RF saturation from MR acquisition parameters is described by V_0, spatial and temporal resolution. The bias depends on the velocity distribution of spins in a voxel, and was shown to be more prevalent at the aqueduct periphery, during the systolic and diastolic cardiac phases. The bias observed in CSF flow rates and aqueductal stroke volumes were significant, and should be taken into consideration when utilizing PCMRI based CSF flow estimates in studies involving clinical outcomes.

Chapter 5

A LABELING APPROACH FOR BULK CSF FLOW DETECTION IN VENTRICULAR SHUNTS

Cerebrospinal fluid (CSF) is a clear fluid generated primarily in the choroid plexus and is present in the ventricles, cranial and subarachnoid spaces. CSF is essential in maintaining the intracranial pressure, and in transport of essential nutrients in the brain. CSF production in healthy adults typically ranges from 400 - 600 ml per day [72]. Cerebrospinal fluid is produced at an average rate of 0.3 ml/min with approximately 100 ml of CSF present in the brain at any given time [14]. The CSF pathway is defined by its circulation and reabsorption functionalities. CSF is initially contained in the lateral ventricles, and passes through the foramen of Monro to the third ventricle, following which it reaches the fourth ventricle via the cerebral aqueduct. The cerebral aqueduct is an important anatomical region of interest due to its utility in testing MR based CSF flow imaging sequences. From the fourth ventricle, the CSF passes into the cisterna magna though the foramen of Luschka and Magendie. Thereafter the CSF pathway is split with one part directed into the cranial subarachnoid space, while the other into the spinal subarachnoid space. The CSF is reabsorbed into the venous system by the arachnoid granulation. This occurs as a result of a pressure gradient across the arachnoid granulations. The rate of CSF reabsorption is directly proportional to the intracranial pressure (ICP). CSF has complex flow dynamics, as observed by previous studies on CSF physiology [72, 77]. CSF flow can be described by two simultaneous components. The first is an oscillatory flow component that is primarily governed by cardiac pulsations. The

second is a much slower bulk flow component that as described above, is responsible for the transport of CSF and its reabsorption in the jugular venous system.

The quantification of CSF flow has been primarily achieved with the use of phase contrast magnetic resonance imaging (PCMRI) with cardiac synchronization to monitor temporal variations in CSF flow. This technique has been successful in quantifying the oscillatory component of CSF flow, but has not been shown to consistently and accurately quantify the bulk drainage of CSF, particularly through the aqueduct. There have been alternative approaches that utilize an approach similar to spin labeling to continuously monitor the flow of CSF [91]. Perturbations in the flow dynamics of CSF has been associated with pathological conditions such as normal pressure hydrocephalus (NPH), Chiari I malformations, and aqueductal stenosis.

Normal pressure hydrocephalus is a CSF based pathological condition that usually results in enlarged ventricles due to the accumulation of CSF, and could result in varying levels of intracranial pressure. Normal pressure hydrocephalus is often kept in check with the use of a surgically implanted shunt catheter. The shunt has a pressure valve that triggers the drainage of CSF through the shunt, and into the abdominal space, when there is excessive build up of intracranial pressure due to improper CSF drainage through its pathways. The shunt is a mechanical device and needs to be examined on a periodical basis for any signs of malfunction. In the United States, 40,000 or more shunt interventions are performed annually, majority of which can be attributed to patients with hydrocephalus [87]. In the same article, the authors attribute approximately 50% of all shunt failures to mechanical issues with the proximal catheter, while shunt malfunction due to infection can occur as early as 6 months post shunt placement, and account for less than 10% of all failures. While these sources can be categorized as device issues, expected CSF flow through the shunt could also be affected by physiological factors such as the presence of ventricular

loculations, and over drainage of CSF in the initial period soon after shunt placement could result in the formation of a subdural hematoma [87]. shunted hydrocephalus patients could also exhibit shunt malfunction symptoms if the shunt valve hasn't be set or programmed accurately. Phase contrast MRI is a commonly used technique used in flow quantification. While PCMRI has been shown to accurately quantify the oscillatory component of CSF flow, it is not sensitive enough to detect bulk CSF drainage. The flow in the shunt is expected to be slower than the bulk flow rates of CSF through its normal pathways. This, combined with the inability of PCMRI to accurately quantify bulk CSF flow, renders the technique unreliable. In addition, the accuracy of PCMRI is also dependent on correction of eddy current based phase errors, appropriate background phase suppression, and concomitant field compensation. Long scan times for high spatial and temporal resolution PCMRI scans has an impact on the feasibility of the technique as a quick check of shunt malfunction.

This work introduces an alternative approach to PCMRI to detect bulk CSF flow in the aqueduct and also in a ventricular shunt (for NPH patients). The proposed approach employs spatial labelling of CSF flow and monitors the labeled region over multiple dynamics. Section 5.1 provides a description of the pulse sequence for the proposed method. This is followed by the methods section (5.2) that describes the experimental setup for obtaining phantom and in vivo data. Two experimental scenarios with respect to the flow phantom are presented, with and without flow. The in vivo data acquisition is also divided into two stages. The first stage describes an experimental setup to evaluate the performance of the proposed method in healthy volunteers using the cerebral aqueduct as the flow region of interest. The second stage describes the experimental setup to evaluate the proposed method in a single shunt volunteer. Section 5.3 presents the data analysis techniques employed to evaluate the

method's performance. The results section (5.4) presents the images obtained and the outcome of data analysis, for each experimental setup. The chapter then concludes with a discussion section (5.5) highlighting the key aspects of the proposed method, and also presents scenarios when the method might not work as expected.

5.1 Pulse sequence description

The pulse sequence developed for this project is based on saturating the hyper-intense signal obtained from CSF from T2 weighted images. An adiabatic inversion prepared single shot T2 weighted turbo spin echo (TSE) sequence with variable "rest delay" is used. The rest delay is the time delay between the onset of the inversion pulse and the excitation pulse. The data acquisition is prospectively triggered with the cardiac cycle using a peripheral pulse-oximetry unit (PPU). The protocol is set up as a dynamic study with 2 or 3 dynamics. The rest delay is incremented by a value equal to the R-R interval for each dynamic obtained. The first dynamic has a delay that is much shorter when compared to the R-R interval. This delay is specified by a user defined parameter. The repetition time (TR) is set at 5 seconds to accommodate the recovery of CSF after each dynamic. The data acquisition is performed during the diastolic phase of the cardiac cycle. Spatial saturation of the CSF signal in the flow region of interest is achieved using the inversion pulse and a variable delay (rest delay). The rest delay increments for the subsequent dynamics of the study, is intended to force the data acquisition to skip one or more systolic events. A systolic event corresponds to CSF flow in the aqueduct from the third to the fourth ventricle. Skipping multiple systolic events, is therefore expected to cause the saturated signal across the CSF ROI, also referred to as the 'labeled flow', to be displaced in the direction of the CSF flow. A 3 dynamic study is adopted for easy visualization of the labeled flow displacement. The pulse sequence development follows multiple code

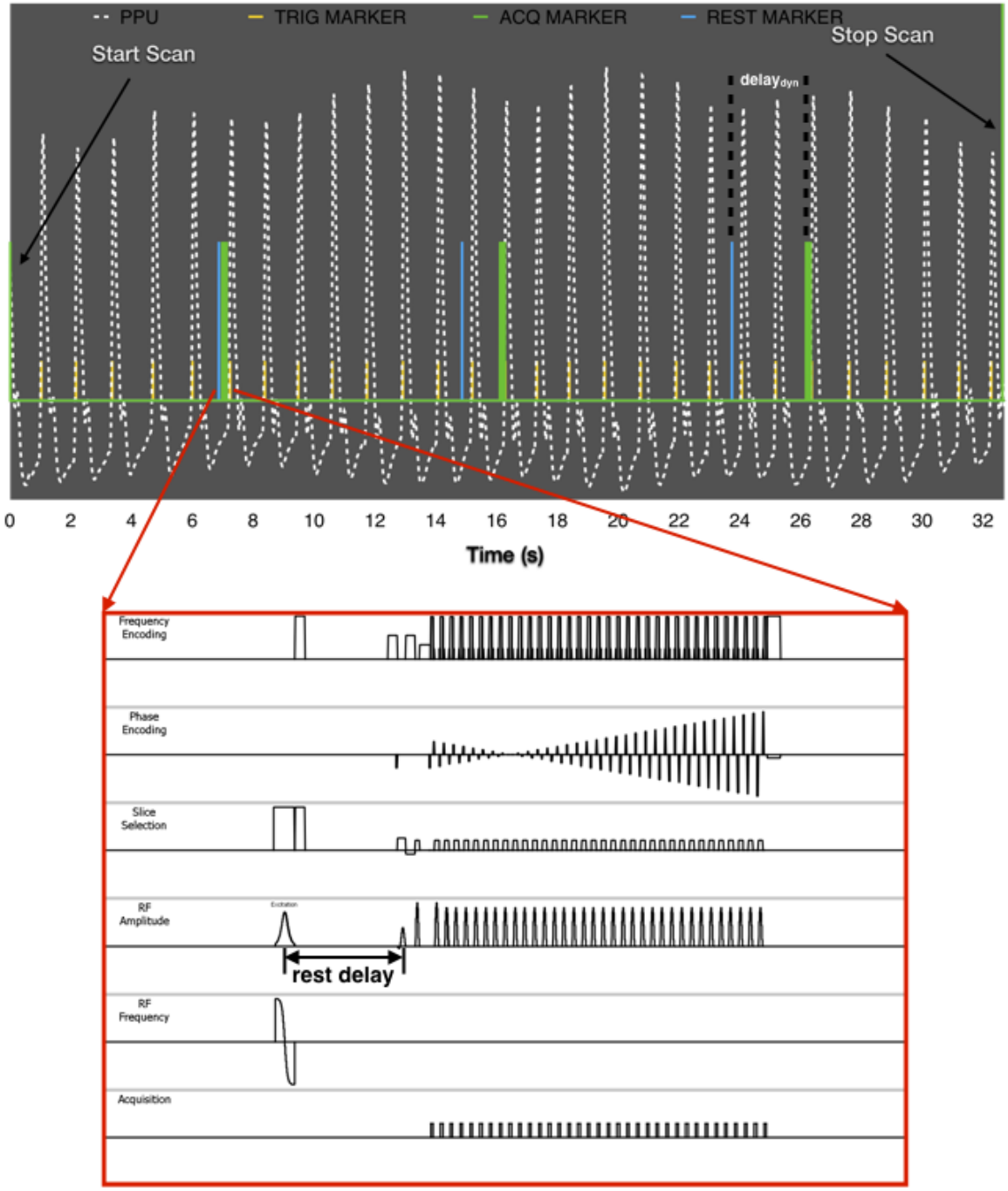

Figure 5.1: The proposed method represented as a timing diagram with markers denoting start and stop scan, saturation pulse onset, data acquisition, and the R peak trigger.

validation stages on a virtual machine environment before being ported to scanner as a patch. A figurative representation of the pulse sequence is shown in Fig. 5.1.

5.2 Methods

There were four stages of development for the proposed method described in detail in this section. 1) The first imaging experiment was implemented using a static phantom with a proximal shunt catheter immersed in a water bath. 2) An IV phantom with constant flow using a gravity feed setup was used to obtain data using the proposed method. 3) The proposed method was applied using the cerebral aqueduct of healthy volunteers as the anatomical region of interest. 4) The final stage involved obtaining data from shunt patients. In this particular case, the shunt data corresponds to a single adult volunteer.

5.2.1 Static Phantom

The static phantom comprised of a proximal ventricular shunt catheter, with outer diameter 2.5 mm and inner diameter 1.3 mm immersed partially in a water bath. The catheter was injected with water, multiple times to avoid the presence of air pockets within the catheter. The part of the catheter outside the water bath was sealed using a plastic stop cork.

A sagittal T1 weighted TFE sequence was used as a localizer to identify the shunt catheter orientation. The MR acquisition parameters for the localizer were: TE/TR = 4.1 / 8.9 ms; $\theta = 8^o$; SENSE = 2; FOV (XxYxZ) = 240x240x60 mm^3; In plane resolution = 0.9x0.9 mm^2; slice thickness = 0.9 mm; and scan time = 1 minute 54 seconds. The shunt flow protocol, was prescribed to capture the shunt catheter in plane using a prospectively triggered axial T2 weighted single shot TSE sequence with the following MR acquisition parameters: TE/TR = 80 ms / 5R-R; SENSE =

3; FOV (XxY) = 240x240 mm^2; In plane resolution = 0.55x0.75 mm^2; slice thickness = 3 mm; and scan time = 37 seconds.

A single experimental set consisted of the survey, a sagittal localizer and five repeated scans of the shunt flow protocol. The experimental set was repeated for multiple combinations of in-plane resolutions, ranging from 0.55 mm isotropic to 1.25 mm along the phase encoding direction, maintaining 0.55 mm resolution along the frequency encoding direction. The repeated scans were used in a noise sensitivity study.

5.2.2 Flow Phantom

A modified version of the static phantom was used for flow experiments due to the inability to extract fluid from the water bath through the proximal catheter tip. A gravity feed based flow phantom setup was designed to generate very slow flow rates, to mimic bulk CSF flow motion. The bulk flow component of CSF in a shunt is expected to be unidirectional, based on the functionality of the pressure valve. Hence an IV bag with water was used as the source, and the other end of the IV tubing was connected to an empty container (5 gallon capacity) serving as the sink. The imaging section comprised of a proximal shunt catheter inserted into the water bath with a U-bend such that both ends of the catheter were outside the bath. Images of the flow phantoms used in this work are presented in Appendix A. The IV tubing had a control valve to restrict the flow rates on the order of observed bulk flow of CSF.

Phantom data were obtained using flow in and out of a gravity feed phantom with flow velocities under 1 cm/s. The flow rate was maintained constant at 4.6 ml/h. The proposed method was setup as a 3 dynamic scan. A sagittal slice was obtained with the labeled region (thickness = 10 mm) orthogonal to the slice, and a rest delay of 10 ms. Physiological waveforms with cardiac frequency of 60 bpm were simulated for

trigger detection using the peripheral pulse-oximeter unit (PPU). The MR acquisition parameters for the localizer were: TE/TR = 4.1 / 8.9 ms; $\theta = 8^o$; SENSE = 2; FOV (XxYxZ) = 240x240x60 mm^3; In plane resolution = 0.9x0.9 mm^2; slice thickness = 0.9 mm; and scan time = 1 minute 54 seconds. The MR acquisition parameters for shunt protocol were: TE/TR = 80 ms / 5R-R; SENSE = 3; FOV (XxY) = 240x240 mm^2; In plane resolution = 0.55x0.75 mm^2; slice thickness = 3 mm; and scan time = 37 seconds.

A single experimental set consisted of the survey, a sagittal localizer and five repeated scans of the shunt flow protocol. Ten repeated trials of the experimental set were obtained. Data analysis was performed on each experimental set to ascertain if flow detection was possible from the monitoring of the saturation band across the flow region.

5.2.3 Healthy Volunteer

The cerebral aqueduct was identified as an appropriate flow region of interest among healthy volunteers without a shunt. The CSF dynamics here are sufficiently complex that if the proposed method was successful in the detection of bulk flow in the aqueduct, then the method should also be robust when attempting to detect flow within a shunt.

In vivo data was obtained using the cerebral aqueduct as the flow region of interest. A sagittal slice was prescribed along the midline of an axial TSE multi slice scout image to capture the aqueduct. The labelling slice was placed orthogonal to the aqueduct, between the third and fourth ventricle. The MR acquisition parameters for the localizer were: TE/TR = 163 / 4880 ms; SENSE = 2; FOV (XxYxZ) = 230x230x69 mm^3; In plane resolution = 0.47x0.58 mm^2; slice thickness = 3 mm. The MR acquisition parameters for shunt protocol were: TE/TR = 80 ms / 5R-R;

SENSE = 3; FOV (XxY) = 240x240 mm^2; In plane resolution = 0.55x0.75 mm^2; slice thickness = 3 mm; and scan time = 37 seconds.

A single experimental set consisted of the survey, a sagittal localizer and the shunt flow protocol. The total scan time for each volunteer was approximately 3 minutes. The experimental set was repeated for six healthy volunteers (aged between 25 and 45 years). Data analysis was performed on the combined data obtained from all volunteers to adjudicate if CSF bulk flow was detected by the proposed method.

5.2.4 Shunt Volunteer

The volunteer had a ventriculoperitoneal shunt embedded in the lateral ventricle of the brain and contained a non-programmable valve to adjust the CSF flow through the shunt.

In vivo data using the shunt as the flow region of interest was obtained on the Philips 3T Ingenia scanner. An oblique slice orientation was used to capture a majority of the shunt in-plane. The slice orientation of the shunt protocol was specified parallel to the shunt angulation with respect to the brain midline. The labeling slice was placed orthogonal to the shunt, proximal to the lateral ventricles. The MR acquisition parameters for the localizer were: TE/TR = 163 / 4880 ms; SENSE = 2; FOV (XxYxZ) = 230x230x69 mm^3; In plane resolution = 0.47x0.58 mm^2; slice thickness = 3 mm. The MR acquisition parameters for shunt protocol were: TE/TR = 80 ms / 5R-R; SENSE = 3; FOV (XxY) = 240x240 mm^2; In plane resolution = 0.55x0.75 mm^2; slice thickness = 3 mm; and scan time = 37 seconds.

A single experimental set consisted of the survey, an oblique angulated localizer and the shunt protocol with variations in slice thickness to ascertain optimal slice thickness values to avoid loss of CSF signal due to averaging effects from the shunt

lumen and surrounding static tissue. Data analysis was performed on the dataset obtained to determine if bulk CSF flow could be detected in the shunt.

5.3 Data Analysis

5.3.1 Displacement estimates

A nonzero displacement of the labeled flow in the direction of flow is a positive indication of bulk CSF in the region of interest. A center of mass based approach is utilized to obtain displacement estimates of the labeled flow. Center of mass based approaches have been previously used to correct for misregistration artifacts due to respiratory motion [28], and in translational motion correction for radial acquisitions [4].

The reconstructed real images are used for displacement estimation. The Fourier data are zero padded by a factor of 6.6 to provide sub-voxel displacement estimates. The images are scaled such that the labeled region appears hyper-intense while CSF flow appears hypo-intense in the grayscale image representation. A 1D line profile within the flow region of interest is identified for center of mass analysis to obtain the displacement estimates. Let the position of the j^{th} pixel on the 1D profile be $\{x_j\}$, and the corresponding pixel magnitude be $I(x_j)$. The first moment of the profile is

$$S_1(x) = \Sigma_j I(x_j) x_j. \tag{5.1}$$

The ratio of the first and zero order moments provides the center of mass. Changes in the center of mass are attributed to inter-dynamic displacement of the profile. The experimental setup in this comprises of three dynamics, resulting in three images describing the time evolution of the flow region of interest. Two displacement estimates were obtained form the center of mass difference: between dynamics 1 and 2 (D_{12}), and between dynamics 1 and 3 (D_{13}). In the case of shunt catheter flow phantom,

the flow is uniform and unidirectional. Therefore, a straight line fit was obtained using the model $y = mx$ whose slope provided an estimate of the flow velocity. The estimation of velocity was only valid for the phantom experiments.

A paired t-test was performed on the displacement estimates between successive dynamics using the repeated data acquisition of the proposed method without flow in the shunt catheter. This approach was implemented to determine the limits of variance in displacement estimates due to noise. Assuming that the sources of error would be consistent when there is flow in the shunt catheter, and in the in vivo data acquisitions, this variance in displacement estimates can be used in the other experiments to determine if the displacement estimates obtained are significantly larger than those due to noise.

5.3.2 Flow rate estimates

The average CSF bulk flow rate Q (ml/min), was estimated as

$$Q = \frac{D}{T_{delay}}.A \tag{5.2}$$

where D the average displacement of the labeled CSF (cm) measured over 3 dynamics, T_{delay} is equal to the average R-R interval (minutes) of the volunteer, and A is the aqueductal cross-section area (cm^2). The aqueduct cross-section was estimated using the magnitude image for each volunteer. In the case of flow phantom data, D represented the average displacement of labeled fluid (cm), and R-R interval was constant at 1 second. The inner diameter of the shunt catheter was used to calculate the flow cross-section area.

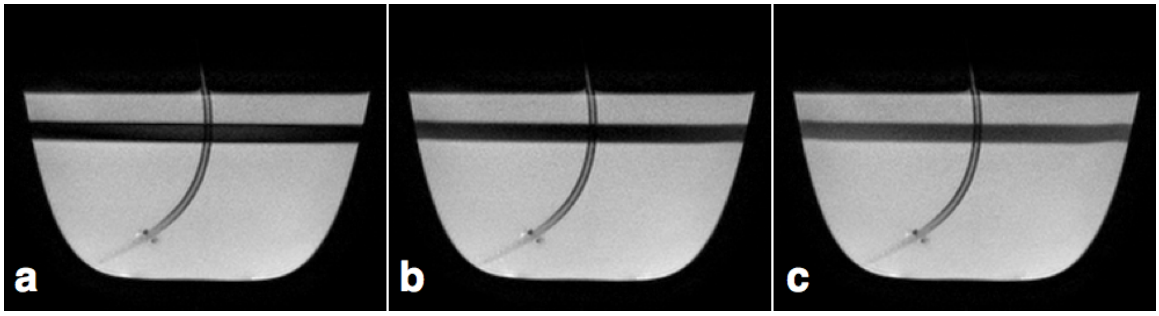

Figure 5.2: No flow condition simulated using a shunt catheter and in a water bath. The resolution was varied in the AP (vertical) direction from 0.55 mm to 1.25 mm.

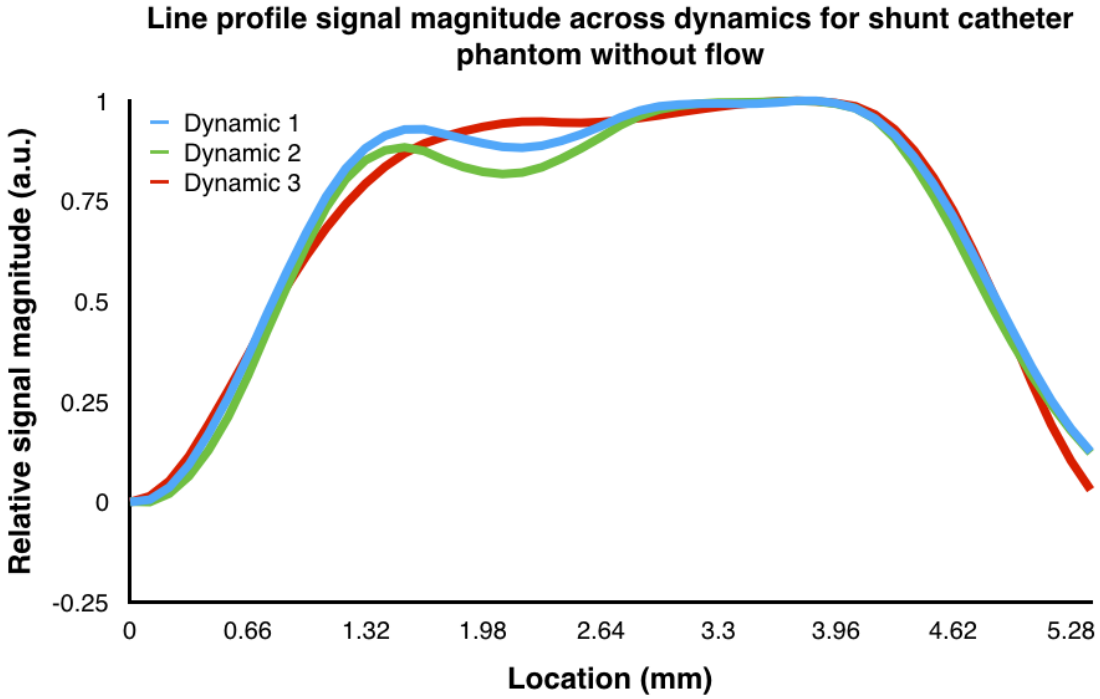

Figure 5.3: Signal profile for all three dynamics for a user selected line proximal to the center of the flow region in the shunt catheter phantom with no flow through the shunt

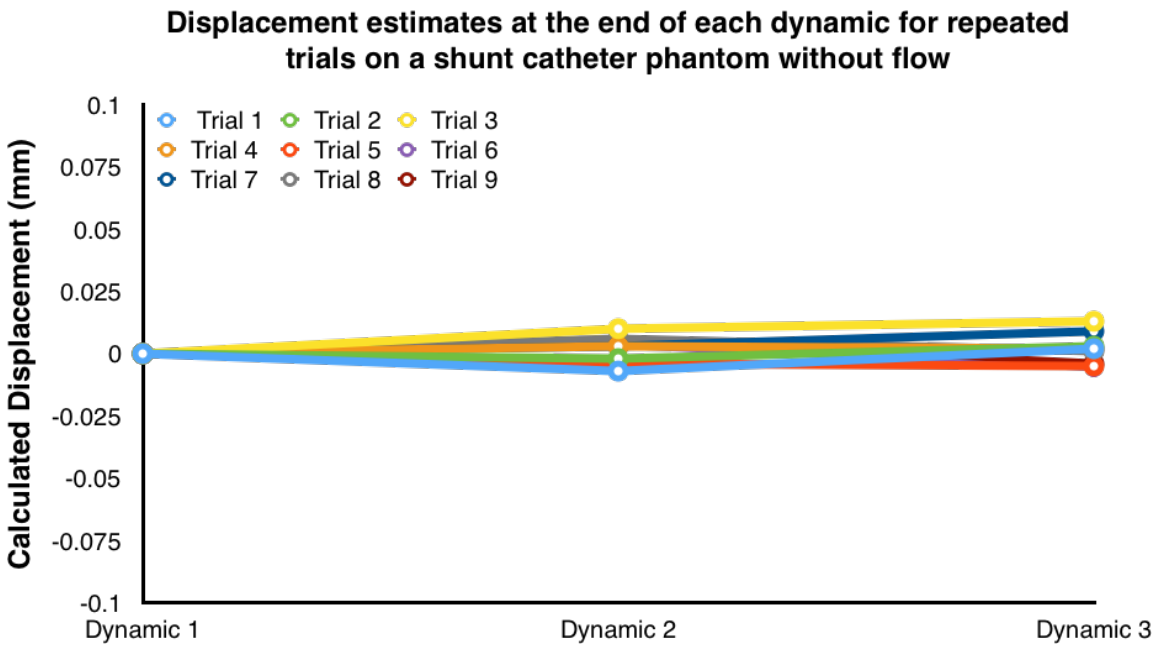

Figure 5.4: The displacement estimate of the labeled CSF region for dynamics 2 and 3 with respect to dynamic 1 obtained for repeated trials of the proposed approach on a shunt catheter phantom with no fluid flow in the catheter.

5.4 Results

5.4.1 Static Phantom

The images reconstructed from each dynamic are shown in Fig. 5.2. The degree of saturation in the labeled region was observed to diminish over the course of three dynamics due to T_1 recovery during the incremental delays between the onset of the inversion pulse, and data acquisition. The relative signal magnitude of the 1D profiles from each dynamic is shown in Fig. 5.3. The location specified along the X axis of Fig. 5.3 spans the length of the 1D profile. The signal magnitude curves did not appear to be shifted along the profile direction. This is expected since there is no flow in the shunt catheter. However, the signal profile can be affected by noise in the image or by signal recovery in the duration between application of the inversion

pulse and data acquisition. This would cause a reduction in the saturation extent of the labeled flow, particularly in the third dynamic. These factors could produce an apparent displacement, which may occur in the direction of flow or against it. The D_{12} and D_{13} estimates (mean ± std. dev) averaged over 9 repeated trials were 0.002±0.005 mm and 0.002±0.006 mm respectively and are shown in Fig. 5.4. The D_{12} and D_{13} estimates were found to not be statistically significant from zero mean displacement.

The 95% confident intervals of the displacement estimates with no flow in the shunt were established as [-0.0118 mm , 0.0118 mm] for D_{12}, and as [-0.0138 mm, 0.0138 mm] for D_{13}.

5.4.2 Flow Phantom

The images reconstructed from each dynamic are shown in Fig. 5.5 (a-c). The reconstructed magnitude and velocity maps from the phase contrast scan are shown in Fig. 5.5 (d-e). The red and green arrows indicate flow in opposite directions. The 1D profile for center of mass assessment was defined on the side of the labeled shunt catheter with the flow direction coming out of the phantom water bath (red arrow). The relative signal magnitude for the defined 1D profile is shown in Fig. 5.6. In comparison to the no flow scenario, initial observation of the relative signal magnitude across the three dynamics indicates a substantial shift in the direction of flow. Figure 5.7 shows the displacement estimates for each of the 10 trials performed. The average D_{12} estimate over 10 trials was 0.453 mm and the average D_{13} estimate was 0.895 mm. The average flow rate was estimated to be 4.81 ± 0.63 ml/hr. The difference between the average flow rate and the experimentally prescribed flow rate of 4.6 ml/hr was found to be not statistically significant.

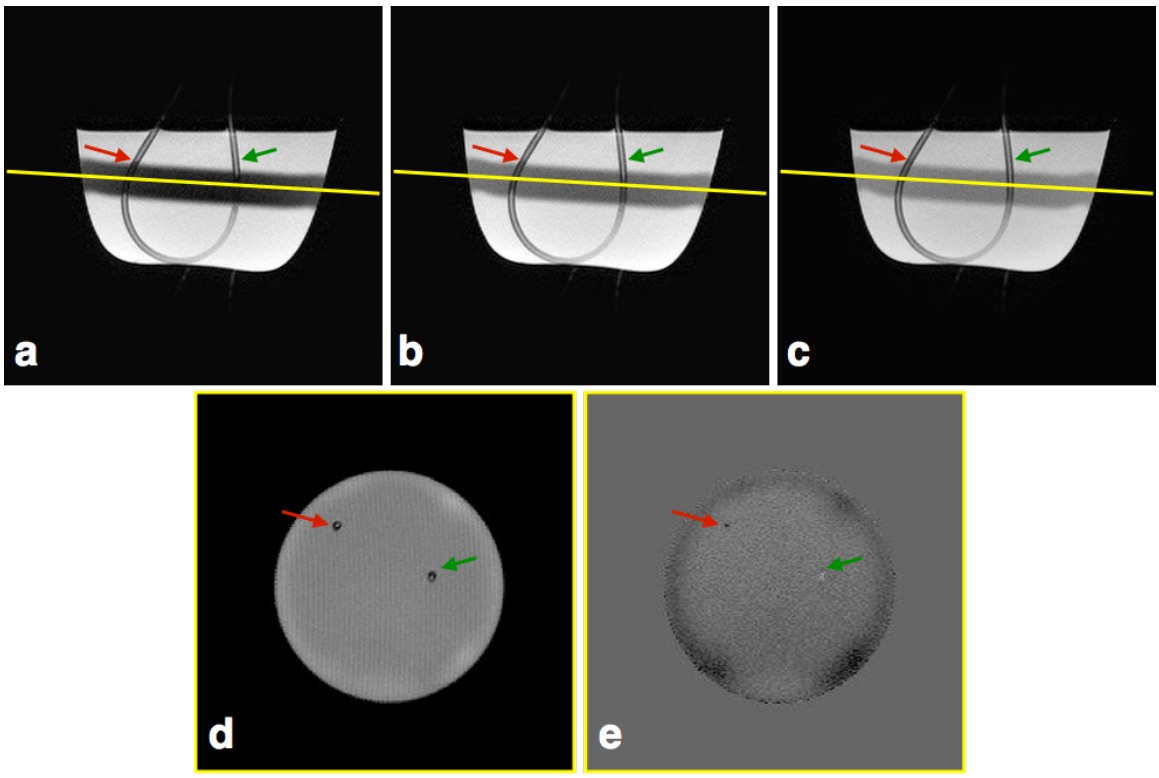

Figure 5.5: (a-c) Displacement of flow label in the direction of flow over the three dynamics of the proposed method. (e-f) Axial slice magnitude image and velocity map obtained for the same shunt catheter flow phantom. The red arrow points focusses on the displacement of labeled fluid in the direction of bulk flow, and the green arrow highlights the contrast generated by the inflow of fresh fluid into the labeled region.

The results of an independent two tailed t-test comparing the mean displacement estimates at the end of Dynamics 2 and 3 with respect to those obtained for the static phantom indicated a significant displacement of the labeled flow between Dynamic 1 and Dynamic 2, and between Dynamic 1 and Dynamic 3.

5.4.3 Healthy Volunteers

Figure 5.8 shows the images obtained from each of the 3 dynamics for a single healthy volunteer dataset. The region around the aqueduct with the labeled flow was

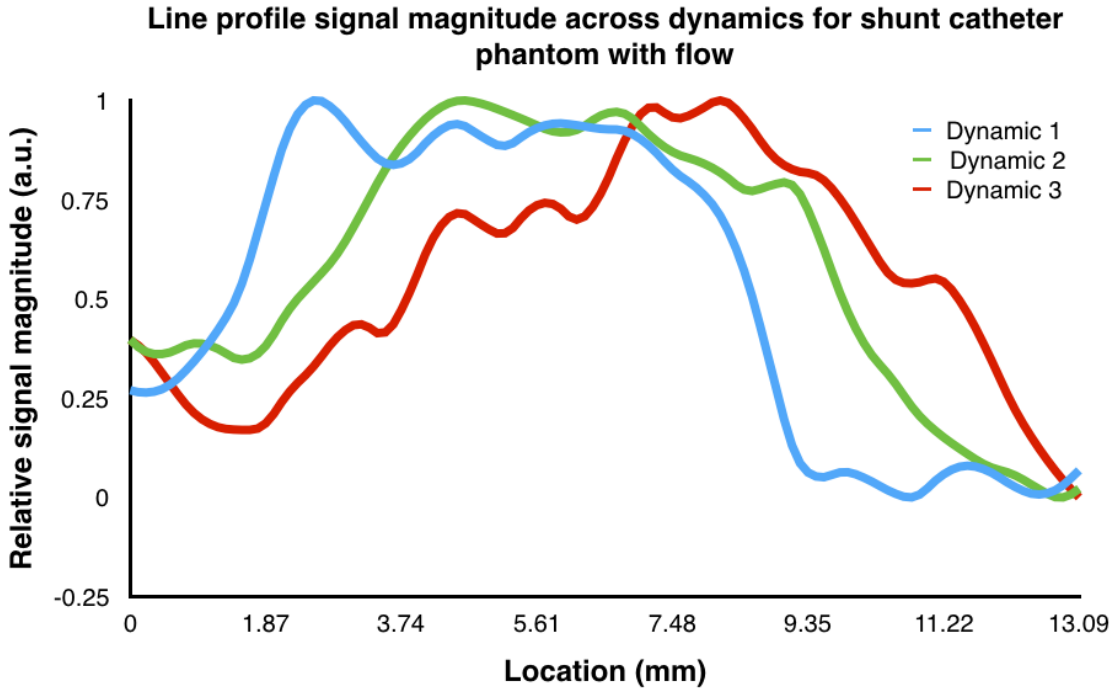

Figure 5.6: Signal profile for all three dynamics for a user selected line proximal to the center of the flow region of a U-shaped shunt catheter phantom with flow velocities approximated at 1.5 mm/sec through the shunt

magnified (green ROI). The circular ROI highlights the displacement of the labeled flow in the craniocaudal direction over the 3 dynamics. The signal profile is presented in Fig. 5.9. The signal profile provided a visual indication of substantial shift of the labeled flow in the craniocaudal direction. The reduction in signal saturation due to recovery effects was observed in regions located at the start of the 1D profile and regions located up to 2 mm along the length of the profile. The relative signal magnitude in Fig. 5.9, at these locations increased with each dynamic.

The displacement estimates obtained for each dataset acquired at Site1 and Site2 are illustrated in Fig. 5.10 and Fig. 5.11 respectively. Data at Site1 were acquired from adult healthy volunteers, while data at Site2 were acquired from an adult and

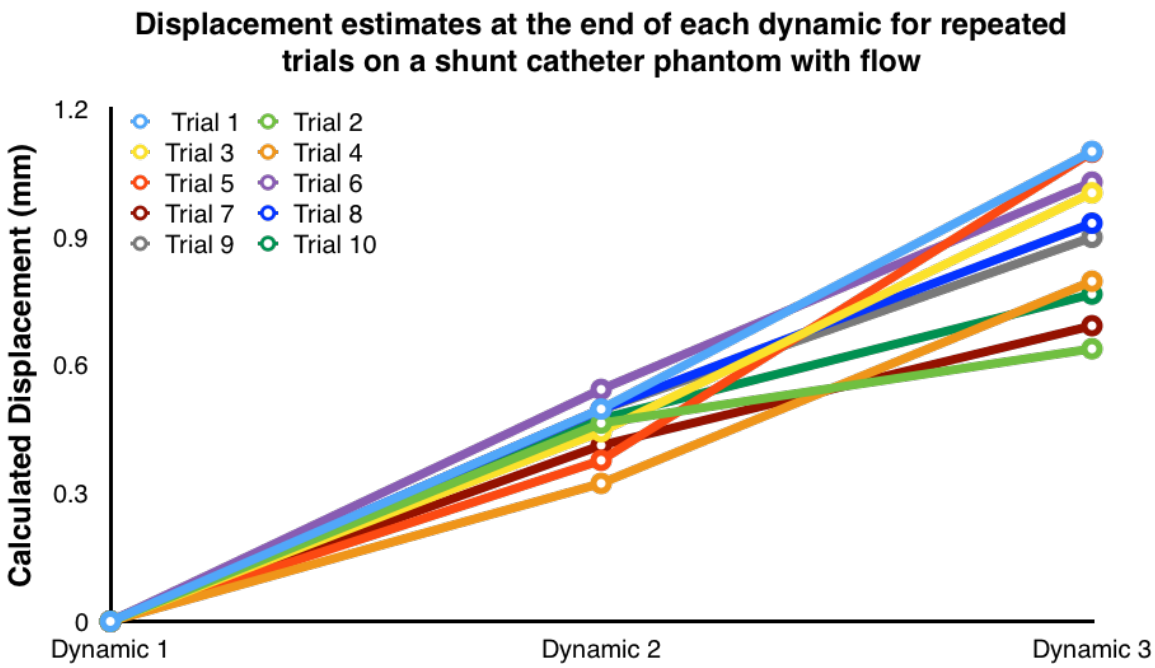

Figure 5.7: The displacement estimate of the labeled CSF region for dynamics 2 and 3 with respect to dynamic 1 obtained for repeated trials of the proposed approach on a shunt catheter phantom with unidirectional steady fluid flow in the catheter.

pediatric population. D_{12} estimates were observed to be approximately half of D_{13} estimates in the volunteer data except for Vol1 at Site1. The values of D_{12} and D_{13} averaged over all trials (Site1 and Site2 combined) were calculated to be 0.838 mm and 1.688 mm respectively, corresponding to an average flow rate of 0.33 ± 0.103 ml/min. This average flow was found to be comparable to normal CSF production rates of 0.3 ml/min.

The mean displacement estimates for D_{12} and D_{13} (over all data) were found to be significantly higher than the displacement estimates at 95% confidence level for the flow phantom with no flow through the shunt catheter.

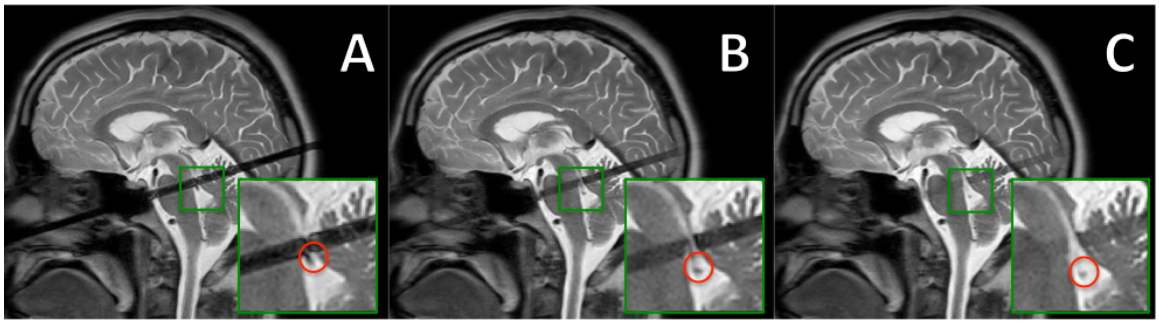

Figure 5.8: Dynamic study detecting CSF flow in aqueduct (Volunteer). (A), (B), and (C) show the images reconstructed from each dynamic [there is an incremental delay of 1 R-R for each dynamic]

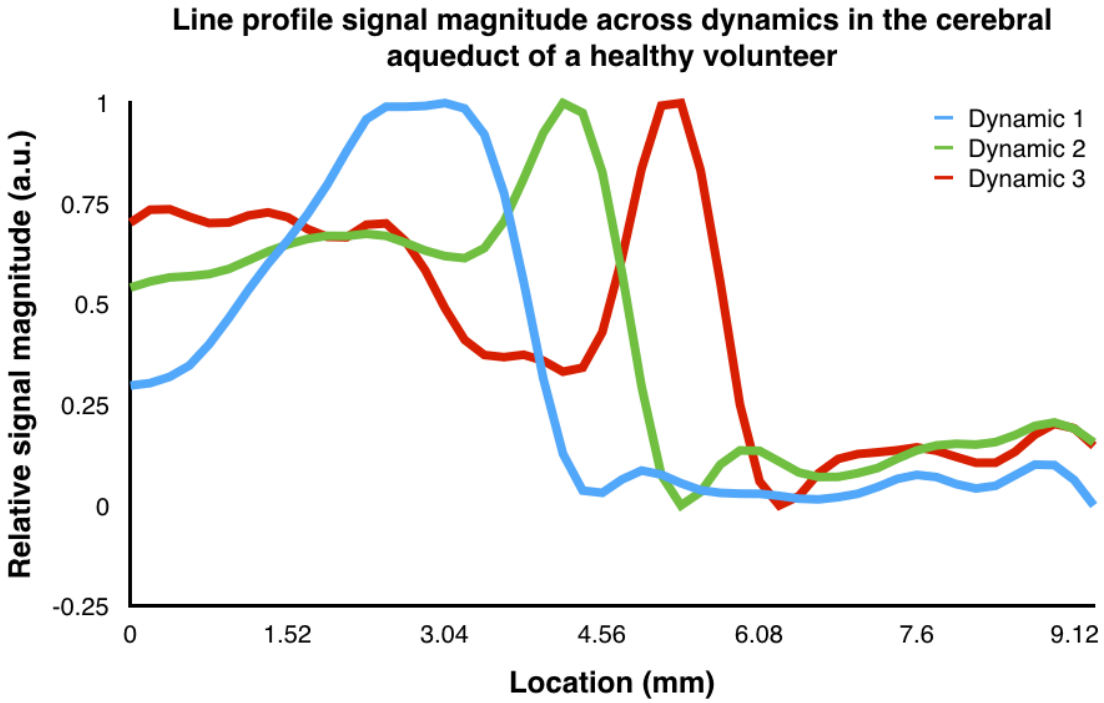

Figure 5.9: Signal profile for all three dynamics for a manually selected line proximal to the center of the aqueduct in a healthy adult volunteer

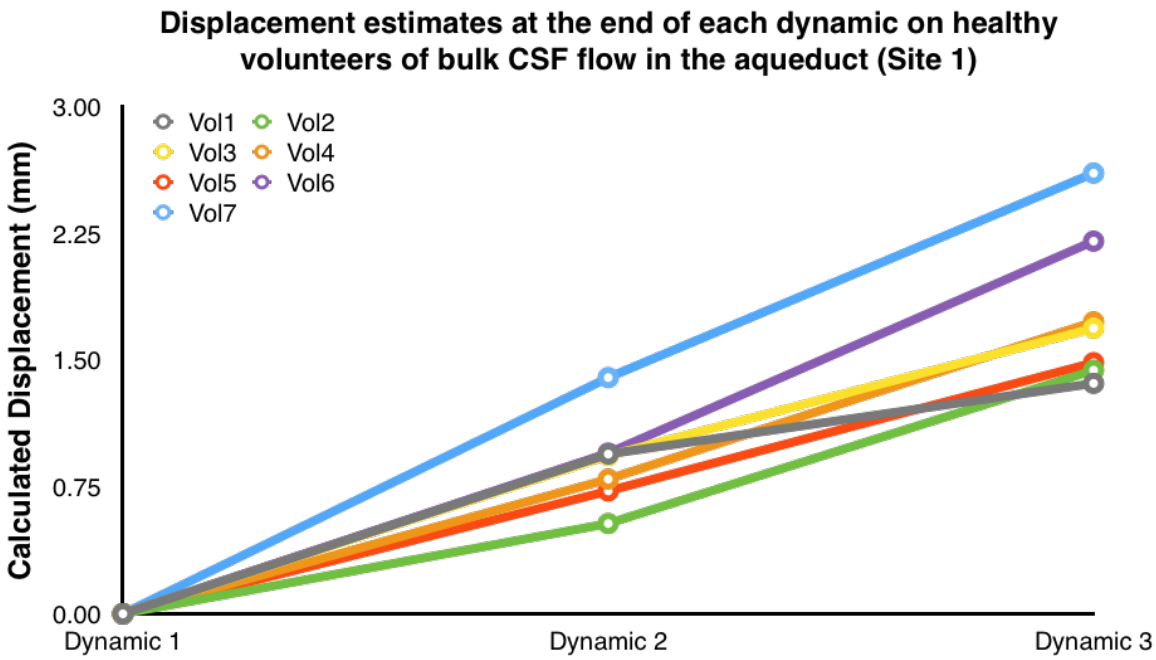

Figure 5.10: The displacement estimates for dynamics 2 and 3 with respect to dynamic 1 of the labeled CSF in the cerebral aqueduct using the proposed approach on multiple healthy volunteers at Site1.

5.4.4 Shunt Volunteer

The reconstructed magnitude images obtained using the proposed method on a shunt volunteer are shown in Fig. 5.12 (a-c). The square green ROI was magnified to highlight the embedded shunt. A visual inspection of the three dynamics does not provide a clear indication of the presence of flow through the shunt. The 1D signal profile at the center of the shunt, and spanning the labeled region is presented in Fig. 5.13. Visual inspection of the signal profile evolution over three dynamics indicated a small but definite shift of the center of mass in the direction away from the ventricular shunt source. A clear distinction of CSF inflow was observed into the labeled region across the three dynamics. There was a clear distinction in the outflow of the labeled CSF at the opposite end of the labeled region between the first two dynamics. The

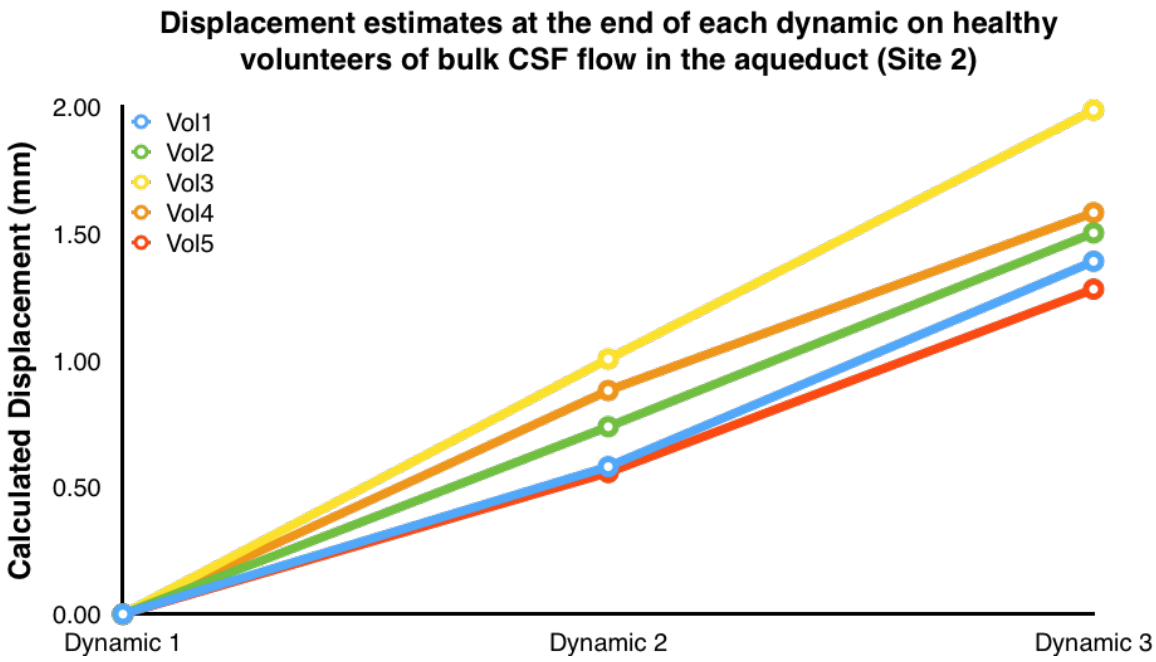

Figure 5.11: The displacement estimates for dynamics 2 and 3 with respect to dynamic 1 of the labeled CSF in the cerebral aqueduct using the proposed approach on multiple healthy volunteers at Site2.

signal profile curves for the second and third dynamic displayed distinctive outflow effect but not to the same extent as observed for CSF inflow.

Figure 5.12 and Fig. 5.13 are shown for the trial during which a Valsalva maneuver was performed by the volunteer. The displacement estimates for each trial performed are shown in Fig. 5.14. There was a substantial difference in the displacement estimates between the trial when the Valsalva maneuver was performed (Trial 3), and the remaining trials (without performing the Valsalva maneuver). The D_{12} estimate for Trial 3 was 0.12 mm and the D_{13} estimate was 0.21 mm. The D_{12} and D_{13} estimates were found to be higher than the upper limit of the 95% confidence interval with no flow in the phantom.

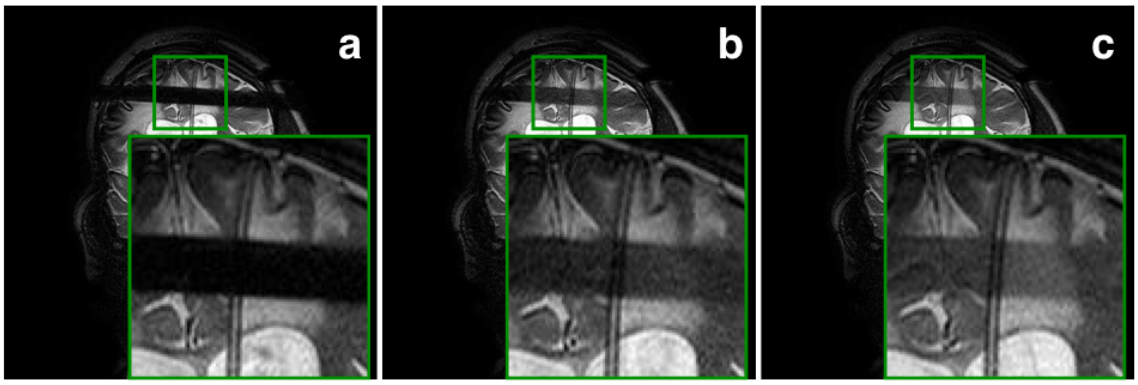

Figure 5.12: Dynamic study for detecting CSF bulk flow in a ventriculoperitoneal shunt. (A), (B), and (C) show the images reconstructed from each dynamic [there is an incremental delay of 1 R-R for each dynamic]

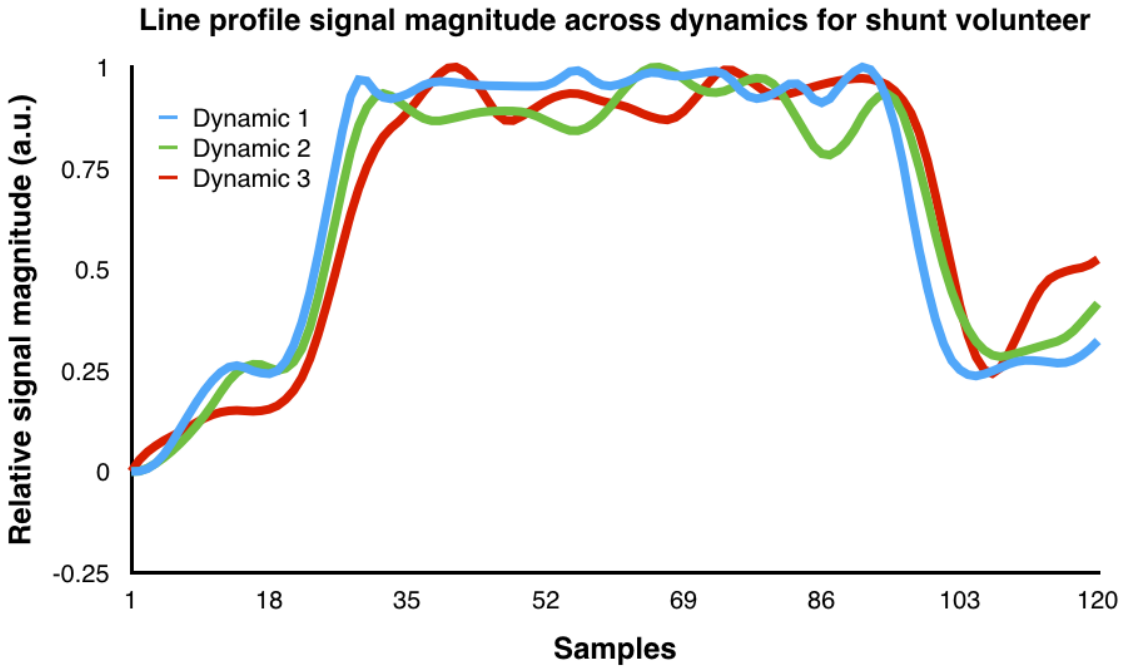

Figure 5.13: Signal profile for all three dynamics for a manually selected line proximal to the center of the shunt catheter for measurement in a volunteer with a ventriculoperitoneal shunt

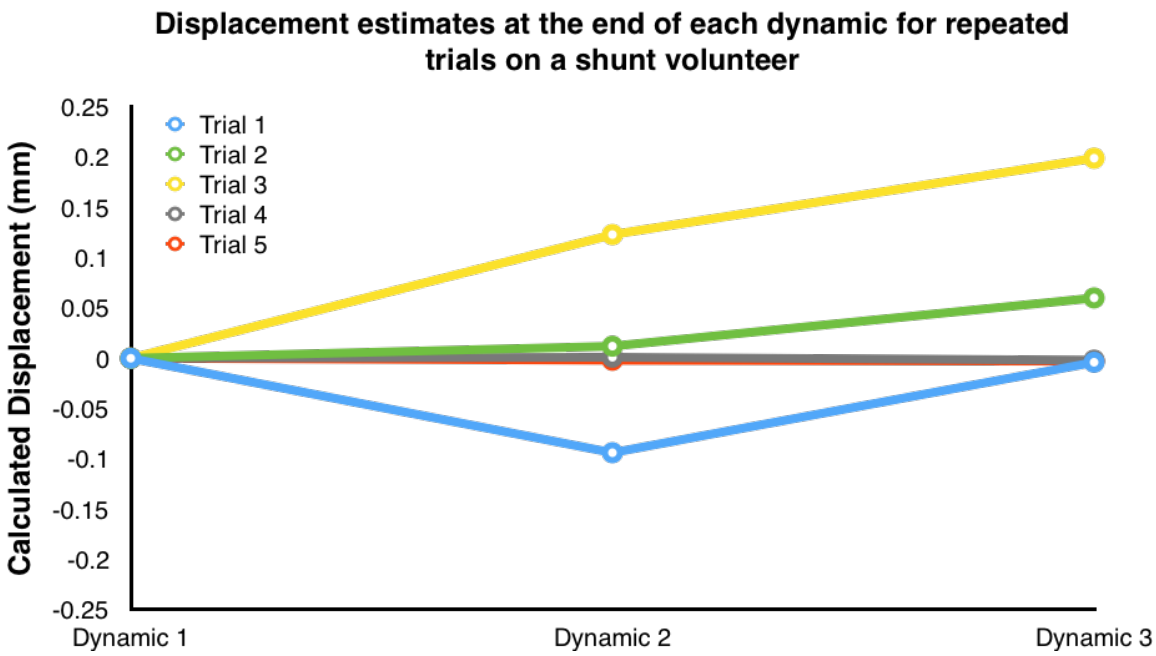

Figure 5.14: The displacement estimates for dynamics 2 and 3 with respect to dynamic 1 of the labeled CSF in the proximal catheter of the ventricular shunt in a single volunteer are shown over multiple trials using the proposed approach. The displacement estimates corresponding to Trial 3 were obtained while the volunteer performed a Valsalva maneuver.

5.5 Discussion

This work presented a labeling approach to detect bulk CSF flow in the aqueduct among healthy volunteers and demonstrated the potential utility towards bulk CSF flow detection in ventricular shunts. The discussion section on the proposed approach begins with detailing some of the existing methodologies to evaluate shunt malfunction. This is followed by highlighting the key aspects of the proposed approach, drawing comparisons to the existing methodology. The discussion section concludes with some insight into the sources of error that can affect the displacement estimate accuracy, and some of the limitations of this approach.

5.5.1 Existing Methodology

According to the Hydrocephalus Association, ventricular shunt malfunction is suspected to have occurred due to the appearance of symptoms such as headaches, vomiting, vision problems, loss of coordination or balance, and swelling along shunt tract, among others. The imaging modalities used to detect shunt malfunction are radiography, radionuclide imaging, CT and MRI [49, 87]. Radiographs are typically the cheapest option, and quick to use in an emergency room environment. Radiographs provide evaluation of the shunt integrity, and can identify breaks or disconnects in the shunt catheter. CT and MRI techniques have been extensively used to monitor ventricular size both pre and post shunt placement [25, 49, 87, 94]. MRI techniques used to image the ventricular size are primarily single shot spin echo based sequences. There have been multiple studies specific to pediatric imaging, using *Quick Brain MRI* which is based on single shot spin echo sequences [33, 94]. However, increase in intracranial pressure doesn't always result in enlarged ventricles as demonstrated in [90]. Therefore CT and current MRI protocols cannot always provide a confident evaluation of shunt patency.

In the event of inconclusive evaluation of shunt malfunction using imaging, invasive methods are used to determine if the shunt is functional. A common approach is the performance of a shunt tap to measure the intracranial pressure. This is performed in the distal catheter and its accuracy can be affected due to occlusion in the proximal catheter. Radionuclide imaging involves the injection of a radioactive material such as Technetium-99m ($^{99m}T_c$). The material is injected into the reservoir and propagates into the ventricles. The presence of the tracer is then detected at the ventricles and in the peritoneal space from imaging to determine if the shunt was successful in flushing out the tracer through the proximal and distal catheters. This is also currently the

most commonly used method to evaluate flow physiology in the shunt. However, it is an expensive method in conjunction with the injection of radioactive material albeit in small doses. It is also the only clinically used technique that provides dynamic information on CSF flow. This underlines the importance of developing an MRI based technique that can also provide dynamic information, while being noninvasive.

5.5.2 Proposed Approach

The proposed method uses a dynamic study to acquire 3 images depicting bulk CSF flow through the displacement of the labeled shunt ROI across the 3 dynamics. The protocol was based on a single shot TSE with SENSE (R=3), thus resulting in a short scan time of 37 seconds. The proposed method was developed with the motivation of ascertaining existence of CSF flow in a ventricular shunt to rule out shunt malfunction.

CSF appears bright on an image generated from T2 weighted spin echo sequences due to a long T2. The slice selective inversion pulse therefore, has a time dependent saturation effect on the CSF signal in the inverted slice. The contrast between the labeled CSF region and CSF signal from outside the inverted slice generates the basis for determining displacement of the labeled CSF in the direction of flow.

The phantom experiments were performed to evaluate the performance of the proposed approach for different flow rates. The static phantom experiments provided a platform to determine the extent of noise interference in obtaining displacement estimates of the labeled flow region over the three dynamics.

The cerebral aqueduct resembles a straight tube, and was therefore identified as an appropriate ROI for in vivo testing of the proposed approach. The complex flow dynamics of CSF in the aqueduct was also used as a basis to test the temporal robustness of the proposed approach for a wide range of cardiac frequencies (48 bpm

- 95 bpm). The proposed approach was sensitive to flow velocities an order of magnitude slower than those detectable by phase contrast in the flow phantom datasets. The phase contrast protocol was not part of the experimental setup for healthy volunteers and the shunt volunteer. The aqueduct data was obtained at two different sites, on MR scanners running two different versions of the MR software. Site 2 did not have the option of adaptive cardiac frequency update, and required additional pulse sequence programming. The cardiac interval was updated as the average of the 5 previous R-R interval values. The protocol run at site 1 was able to update the cardiac frequency from the physiology monitor data. The latency between the R peak detected by the plethysmograph and the true systolic event was approximated at 400 ms. Instructions were provided to healthy and shunt volunteers to minimize arm movement to minimize corruption of the physiological waveform data measured using the finger plethysmograph with noise.

A center of mass based approach was used to obtain displacement estimates because it was easy to implement yet accurate, and less sensitive to the dispersion effect of the labeled region across dynamics. The problem formulation was binary in nature: determining if there was flow in the shunt or not. Therefore, a one dimensional signal profile at the flow region center, and across the labeled region was adjudged sufficient to determine the presence or absence of flow. In the case of the flow phantom, the center of the shunt catheter provided the maximum displacement, and could be used to determine the maximum fluid velocity (assuming a laminar flow profile). Determining velocities becomes complicated in vivo due to the complex nature of CSF flow. Hypothetically, flow in the shunt is expected to be unidirectional, but there haven't been many studies determining the flow profile of CSF in the shunt. The images reconstructed for each dynamic were scaled independently to obtain a uniform

range of signal values in order to minimize the effect of contrast on the center of mass evaluation.

The displacement estimates obtained using the proposed approach for flow phantom and aqueduct measurements were found to be significantly higher than the 95% confidence interval of displacement due to noise alone. The average flow rates estimated from the displacement measurements were found to be comparable to the reference values for the flow phantom and in the aqueduct. The signal profile shown in Fig. 5.9 was obtained from *Vol3* (Site 2) who had the most consistent inter-dynamic cardiac frequency. The data acquisition occurred at the approximately the same time point in the R-R interval providing an accurate representation of bulk flow. This translated to consistent delays between the peak signal magnitude across two successive dynamics. *Vol1* data from site 1 on the other hand demonstrated varying displacement estimates across successive dynamics. This could be attributed to large fluctuations in the inter-dynamic cardiac frequency. The displacement estimates obtained from the shunt volunteer data did not provide sufficient visual evidence of flow in the shunt. This was confirmed with the displacement estimates obtained for trials 1, 2, 4 and 5. During trial 3, the volunteer was asked to perform the Valsalva maneuver, to ascertain if forced pressure would result in CSF flow through the shunt. The displacement estimates obtained corresponding to trial 3 indicated in the affirmative. There was also a strong indication that the CSF physiology in the shunt volunteer could have returned to normal due to the absence of shunt malfunction symptoms even with minimal to no flow in the shunt.

5.5.3 Assumptions and Study Limitations

The sensitivity of the labeled region displacement estimates to noise needs to be characterized. Displacement due to noise could be a potential source of error. The

variation in displacement estimates were characterized from the phantom data with no flow in the shunt catheter. Assuming comparable SNR in the phantom and in vivo, the noise deviation in displacement estimates provided the confidence interval to determine if the displacement estimates obtained with flow in shunt catheter and in vivo were affected by noise. While the physiology of CSF flow in the cerebral aqueduct is well characterized, there is still active discussion on the CSF flow physiology in a shunt catheter. The expectation is that CSF flow is unidirectional, flowing outward of the ventricles and into the abdominal space. The CSF flow is regulated by the pressure valve with the objective of maintaining acceptable levels of intracranial pressure. The current approach is based on the assumption of unidirectional flow and has not been evaluated for the potential existence of a regurgitant component of CSF flow in the shunt catheter. The flow phantom developed for evaluating the proposed approach is not designed with the appropriate entrance length of the catheter to support laminar flow profiles. Since flow profiles were not measured directly from the images obtained using the shunt catheter phantom, this design consideration was not expected to influence the accuracy of the obtained displacement estimates.

The primary limitation of the this study is the evaluation of the proposed approach on a single shunt volunteer. There was lack of a priori information available on the existence of flow in the shunt. Although visual confirmation of flow in the shunt was not obtained with confidence, the displacement estimates from the dataset corresponding to the Valsalva maneuver were indicative of flow in the shunt. It is also not clearly understood if a shunt patient lying in the supine position on the scanner bed will immediately have flow through the shunt. Alternatively, the quick brain MRI approach to evaluate shunt malfunction focusses on the ventricular size and not the flow physiology in the shunt, and hence cannot be used to provide additional information on CSF flow. Inter-dynamic motion also needs to be evaluated

in further detail as part of future work. The accuracy of the displacements can be affected by voluntary and involuntary motion occurring in between dynamics. The number of dynamics is currently limited to 3 due to the lack of contrast between CSF flow region that is and is not labeled. Further increase in the number of dynamics inhibits the ability to use the signal magnitude to obtain displacement estimates.

5.6 Conclusion

A labeling approach to detect CSF bulk flow in a ventricular shunt is proposed with the objective of identifying shunt malfunction in a quick and noninvasive manner. The proposed approach is a dynamic setup with incremental delay between the label application and data acquisition for successive dynamics. The displacement of the labeled CSF in the direction of flow was estimated using a center of mass approach. The proposed method was shown to be able to detect flow in a shunt catheter based flow phantom for different flow rates. This approach was also successful in detecting bulk CSF flow in the cerebral aqueduct of healthy volunteers, and was indicative of the presence of flow in a single volunteer's ventricular shunt. Future work would involve obtaining data from multiple shunt volunteers with a priori knowledge of flow in the shunt, to evaluate the performance of the proposed approach with statistical significance.

Chapter 6

DISCUSSION

The purpose of this work was to propose improvements to different aspects of MR flow imaging in the brain. Chapter 3 focussed on proposing improvements to the reconstruction pipeline for intracranial velocity maps obtained using multidirectional velocity encoding strategy, while Chapters 4 and 5 focussed on the two distinct CSF flow components.

A new approach to estimate noise statistics for a fully sampled spiral acquisition was presented in Chapter 3. Sampling density compensation weights were modified such that the region of K-space oversampled by a factor of two or more were split into odd and even data points with opposing polarity, masking out the remainder of K-space. Gridding reconstruction with the modified weights resulted in a scaled noise image with the same statistics as that of noise in a fully sampled dataset. The noise statistics were used in the development of a mask identifying background noise, static tissue and flow regions in an image volume. The implementation of the mask was shown for multidirectional velocity encoded PCMRI data. The tri-level mask was found to speed up the computational time of phase unwrapping of multidirectional velocity encoded data by a factor greater than 30x.

Multiple research studies have used MRI based CSF flow quantification in determining clinical outcome for conditions such as hydrocephalus. Chapter 4 of this work explored the extent of bias introduced in CSF flow estimates as a result of RF saturation effects. A new parameter called the critical velocity was proposed as an initial check for bias. The critical velocity was a threshold value to avoid RF saturation effects on measured velocities. The critical velocity is dependent on flip angle, TR,

and slice thickness. The CSF flow bias was also shown to highly correlate with the spatiotemporal velocity gradient. Aqueductal stroke volume estimates obtained from PCMRI data were found to be biased by as much as 12% for flip angle change from 10^o to 30^o.

Cerebrospinal fluid drainage is important to maintain appropriate levels of ICP. Ventricular shunts are used as surgical intervention when improper CSF drainage leads to elevated levels of ICP. However, evaluating shunt patency is still a major concern with the only MRI approach being a qualitative evaluation of ventricular size. Chapter 5 proposes a dynamic labeling approach to track CSF drainage through the ventricular shunt. The proposed approach uses incremental delays for successive dynamics between the preparation RF pulse (to label CSF) and the data acquisition to track displacement of the labeled CSF in the direction of drainage. A customized shunt catheter based flow phantom was designed for testing the proposed approach. The method was successfully evaluated in the aqueduct of healthy volunteers at two different research sites. The proposed approach was able to detect flow in the ventricular shunt of a 32 year old shunt volunteer performing a valsalva maneuver. Further work has to be performed in testing the approach in patients with shunts to show repeatability and reproducibility.

Chapter 7

FUTURE WORK

The noise estimation algorithm proposed in this work was performed on data acquired using spiral trajectory, but could be extended to any non-Cartesian trajectory or a Cartesian trajectory with oversampling in the readout direction. This would make the approach universally applicable to obtain accurate SNR, without the need to acquire multiple scans or a separate noise scan. The tri-level mask developed was applied towards speeding up phase unwrapping. Other potential applications for the mask would be estimating background phase errors by masking out noise and flow, and the use of the mask for flow visualization. Spurious noise voxels from edge of the field of view in the slice direction could affect flow visualization. Mask refinement techniques could be explored to mitigate the effect of the spurious voxels.

The effects of RF saturation were explored for CSF flow in the aqueduct. The aqueduct is a suitable flow ROI for the purposes of hydrocephalus applications. However, future work could also explore these effects for CSF flow in the cervical spine section, for example. The effects of partial volume when compared to RF saturation were presented with simulations run using the proposed theoretical framework. Delineating the effects of partial volume from RF saturation for phantom or in vivo data would help determine the severity of the bias for specific clinical applications.

The labeling approach to dynamically study CSF drainage was shown to successfully determine displacement estimates of the labeled flow over multiple dynamics for a phantom setup and in the aqueduct of healthy volunteers. Obtaining in vivo shunt data would enable testing of the labeling approach in identifying flow or no flow in a ventricular shunt.

REFERENCES

[1] Aja-Fernández, S., A. Tristán-Vega and C. Alberola-López, "Noise estimation in single- and multiple-coil magnetic resonance data based on statistical models", Magnetic Resonance Imaging **27**, 10, 1397–1409, URL `http://dx.doi.org/10.1016/j.mri.2009.05.025http://linkinghub.elsevier.com/retrieve/pii/S0730725X09001404` (2009).

[2] Algin, O., B. Hakyemez and M. Parlak, "The Efficiency of PC-MRI in Diagnosis of Normal Pressure Hydrocephalus and Prediction of Shunt Response", Academic Radiology **17**, 2, 181–187 (2015).

[3] Alvarez, L. W. and F. Bloch, "A Quantitative Determination of the Neutron Moment in Absolute Nuclear Magnetons", Physical Review **57**, 2, 111–122, URL `https://link.aps.org/doi/10.1103/PhysRev.57.111` (1940).

[4] Anderson, A. G., J. Velikina, W. Block, O. Wieben and A. Samsonov, "Adaptive retrospective correction of motion artifacts in cranial MRI with multicoil three-dimensional radial acquisitions", Magnetic Resonance in Medicine **69**, 4, 1094–1103 (2013).

[5] Axel, L., "Blood flow effects in magnetic resonance imaging", AJR Am J Roentgenol **143** (1984).

[6] Barkhof, F., M. Kouwenhoven, P. Scheltens, M. Sprenger, P. Algra and J. Valk, "Phase-contrast cine MR imaging of normal aqueductal CSF flow. Effect of aging and relation to CSF void on modulus MR.", Acta radiologica **35**, 2, 123–130 (1994).

[7] Beggs, C. B., C. Magnano, S. J. Shepherd, K. Marr, V. Valnarov, D. Hojnacki, N. Bergsland, P. Belov, S. Grisafi, M. G. Dwyer, E. Carl, B. Weinstock-Guttman and R. Zivadinov, "Aqueductal cerebrospinal fluid pulsatility in healthy individuals is affected by impaired cerebral venous outflow", Journal of Magnetic Resonance Imaging **40**, 5, 1215–1222 (2014).

[8] Bernstein, M. A., M. Grgic, T. J. Brosnan and N. J. Pelc, "Reconstructions of phase contrast, phased array multicoil data", Magn Reson Med **32** (1994).

[9] Bernstein, M. A., K. F. King and X. J. Zhou, *Handbook of MRI Pulse Sequences* (Elsevier Inc., ????).

[10] Bernstein, M. A., X. J. Zhou, J. A. Polzin, K. F. King, A. Ganin, N. J. Pelc and G. H. Glover, "Concomitant gradient terms in phase contrast MR: Analysis and correction", Magnetic Resonance in Medicine **39**, 2, 300–308 (1998).

[11] Bock, J., A. Frydrychowicz, A. F. Stalder, T. A. Bley, H. Burkhardt and J. Hennig, "4D phase contrast MRI at 3 T: effect of standard and blood-pool contrast agents on SNR, PC-MRA, and blood flow visualization", Magn Reson Med **63** (2010).

[12] Bock, J., B. W. Kreher, J. Hennig and M. Markl, "Optimized pre-processing of time-resolved 2D and 3D Phase Contrast MRI data", in "Proc. Intl. Soc. Mag. Reson. Med", vol. 15, p. 3138 (2007).

[13] Bradley, W. G., "Magnetic Resonance Imaging of Normal Pressure Hydrocephalus", Seminars in Ultrasound, CT and MRI **37**, 2, 120–128 (2016).

[14] Brinker, T., E. Stopa, J. Morrison and P. Klinge, "A new look at cerebrospinal fluid circulation", Fluids and Barriers of the CNS **11**, 1, 1–16 (2014).

[15] Bryant, D. J., J. A. Payne, D. N. Firmin and D. B. Longmore, "Measurement of flow with NMR imaging using a gradient pulse and phase difference technique", J Comput Assist Tomogr **8** (1984).

[16] Chen, G., J. Zheng, Q. Xiao and Y. Liu, "Application of phase-contrast cine magnetic resonance imaging in endoscopic aqueductoplasty", Experimental and Therapeutic Medicine **5**, 6, 1643–1648 (2013).

[17] Chernobelsky, A., O. Shubayev, C. R. Comeau and S. D. Wolff, "Baseline correction of phase contrast images improves quantification of blood flow in the great vessels", J Cardiovasc Magn Reson **9** (2007).

[18] Constantinides, C. D., E. Atalar and E. R. McVeigh, "Signal-to-noise measurements in magnitude images from NMR phased arrays", Magnetic Resonance in Medicine **38**, 5, 852–857 (1997).

[19] Dumoulin, C. L., S. P. Souza, M. F. Walker and W. Wagle, "Three-dimensional phase contrast angiography", Magn Reson Med **9** (1989).

[20] Ernst, R. R. and W. A. Anderson, "Application of Fourier Transform Spectroscopy to Magnetic Resonance", Review of Scientific Instruments **37**, 1, 93–102, URL `http://aip.scitation.org/doi/10.1063/1.1719961` (1966).

[21] Forner Giner, J., R. Sanz-Requena, N. Flórez, A. Alberich-Bayarri, G. García-Martí, A. Ponz and L. Martí-Bonmatí, "Quantitative phase-contrast MRI study of cerebrospinal fluid flow: a method for identifying patients with normal-pressure hydrocephalus", Neurología (English Edition) **29**, 2, 68–75 (2014).

[22] Gatehouse, P. D., M. P. Rolf, K. M. Bloch, M. J. Graves, P. J. Kilner, D. N. Firmin and M. B. Hofman, "A multi-center inter-manufacturer study of the temporal stability of phase-contrast velocity mapping background offset errors", Journal of Cardiovascular Magnetic Resonance **14**, 1, 1, URL `http://dx.doi.org/10.1186/1532-429X-14-72` (2012).

[23] Gatehouse, P. D., M. P. Rolf, M. J. Graves, M. B. Hofman, J. Totman and B. Werner, "Flow measurement by cardiovascular magnetic resonance: a multi-centre multi-vendor study of background phase offset errors that can compromise the accuracy of derived regurgitant or shunt flow measurements", J Cardiovasc Magn Reson **12** (2010).

[24] Giese, D., M. Haeberlin, C. Barmet, K. P. Pruessmann, T. Schaeffter and S. Kozerke, "Analysis and correction of background velocity offsets in phase-contrast flow measurements using magnetic field monitoring", Magn Reson Med **67** (2012).

[25] Goeser, C. D., M. S. McLeary and L. W. Young, "Diagnostic imaging of ventriculoperitoneal shunt malfunctions and complications.", RadioGraphics **18**, 3, 635–651, URL papers3://publication/uuid/A45FCE71-0988-4581-BA66-3CBF4DD0FCD7http://pubs.rsna.org/doi/10.1148/radiographics.18.3.9599388 (1998).

[26] Griswold, M. A., P. M. Jakob, R. M. Heidemann, M. Nittka, V. Jellus, J. Wang, B. Kiefer and A. Haase, "Generalized Autocalibrating Partially Parallel Acquisitions (GRAPPA)", Magnetic Resonance in Medicine **47**, 6, 1202–1210 (2002).

[27] Gudbjartsson, H. and S. Patz, "The rician distribution of noisy mri data", Magnetic Resonance in Medicine **34**, 6, 910–914, URL http://doi.wiley.com/10.1002/mrm.1910340618 (1995).

[28] Gupta, S. N., M. Solaiyappan, G. M. Beache, A. E. Arai and T. K. Foo, "Fast method for correcting image misregistration due to organ motion in time-series MRI data", Magnetic Resonance in Medicine **49**, 3, 506–514, URL http://doi.wiley.com/10.1002/mrm.10394 (2003).

[29] Haacke, M. E., R. W. Brown, M. R. Thompson and R. Venkatesan, *Magnetic Resonance Imaging* (John Wiley & Sons Ltd, Chichester, UK, 2014), URL http://doi.wiley.com/10.1002/9781118633953.

[30] Hahn, E. L., "Spin Echoes", Physical Review **80**, 4, 580–594, URL https://link.aps.org/doi/10.1103/PhysRev.80.580 (1950).

[31] Hennig, J., A. Nauerth and H. Friedburg, "RARE imaging: a fast imaging method for clinical MR.", Magnetic Resonance Imaging **3**, 6, 823–833 (1986).

[32] Holland, B. J., B. F. Printz and W. W. Lai, "Baseline correction of phase-contrast images in congenital cardiovascular magnetic resonance", J Cardiovasc Magn Reson **12** (2010).

[33] Iskandar, B. J., J. M. Sansone, J. Medow and H. A. Rowley, "The use of quick-brain magnetic resonance imaging in the evaluation of shunt-treated hydrocephalus", Journal of Neurosurgery: Pediatrics **101**, 2, 147 – 151, URL http://thejns.org/doi/abs/10.3171/ped.2004.101.2.0147 (2004).

[34] J, S., P. DHJ, D. AJ and P. W, "Automatic estimation of the noise variance from the histogram of a magnetic resonance image", Physics in Medicine and Biology **52**, 5, 1335–1348 (2007).

[35] Jaeger, M., A. K. Khoo, D. A. Conforti and R. Cuganesan, "Relationship between intracranial pressure and phase contrast cine MRI derived measures of intracranial pulsations in idiopathic normal pressure hydrocephalus", Journal of Clinical Neuroscience **33**, 169–172 (2016).

[36] Jeong, H. L., K. L. Ho, K. K. Jae, J. K. Hyun, K. P. Ji and G. C. Choong, "CSF flow quantification of the cerebral aqueduct in normal volunteers using phase contrast cine MR imaging", Korean Journal of Radiology **5**, 2, 81–86 (2004).

[37] Jung, B., M. Honal, P. Ullmann, J. Hennig and M. Markl, "Highly k-t-space-accelerated phase-contrast MRI", Magn Reson Med **60** (2008).

[38] Kahlon, B., M. Annertz, F. Ståhlberg and S. Rehncrona, "Is aqueductal stroke volume, measured with cine phase-contrast magnetic resonance imaging scans useful in predicting outcome of shunt surgery in suspected normal pressure hydrocephalus?", Neurosurgery **60**, 1, 124–129 (2007).

[39] Kapsalaki, E., P. Svolos, I. Tsougos, K. Theodorou, I. Fezoulidis and K. N. Fountas, *Hydrocephalus*, vol. 113 of *Acta Neurochirurgica Supplementum* (Springer Vienna, Vienna, 2012).

[40] Kurtcuoglu, V., M. Soellinger, P. Summers, K. Boomsma, D. Poulikakos, P. Boesiger and Y. Ventikos, "Computational investigation of subject-specific cerebrospinal fluid flow in the third ventricle and aqueduct of Sylvius", Journal of Biomechanics **40**, 6, 1235–1245 (2007).

[41] Kurwale, N. S. and D. Agrawal, "Phase-contrast magnetic resonance imaging of intracranial shunt tube: A valuable adjunct in the diagnosis of ventriculoperitoneal shunt malfunction", Clinical Neurosurgery **58**, 138–142 (2011).

[42] Lagerstrand, K. M., B. Vikhoff-Baaz, G. Starck and E. Forssell-Aronsson, "Quantitative phase-contrast flow MRI measurements in the presence of a second vessel closely positioned to the examined vessel", J Magn Reson Imaging **23** (2006).

[43] Lauterbur, P. C., "Image Formation by Induced Local Interactions: Examples Employing Nuclear Magnetic Resonance", Nature **242**, 5394, 190–191, URL `http://www.nature.com/doifinder/10.1038/242190a0` (1973).

[44] Lee, A. T., G. Bruce Pike and N. J. Pelc, "Three?Point Phase?Contrast Velocity Measurements with Increased Velocity?to?Noise Ratio", Magnetic Resonance in Medicine **33**, 1, 122–126 (1995).

[45] Liang, Z.-P. and P. C. Lauterbur, *Principles of Magnetic Resonance Imaging: A Signal Processing Perspective* (Wiley-IEEE Press, 1999).

[46] Loecher, M., E. Schrauben, K. M. Johnson and O. Wieben, "Phase unwrapping in 4D MR flow with a 4D single-step laplacian algorithm", Journal of Magnetic Resonance Imaging **43**, 4, 833–842 (2016).

[47] Luetmer, P. H., J. Huston, J. A. Friedman, G. R. Dixon, R. C. Petersen, C. R. Jack, R. L. McClelland, M. J. Ebersold, T. H. Milhorat and C. J. Hodge, "Measurement of cerebrospinal fluid flow at the cerebral aqueduct by use of phase-contrast magnetic resonance imaging: Technique validation and utility in diagnosing idiopathic normal pressure hydrocephalus", Neurosurgery **50**, 3, 534–543 (2002).

[48] Macovski, A., "Noise in MRI.", Magnetic resonance in medicine **36**, 3, 494–7, URL http://www.ncbi.nlm.nih.gov/pubmed/8875425 (1996).

[49] Maller, V. V. and S. Kanekar, "Imaging of Ventricular Shunts", Seminars in Ultrasound, CT and MRI **37**, 2, 159–173, URL http://www.sciencedirect.com.ezproxy1.lib.asu.edu/science/article/pii/S0887217116000044 (2016).

[50] Mansfield, P. and A. A. Maudsley, "Planar spin imaging by NMR", Journal of Physics C: Solid State Physics **9**, 15, L409–L412, URL http://stacks.iop.org/0022-3719/9/i=15/a=004?key=crossref.1889152035c618fa29b8e7d3d7d23453 (1976).

[51] Markl, M., A. Frydrychowicz, S. Kozerke, M. Hope and O. Wieben, "4D flow MRI.", Journal of magnetic resonance imaging : JMRI **36**, 5, 1015–36, URL http://www.ncbi.nlm.nih.gov/pubmed/23090914 (2012).

[52] Moftakhar, R., B. Aagaard-Kienitz, K. Johnson, P. A. Turski, A. S. Turk and D. B. Niemann, "Noninvasive measurement of intra-aneurysmal pressure and flow pattern using phase contrast with vastly undersampled isotropic projection imaging", AJNR Am J Neuroradiol **28** (2007).

[53] Moran, P. R., "A flow velocity zeugmatographic interlace for NMR imaging in humans", Magn Reson Imaging **1** (1982).

[54] Mosquera, C., P. Irarrazabal and D. G. Nishimura, "Noise behavior in gridding reconstruction.", International conference in Acoustics, Speech and Signal Processing , JUNE 1995, 2281–84, URL http://ieeexplore.ieee.org/xpls/abs{_}all.jsp?arnumber=479946 (1995).

[55] Nayler, G. L., D. N. Firmin and D. B. Longmore, "Blood flow imaging by cine magnetic resonance", J Comput Assist Tomogr **10** (1986).

[56] Negahdar, M., M. Kadbi, V. Tavakoli, J. Heidenreich and A. A. Amini, "Comparison of Cartesian, UTE radial, and spiral phase-contrast MRI in measurement of blood flow in extracranial carotid arteries: normal subjects", in "Medical Imaging", edited by J. B. Weaver and R. C. Molthen, p. 86720A (2013), URL http://proceedings.spiedigitallibrary.org/proceeding.aspx?doi=10.1117/12.2007438.

[57] Negahdar, M. J., M. Kadbi, M. Kotys, M. Alshaher, S. Fischer and A. A. Amini, "Rapid flow quantification in iliac arteries with spiral phase-contrast MRI", in "2011 Annual International Conference of the IEEE Engineering in Medicine and Biology Society", No. 1, pp. 2804–2808 (IEEE, 2011), URL http://ieeexplore.ieee.org/document/6090776/.

[58] Nishimura, D. G., A. Macovski and J. M. Pauly, "Magnetic resonance angiography", IEEE Trans Med Imaging **5** (1986).

[59] NR, Z. and P. JG, "Graphical programming interface", in "ISMRM Workshop on Data Sampling and Image Reconstruction", (2013; Session 8).

[60] NR, Z., J. KO and P. JG, "Efficient sample density estimation by combining gridding and an optimized kernel", Magnetic Resonance in Medicine **67**, 3, 701–710 (2012).

[61] Ooij, P., W. V. Potters, A. Guédon, J. J. Schneiders, H. A. Marquering and C. B. Majoie, "Wall shear stress estimated with phase contrast MRI in an in vitro and in vivo intracranial aneurysm", J Magn Reson Imaging **38** (2013).

[62] Ooij, P., J. J. M. Zwanenburg, F. Visser, C. B. Majoie, E. Bavel and J. Hendrikse, "Quantification and visualization of flow in the Circle of Willis: time-resolved three-dimensional phase contrast MRI at 7 T compared with 3 T", Magn Reson Med **69** (2013).

[63] Oyre, S., S. Ringgaard, S. Kozerke, W. P. Paaske, M. Erlandsen and P. Boesiger, "Accurate noninvasive quantitation of blood flow, cross-sectional lumen vessel area and wall shear stress by three-dimensional paraboloid modeling of magnetic resonance imaging velocity data", J Am Coll Cardiol **32** (1998).

[64] Ozturk, M., A. Sgrc and S. Unlu, "Evaluation of aqueductal cerebrospinal fluid flow dynamics with phase-contrast cine magnetic resonance imaging in normal pediatric cases", Clinical Imaging **40**, 6, 1286–1290 (2016).

[65] P, C., M. JV, G. E, A. D, R. M and C. DL, "Robust rician noise estimation for mr images", Medical Image Analysis **14**, 4, 483–493 (2010).

[66] Pelc, N. J., M. A. Bernstein, A. Shimakawa and G. H. Glover, "Encoding strategies for three-direction phase-contrast MR imaging of flow", J Magn Reson Imaging **1** (1991).

[67] Pelc, N. J., R. J. Herfkens, A. Shimakawa and D. R. Enzmann, "Phase contrast cine magnetic resonance imaging", Magn Reson Q **7** (1991).

[68] Pipe, J. G., E. Ahunbay and P. Menon, "Effects of interleaf order for spiral MRI of dynamic processes", Magnetic Resonance in Medicine **41**, 2, 417–422 (1999).

[69] Pipe, J. G. and R. K. Robison, "Simplified Signal Equations for Spoiled Gradient Echo MRI", vol. 29, p. 3114 (2010).

[70] Pipe, J. G. and N. R. Zwart, "Spiral trajectory design: A flexible numerical algorithm and base analytical equations", Magnetic Resonance in Medicine **71**, 1, 278–285 (2014).

[71] Pruessmann, K. P., M. Weiger, M. B. Scheidegger and P. Boesiger, "SENSE: sensitivity encoding for fast MRI", Magn Reson Med **42** (1999).

[72] Puntis, M., U. Reddy and N. Hirsch, "Cerebrospinal fluid and its physiology", Anaesthesia and Intensive Care Medicine pp. 611–612 (2016).

[73] Purcell, E. M., H. C. Torrey and R. V. Pound, "Resonance Absorption by Nuclear Magnetic Moments in a Solid", Physical Review **69**, 1-2, 37–38, URL `https://link.aps.org/doi/10.1103/PhysRev.69.37` (1946).

[74] Rabi, I. I., J. R. Zacharias, S. Millman and P. Kusch, "A New Method of Measuring Nuclear Magnetic Moment", Physical Review **53**, 4, 318–318, URL https://link.aps.org/doi/10.1103/PhysRev.53.318 (1938).

[75] Ridler, T. and S. Calvard, "Picture Thresholding Using an Iterative Selection Method", IEEE Transactions on Systems, Man, and Cybernetics **8**, 8, 630–632, URL http://ieeexplore.ieee.org/document/4310039/ (1978).

[76] Ringstad, G., K. E. Emblem, O. Geier, N. Alperin and P. K. Eide, "Aqueductal stroke volume: Comparisons with intracranial pressure scores in idiopathic normal pressure hydrocephalus", American Journal of Neuroradiology **36**, 9, 1623–1630 (2015).

[77] Sakka, L., G. Coll and J. Chazal, "Anatomy and physiology of cerebrospinal fluid", European Annals of Otorhinolaryngology, Head and Neck Diseases **128**, 6, 309–316 (2011).

[78] Scollato, A., R. Tenenbaum, G. Bahl, M. Celerini, B. Salani and N. Di Lorenzo, "Changes in aqueductal CSF stroke volume and progression of symptoms in patients with unshunted idiopathic normal pressure hydrocephalus", American Journal of Neuroradiology **29**, 1, 192–197 (2008).

[79] Song, S. M., S. Napel, G. H. Glover and N. J. Pelc, "Noise reduction in three-dimensional phase-contrast MR velocity measurements", J Magn Reson Imaging **3** (1993).

[80] Stankovic, Z., B. D. Allen, J. Garcia, K. B. Jarvis and M. Markl, "4D flow imaging with MRI", Cardiovasc Diagn Ther **4** (2014).

[81] Stivaros, S. M., D. Sinclair, P. A. Bromiley, J. Kim, J. Thorne and A. Jackson, "Endoscopic Third Ventriculostomy : Predicting outome with phase contrast MR imaging.", Radiology **252**, 3, 825–832 (2009).

[82] Stoquart-El Sankari, S., P. Lehmann, C. Gondry-Jouet, A. Fichten, O. Godefroy, M. E. Meyer and O. Baledent, "Phase-contrast MR imaging support for the diagnosis of aqueductal stenosis", American Journal of Neuroradiology **30**, 1, 209–214 (2009).

[83] Tang, C., D. D. Blatter and D. L. Parker, "Accuracy of phase contrast flow measurements in the presence of partial volume effects", Journal of Magnetic Resonance Imaging **3**, 2, 377–385 (1993).

[84] Ünal, Ö., A. Kartum, S. Avcu, Ö. Etlik, H. Arslan and A. Bora, "Cine phase-contrast MRI evaluation of normal aqueductal cerebrospinal fluid flow according to sex and age", Diagnostic and Interventional Radiology **15**, 4, 227–231 (2009).

[85] Untenberger, M., M. Hüllebrand, L. Tautz, A. A. Joseph, D. Voit, K. D. Merboldt and J. Frahm, "Spatiotemporal phase unwrapping for real-time phase-contrast flow MRI", Magnetic Resonance in Medicine **74**, 4, 964–970 (2015).

[86] Walker, P. G., G. B. Cranney, M. B. Scheidegger, G. Waseleski, G. M. Pohost and A. P. Yoganathan, "Semiautomated method for noise reduction and background phase error correction in MR phase velocity data", J Magn Reson Imaging **3** (1993).

[87] Wallace, A. N., J. McConathy, C. O. Menias, S. Bhalla and F. J. Wippold, "Imaging Evaluation of CSF Shunts", American Journal of Roentgenology **202**, 1, 38–53, URL `http://www.ajronline.org/doi/abs/10.2214/AJR.12.10270` (2014).

[88] Weinzierl, M. R., T. Krings, C. Ocklenburg and M. C. Korinth, "Value of cine phase contrast magnetic resonance imaging to predict obstructive hydrocephalus", J Neurol Surg A Cent Eur Neurosurg **73**, 1, 18–24 (2012).

[89] Wentland, A. L., O. Wieben, F. R. Korosec and V. M. Haughton, "Accuracy and reproducibility of phase-contrast MR imaging measurements for CSF flow", American Journal of Neuroradiology **31**, 7, 1331–1336 (2010).

[90] Winston, K. R., J. A. Lopez and J. Freeman, "CSF Shunt Failure with Stable Normal Ventricular Size", Pediatric Neurosurgery **42**, 3, 151–155, URL `http://www.karger.com/doi/10.1159/000091857` (2006).

[91] Yamada, S., K. Tsuchiya, W. G. Bradley, M. Law, M. L. Winkler, M. T. Borzage, M. Miyazaki, E. J. Kelly and J. G. McComb, "Current and emerging MR imaging techniques for the diagnosis and management of CSF flow disorders: A review of phase-contrast and time-spatial labeling inversion pulse", American Journal of Neuroradiology **36**, 4, 623–630 (2015).

[92] Youn, S. W., H. K. Kim, H. J. Lee and J. Lee, "Quantification of cerebral circulation and shunt volume in a tentorial dural arteriovenous fistula using two-dimensional phase-contrast magnetic resonance imaging", Acta Radiologica Short Reports **3**, 5, 1–5 (2014).

[93] Yousef, M. I., A. E. Abd El Mageed, A. E. N. Yassin and M. H. Shaaban, "Use of cerebrospinal fluid flow rates measured by phase-contrast MR to differentiate normal pressure hydrocephalus from involutional brain changes", The Egyptian Journal of Radiology and Nuclear Medicine **47**, 3, 999–1008 (2016).

[94] Yue, E. L., G. D. Meckler, R. J. Fleischman, N. R. Selden, D. M. E. Bardo, A. K. Chu O'Connor, E. T. Vu, R. Fu and D. M. Spiro, "Test characteristics of quick brain MRI for shunt evaluation in children: an alternative modality to avoid radiation", Journal of Neurosurgery: Pediatrics **15**, 4, 420–426, URL `http://www.ncbi.nlm.nih.gov/pubmed/25634816{%}5Cnhttp://thejns.org/doi/abs/10.3171/2014.9.PEDS14207http://thejns.org/doi/10.3171/2014.9.PEDS14207` (2015).

[95] Zwart, N. R. and J. G. Pipe, "Multidirectional high-moment encoding in phase contrast MRI.", Magnetic resonance in medicine **69**, 6, 1553–64, URL `http://www.ncbi.nlm.nih.gov/pubmed/22760964` (2013).

[96] Zwart, N. R. and J. G. Pipe, "Graphical programming interface: A development environment for MRI methods", Magnetic Resonance in Medicine **74**, 5, 1449–1460 (2015).

APPENDIX A

FLOW PHANTOM

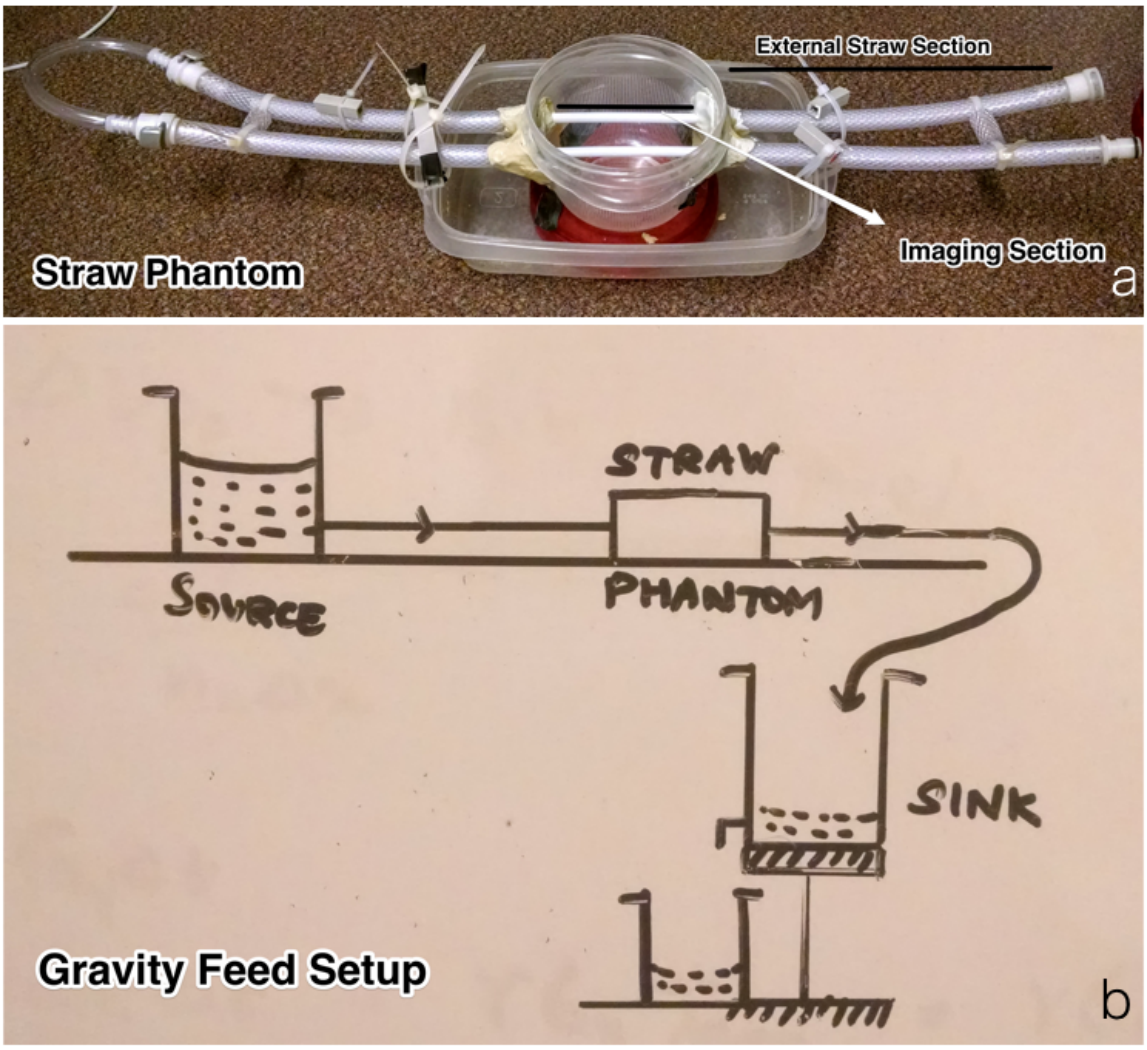

Figure A.1: (a) Design of the flow phantom used in data acquisition for chapters 3 and 4. (b) Schematic of the phantom setup in the scanner

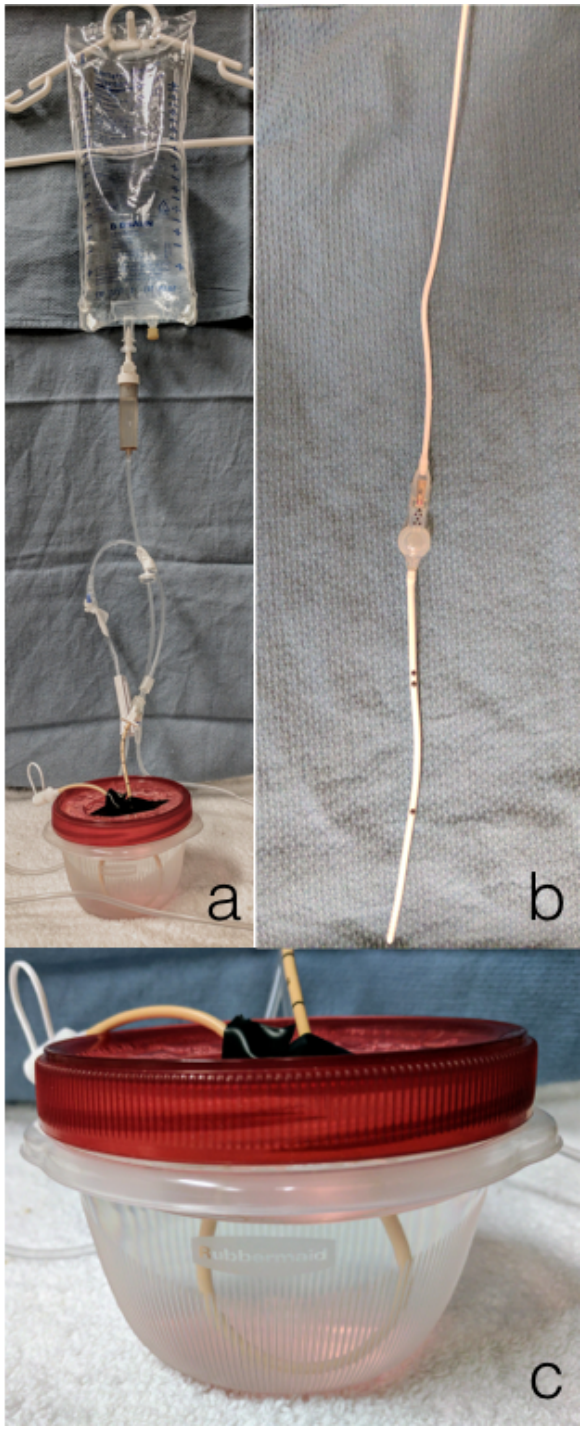

Figure A.2: (a) Design of the flow phantom used in data acquisition for chapter 5 experiments. The IV bag was used as the source and the outflow shunt catheter was connected to a 1000 ml beaker acting as the drain. (b) An typical ventricular shunt catheter is shown with the proximal catheter section and the distal catheter section connected using a programmable valve. (c) The imaging section of the shunt catheter phantom consists of a 'U' shaped proximal catheter immersed in a water bath.